

Dr. Vreeland,
I enjoyed studying
under you and hope you
will have continuing success.

SHOCK-WAVE CONSOLIDATION
OF
METALLIC POWDERS

Prakash

Thesis by
Prakash Kasiraj

In Partial Fulfillment of the Requirements
for the Degree of
Doctor of Philosophy

California Institute of Technology
Pasadena, California

1985

(Submitted July 31, 1984)

TO MY MOTHER
AND
IN MEMORY OF MY FATHER

ACKNOWLEDGEMENTS

I would like to thank Dr. Thad Vreeland, Jr. for his excellent advise and guidance. His friendly demeanor and good temperament made graduate research at Caltech an enjoyable and pleasant phase in my life. I would also like to thank Dr. Ricardo B. Schwarz for his many useful ideas, as well as for his contagious enthusiasm and energy.

I would like to thank Dr. Thomas J. Ahrens for the use of the Caltech Seismology Laboratory. This thesis would not have been possible without those facilities. I would also like to thank Dr. Bill Johnson and Dr. D. S. Wood for allowing me to discuss ideas with them.

The completion of my research and thesis required help from many individuals. I would like to thank, in particular; Dan Kostka, Mary Jane Bartholomew, Papo Gelle, Mike Long, Chuck Manning, Darrel Schlom, John Krehbiel, Anne Sauter, Lynne K. Adler, and Costa Potamianos. I would like to thank Carolyn Meredith for her help in preparation of manuscripts of my thesis and other papers.

The experience at Caltech would not have been as fulfilling and memorable if it were not for the many friends I made during my graduate life. I would like to mention a few of them; Larry Sverdrup, Roy Williams, Steve Douglass, Ted and Jeri Russel, Byron Siu, Brian Newport, Tom Banwell, and the people of the 3rd floor of the Keck building. In addition, I would like to thank the team members of the Garvey's Softball Team, Caltech Men's Volleyball Team, and the Smashers Basketball Team for giving me many hours of relaxation and fun.

Finally, I would like thank my family, especially my mother Jothi, for providing the proper intellectual and emotional nourishment which has allowed me to come this far.

ABSTRACT

Conventional powder metallurgical techniques have the drawback in that metastable properties of the powder can be lost during the sintering stage. The use of shock waves to bond particles of powder together can, in principle, circumvent this drawback and produce bulk solids which retain metastable properties of the initial powder. However, the effects of the relevant shock and powder parameters on the final properties of the compacts must be understood before this technique can be used optimally.

In the present investigation the influence of shock pressure, shock duration, and surface oxides on the mechanical and metallurgical properties of compacted steel, molybdenum, and nickel-molybdenum alloy powders were studied. In addition, to improve our fundamental understanding of shock waves in metallic powder media, the shock temperature at the junction between two layers of copper and constantan powders was measured via the thermoelectric effect for varying shock pressure and energy.

The measured homogeneous temperatures in the copper-constantan powders varied from 150 C to 940 C as the shock energy was increased from 50 to 360 kJ/kg (shock pressure from 1.3 to 9.4 GPa). These results indicate that almost all of the energy in the shock front is converted into thermal energy. Furthermore, the rise time of the shock front is less than 23 ns which corresponds to a shock front width of less than 37 μm , a dimension comparable to the powder particle diameter.

Rapidly solidified AISI 9310 steel powders were consolidated and the dependence of the microhardness and the ultimate tensile strength of the compacts on the shock energy from 94 to 770 kJ/kg (3.6 to 19.0 GPa)

were measured for an initial powder distension of 1.64 and a shock duration of 2-3 μ s. Photomicrographs and SEM fractographs were used to study the interparticle bonding in the compacts. Results show that, for shock energies below 200 kJ/kg (4.9 GPa), the compacts have negligible strength. However, above this threshold the strength of the compact rises rapidly until a maximum value of 1.3 GPa is reached at a shock energy of 500 kJ/kg (12.4 GPa). This strength which is larger than that of wrought AISI 9310 remains constant before decreasing at the higher shock energies. In marked contrast, with increasing shock energy, the diamond pyramid hardness increases very gradually from a value of 340 for the initial powder to 500 at a shock energy of 500 kJ/kg. Microhardness also begins to decrease at higher shock energies. The maximum strength obtained correlates well with the strength expected from microhardness measurements.

The AISI 9310 powders were also used to study the effect of shock duration on the compact's strength. Results indicate that, for consolidations with a shock energy of 400 kJ/kg (10 GPa), shock durations greater than 0.4 μ s are needed to produce strong compacts. This lower limit on shock duration can be attributed to the condition that the duration of the compressive shock wave must exceed the solidification and strengthening time of the melt produced by the shock wave.

Molybdenum powders with a distension of 1.67 were used to study the effect of surface oxides. Results indicate that, by reducing the surface oxides, the tensile strength of the compact can be increased from nearly zero to 0.76 GPa for a shock energy of 580 kJ/kg (17.8 GPa). The final strength is comparable to that of bar stock of molybdenum.

Powders of glass forming Mark-1064 alloy ($\text{Ni}_{55.8}\text{Mo}_{25.7}\text{Cr}_{9.7}\text{B}_{8.8}$) with a distension of 2.0 were used to study the amount of melt produced during the shock consolidation process. Such measurements were possible because the melt was quenched rapidly enough to form the amorphous phase which could be delineated from the microcrystalline phase during metallographic examination. The results indicate that shock energies above 190 kJ/kg (3.4 GPa) are required before the occurrence of measurable melting. The amount of melt is much less than the upper bound limit and the melt distribution is nonuniform.

Finally, the conceptual understanding of the shock consolidation process is discussed and the criteria for producing well-bonded compacts are enumerated. These criteria can be conveniently expressed in terms of a shock consolidation map which plots a dimensionless shock duration versus a dimensionless shock energy. The existing models for the shock consolidation process are evaluated in light of the recently acquired results.

TABLE OF CONTENTS

	Page
Acknowledgements	iii
Abstract	iv
List of Tables	ix
List of Illustrations	x
1. INTRODUCTION	1
REFERENCES	6
2. PHYSICS OF SHOCK CONSOLIDATION	8
2.1 Introduction	8
2.2 Conservation Laws	10
2.3 Thermal Shock Energy	13
2.4 Powder Hugoniot	15
2.5 Homogeneous Shock Temperature	20
2.6 Impedance Matching Calculations	23
REFERENCES	39
3. SHOCK TEMPERATURE MEASUREMENTS	40
3.1 Introduction	40
3.2 Temperature Measurement Techniques	41
3.3 Bimetallic Powder Thermocouple	43
3.4 Experimental Method	45
3.5 Calculated Homogeneous Temperature	49
3.6 Results and Discussion	51
3.7 Summary	56
REFERENCES	74
4. SHOCK CONSOLIDATION AND RECOVERY EXPERIMENTS	76
4.1 Introduction	76
4.2 Experimental Method	77
4.3 Shock Energy	79
4.4 Shock Duration	85
4.5 Surface Oxides	87
4.6 Interparticle Melting	88
4.7 Summary	93
REFERENCES	119

TABLE OF CONTENTS (cont.)

	Page
5. SHOCK CONSOLIDATION MAPS	121
5.1 Introduction	121
5.2 Characteristic Times in the Shock Consolidation Process .	121
5.3 Criteria for Successful Shock Consolidations	124
5.4 Shock Consolidation Map for Spherical Steel Powders . . .	126
5.5 Energy Deposition Mechanisms	128
5.6 Melt Threshold	133
5.7 Concluding Remarks	135
REFERENCES	141
APPENDIX A FABRICATION OF POWDER THERMOCOUPLE	142
APPENDIX B ETCHANTS USED IN METALLOGRAPHY	145
APPENDIX C TENSILE TEST MEASUREMENTS	146
APPENDIX D SURFACE OXIDE REDUCTION	152
REFERENCES	154

LIST OF TABLES

Table		Page
3.1	Results of the powder copper-constantan thermocouple experiments.	58
3.2	Comparison of predicted shock transit times with the measured transit times.	59
4.1	Properties of powders used in the shock consolidation and recovery experiments [2].	95
4.2	Properties of the wrought materials whose powder forms were used in the shock consolidation experiments [3,8].	96
4.3	Shock wave consolidation data for 44-74 micron diameter AISI 9310 powders of distension $m = 1.64$.	97
4.4	Results of the shock consolidation of microcrystalline Markomet 1064 powder with distension of $m = 2.0$.	98
4.5	Thermal data for aluminum [19] and Marko-1064 [20]. The specific heat is the average value from 20 to 600 C.	99
5.1	Characteristic times in the shock consolidation process. These are typical values in the consolidation of 58 μm AISI 9310 steel. The solidification time was estimated from the dependence of UTS on shock duration. The other four times were calculated as explained in the text.	136
5.2	Thermal and thermodynamic properties of iron [17].	137
5.3	The slope and intercept in the linear melt fraction versus shock energy relation, $M_f = M_0(L-L_0)$. The $\text{Al}_{94}\text{Si}_6$ results are from Ref. [16].	138

LIST OF ILLUSTRATIONS

Figure		Page
1.1	The 20 mm bore propellant gun used in most of the shock consolidation experiments. The breach is on the left while the muzzle and the target recovery chamber are on the far right.	5
2.1	Schematic drawing of a shock wave traveling to the right. E, u, P, and ρ stand for specific internal energy, particle velocity, pressure, and mass density, respectively.	27
2.2	Schematic diagram of shock pressure versus specific volume for a shocked solid.	28
2.3	Schematic diagram of pressure versus volume for a solid which is released from the shocked state.	29
2.4	Schematic diagram of pressure versus volume for a shocked powder medium.	30
2.5	Shock impedance data for solid and porous copper [4]. The solid lines are from the porous Hugoniot model described in text. The values used for γ , η_s , and V_0 are 1.98, 0.0073 GPa^{-1} , and 1.12×10^{-4} , respectively [10].	31
2.6	Schematic diagram showing the shock state (P_1, u_1) produced by the impact of a flyer on a target. V_f is the flyer velocity.	32
2.7	Schematic drawing of a steel flyer plate impacting a steel powder layer which is backed by a steel base.	33

LIST OF ILLUSTRATIONS (cont.)

Figure		Page
2.8	The impedance curves used in calculating the shocked states produced in the experiment depicted in Fig. 2.7 with a flyer velocity of 1.2 km/s.	34
2.9	The position vs time diagram of the shock fronts and release waves produced in the experiment depicted in Fig. 2.7. The encircled numbers correspond to the shock states shown in Fig. 2.8.	35
2.10	Pressure-time history in the shocked powder at the surface of impact (solid line) and at the surface of contact with base (dashed line). This diagram follows from analysis shown in Fig. 2.9.	36
2.11	Schematic depiction of cone-like volume in which the one-dimensional analysis of shock wave propagation is valid. The duration of the one-dimensional conditions inside of the cone depends on the location and speed of the edge disturbances.	37
2.12	Schematic diagram of how the shock state (P_1, u_1) produced by the impact of a flyer (whose shock impedance is known) on a powder medium (whose shock impedance is unknown) can be determined by measuring the shock velocity C_s and flyer velocity V_f .	38
3.1	Schematic representation of the idea for measuring shock temperatures with the shocked media generating the thermoelectric signals at the interface between the two metals.	60

LIST OF ILLUSTRATIONS (cont.)

Figure		Page
3.2	SEM photomicrograph of -100 mesh copper powder used in the experiments.	61
3.3	X-ray diffraction intensity lines of a mixture of 55% copper and 45% nickel powders at different stages of mechanical alloying: (a) after mechanical alloying for 10 min.; (b) after 3.5 hrs.; (c) after 5 hrs. and thermal anneal in purified hydrogen atmosphere at 750 C for 16 hrs. Powder (c) was used in the thermocouple experiments.	62
3.4	SEM photomicrograph of constantan powder used in experiments. Note the flat shape obtained from the ball milling fabrication procedure.	63
3.5	Thermoelectric voltage of the copper-constantan powder junction as a function of temperature with the constantan as the reference ground [20].	64
3.6	The change in thermoelectric voltage (per 100 C) as a function of pressure [18].	65
3.7	Schematic cross-sectional view of the powder thermocouple assembly with: A) 5.08 mm thick X 15.88 mm diameter flyer, B) 3.18 mm thick copper buffer plate, C) copper powder, 0.78 mm thick at center, D) constantan powder, 4 mm thick at center, E) 0.5 mm thick alumina powder, F) 6mm long quartz tube with 11.7 mm I.D. and 14.0 mm O.D., and G) epoxy coating. The diameter of the powder pill was 2 cm. The diameter of the copper-constantan interface was 4.7 mm.	66

LIST OF ILLUSTRATIONS (cont.)

Figure		Page
3.8	Photograph of experimental assembly prior to loading onto the 20 mm gun barrel. The vacuum chamber was 5 cm wide and 3.8 cm long. The 7.6 cm X 7.6 cm copper buffer plate was 3.18 mm thick.	67
3.9	Shock impedance matching solution for the impact of 1.03 km/s aluminum flyer on a copper buffer plate and the subsequent shocking of the copper powder by the buffer plate. Hugoniot data for the copper powder from Ref. [23] was fit by the analytical equation for porous media from Ref. [25]. Hugoniot for solid copper and aluminum are from Ref. [25].	68
3.10	The specific heat at constant pressure of nickel, constantan, and copper [26].	69
3.11	Thermal conductivity data for copper, nickel, and constantan [26].	70
3.12	Oscilloscope trace of the thermocouple signal from shot 798. Vertical scale: 20 mv/div. Sweep rate: 0.5 μ s/div.	71
3.13	Shock sweep times across a 4.7 mm diameter area when the flyer face has a tilt for different flyer velocities on the 20 mm gun.	72
3.14	The measurements of the homogeneous junction temperature plotted as a function of shock energy. The solid line represents the calculated junction temperature and the dashed line represents the calculated copper temperature.	73

LIST OF ILLUSTRATIONS (cont.)

Figure		Page
	The calculated temperature of the constantan is not shown on the figure, but lies about 10% below the copper curve.	
4.1	Schematic cross-section of the target recovery assembly. The dimensions of the target assembly are: a) 8.3 cm O.D. X 2.0 cm I.D. X 2.5 cm thick target ring, b) 8.9 cm diameter X 2.5 cm thick base, and c) 8.9 cm diameter X 3.8 cm thick axial spall plate.	100
4.2	Shock Hugoniot for pure iron [21], 304 stainless steel [22], and porous iron (points from Ref. [4], curves from Ref. [5]) used in calculations. The symbols + and x are the measured points for AISI 9310 with distension $m = 1.67$ and 1.43, respectively.	101
4.3	SEM micrograph of AISI 9310 rapidly solidified powder particles (-200 +300 mesh).	102
4.4	Photomicrographs of compacted AISI 9310 samples with shock energies of: a) 240 kJ/kg, b) 500 kJ/kg, and c) 730 kJ/kg. Etchant = 5% nital, room temperature.	103
4.5	Low magnification SEM fractographs of compacted AISI 9310 samples with shock energies of: a) 240 kJ/kg, b) 500 kJ/kg, and c) 730 kJ/kg.	104
4.6	Normal SEM views of fractured surfaces from compacted AISI 9310 samples with shock energies of: a) 240 kJ/kg, b) 500 kJ/kg, and c) 730 kJ/kg.	105
4.7	Dependence of diamond pyramid hardness and ultimate tensile	106

LIST OF ILLUSTRATIONS (cont.)

Figure		Page
	strength on the shock energy with a shock duration of 2-3 μ s. The open circles are the DPH values and the closed squares are the UTS values.	
4.8	Time-position histogram for the experiment in which the effect of the shock duration on AISI 9310 compact strength was measured. A 304 stainless steel flyer with a velocity of 1.16 km/s is shown impacting an AISI 9310 powder sample with $m = 1.69$. The diagram shows the leading edge of the release fan.	107
4.9	UTS versus shock duration for AISI 9310 alloy consolidated at a shock pressure of 9.5 GPa and shock energy of 404 kJ/kg.	108
4.10	SEM micrograph of AMAX Mo powder.	109
4.11	Photomicrograph of the compacted surface treated Mo consolidated with the shock energy of 580 kJ/kg. Etchant = Murikami's solution, room temperature.	110
4.12	SEM micrograph of Markomet 1064 powder.	111
4.13	Shock Hugoniot of Markomet 1064 powder for a distension $m = 2.0$ [13].	112
4.14	Photomicrograph of Markomet 1064 powder in the: A) amorphous phase, and B) microcrystalline phase (annealed at 900 C). Etchant = Marble's reagent, room temperature. 10μ m	113
4.15	Photomicrographs of compacted microcrystalline Markomet 1064 with shock energy of 190 kJ/kg: A) plane of shock	114

LIST OF ILLUSTRATIONS (cont.)

Figure		Page
	front, and B) perpendicular plane to shock front (shock travel from top to bottom of picture). Etchant = Marble's reagent, room temperature. $\overline{50 \mu\text{m}}$	
4.16	Photomicrographs of compacted microcrystalline Markomet 1064 with shock energy of 279 kJ/kg: A) plane of shock front, and B) perpendicular plane to shock front (shock travel from top to bottom of picture). Etchant = Marble's reagent, room temperature. $\overline{50 \mu\text{m}}$	115
4.17	Photomicrographs of compacted microcrystalline Markomet 1064 with shock energy of 350 kJ/kg: A) plane of shock front, and B) perpendicular plane to shock front (shock travel from top to bottom of picture). Etchant = Marble's reagent, room temperature. $\overline{50 \mu\text{m}}$	116
4.18	Higher magnification photomicrograph (in the shock plane) of compacted microcrystalline Markomet 1064 with shock energy of 350 kJ/kg. Etchant = Marble's reagent, room temperature.	117
4.19	Melt fraction data for Al+6%Si powder [16] and Mark-1064 powder in terms of the normalized shock energy, L, which is defined as the shock energy per mass divided by the energy per mass required to melt the material.	118

LIST OF ILLUSTRATIONS (cont.)

Figure		Page
5.1	The shock consolidation map for AISI 9310 steel powders. The clear circles denote compacts with UTS < 0.3 GPa. The half-filled circles denote compacts with $0.3 < \text{UTS} < 0.8$ GPa. The filled circles denote compacts with UTS > 0.8 GPa.	139
5.2	Photomicrograph in the plane of the shock wave of consolidated AISI 9310 powder (44-74 μm in diameter) with a shock energy of 240 kJ/kg. The letter "A" denotes areas where the surface oxides have been dispersed by the converging collision of three or more deforming particles. The letter "B" denotes the area where oxides may be dispersed due to high shock pressure at a point-like contact. Etchant = MoO_3 etch.	140
C1	The fixture on the right is used for measuring the tensile strength of dog-bone shaped tensile specimens. The fixture on the left is for ribbon shaped tensile specimens (not used in the present investigation). The letters "A" denote the Mo pull wires. The letters "B" denote the guide wires that are attached to the LVDT coil. The letter "C" denotes the central tube that is attached to the LVDT core.	149
C2	The tensile test fixture with a sample tensile specimen is shown in the picture. The springs are used to hold the pins firmly to the holes in the tensile specimen. The upper pin is attached to the guide wires labeled "B". The lower pin is attached to the central tube labeled "C".	150

LIST OF ILLUSTRATIONS (cont.)

Figure		Page
C3	The stress-strain curve of a tensile specimen pulled with the tensile fixture shown in Fig. C2.	151

CHAPTER 1

INTRODUCTION

Shock-wave consolidation of powders is a promising technique for obtaining fully dense and strong materials which retain metastable properties of the initial powder. Conventional compaction methods involve the quasistatic pressing and sintering of the powder. The bonding of powder particles and the reduction of porosity occur mainly by atomic diffusion, thus requiring high temperatures (75% of the melting temperature or higher) for long durations (6 hours or more) [1]. During the sintering stage, metastable properties of the powder cannot be retained and the long exposure to high temperatures precludes the use of chemically reactive powder mixtures. In addition the compacts usually have significant residual porosity. These restrictions in powder compaction may be overcome with the use of shock waves to bond particles together. Thus shock waves may play an important role in the synthesis of novel and technologically useful bulk materials.

Qualitatively, consolidation by shock waves is achieved via preferential deposition of energy at particle surfaces which occurs during the shock rise-time. The preferential surface deposition has been attributed mainly to friction between particles [2-4]. The selectiveness of the heating allows for the possibility of obtaining well-bonded compacts without subjecting the bulk to high homogeneous temperature for long durations, as required in conventional powder metallurgical processes. Furthermore, the large pressures (10 GPa or

higher) obtainable through shock waves can produce compacts with nearly zero porosity. Although consolidation without local melting of particles may take place [5], it appears that energy deposition which causes interparticle melting is required before very strong compacts are produced [6]. However, these interparticle melt layers can be quenched as rapidly as 10^5 - 10^{10} C/s depending on their thickness [7]. Before the shock consolidation process can be optimally applied to the fabrication of materials, knowledge of the conditions required to produce strong compacts (while retaining the metastable properties of the powder) is needed.

Two general methods have been used to affect the shock consolidation of powders. In the explosive compact method, consolidation is achieved by detonating explosives attached to the powder in various geometries [8,9]. The other method involves the production of shock waves by high-velocity impact of flyers [3]. The explosives method has the advantage of lower capital investment and the feasibility of producing large compacts (in the scale of meters). This method will probably be used in any large-scale commercial application of the shock consolidation process. However, the flyer-impact method is much more attractive in terms of studying the shock consolidation process since the shock history of the powder can be more easily controlled and defined. Thus in our studies the shock waves were generated by high-velocity flyer impacts. The 20 mm bore gun from the California Institute of Technology Seismology Laboratory was used for most of our experiments and is shown in Fig. 1.1.

Although shock compaction has been studied since the 1950's [10], there is a scarcity of quantitative investigations on the relevant

parameters which govern the consolidation process. Previously, powders of lead, iron, aluminum, steel, and metallic glasses have been compacted by flyer plate impact [2,6,11,12,13]. In these studies the powder was subjected to relatively low shock pressures (less than 2 GPa) and the steel compacts produced had relatively low strength in relation to their hardness [2]. The shock consolidation process at higher pressures was not explored. Systematic studies on properties such as, strength and microhardness of the compacts and the melt production during shock consolidation, are lacking.

Several models of the shock consolidation process have been advanced. A shock rise-time criterion was introduced which requires that the shock-energy deposition rate at the surface of the particles be higher than the heat conduction rate into the interior of the particles, so as to reach the melting temperature at the particle surfaces [2,14]. The requirement that the compressive shock duration must be long enough to insure that the melted regions have solidified and strengthened before release occurs [4] was quantitatively treated by using an upper bound calculation of melt material for a given shock energy and by assuming a uniform distribution of melt [15]. However, these models are approximate and their usefulness has to be evaluated.

Some fundamental laws of shock wave propagation derived from conservation laws and basic concepts which are necessary for the discussion of shock waves in powder media are introduced in Chapter 2. To verify the assumptions usually made for the propagation of shock waves through a porous medium (introduced in Chapter 2), shock temperature measurements were performed on copper-constantan powder media by using the medium as a thermocouple. These results are

presented in Chapter 3. Measurements and observations made on compacts from steel, molybdenum, and nickel-molybdenum alloy powders that were recovered after shock consolidation are presented in Chapter 4. The AISI 9310 steel compacts were tested for ultimate tensile strength and microhardness, as the shock pressure and shock duration were varied. The tensile tests and microhardness measurements provide quantitative evaluation of the interparticle bonding. Photomicrographs and SEM fractographs were also used to study the nature of particle bonding and deformation. Molybdenum powders were used to study the effect of surface contaminants such as oxides on the strength of the compact. Powders of the glass forming Markomet 1064 ($\text{Ni}_{55.8}\text{Mo}_{25.7}\text{Cr}_{9.7}\text{B}_{8.8}$) were used to measure the amount of melt produced by shock waves. These measurements could be made because the amorphous phase formed from the rapid quenching of the melt could be distinguished from the microcrystalline phase. The melt data provide useful insights into the shock consolidation process. The conceptual understanding and the criteria for producing well-bonded compacts are discussed in Chapter 5. The models for the shock consolidation process are evaluated in light of the new understanding and knowledge gained from the present investigation. Finally it should be noted that parts of Chapters 4 and 5 have been published elsewhere [15,16,17,18,19].

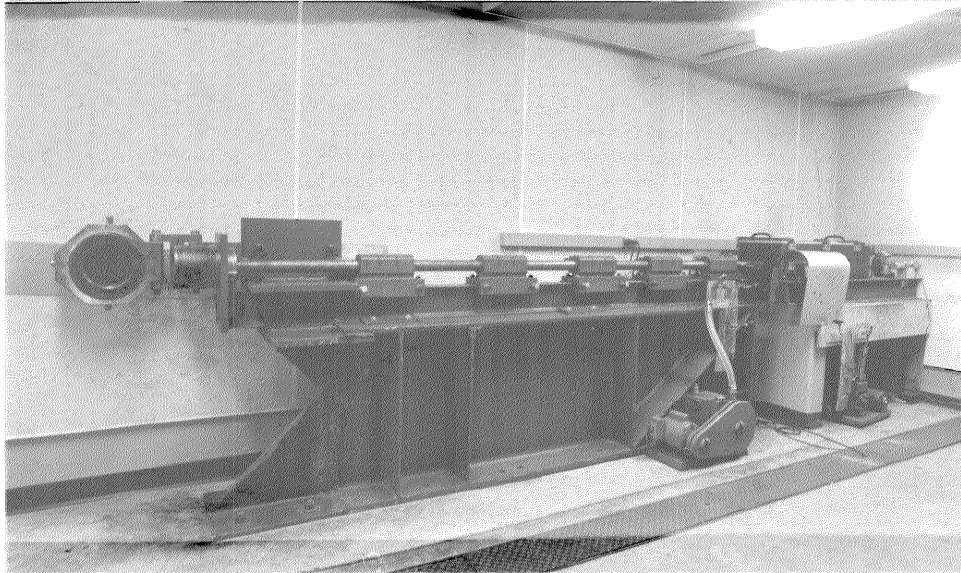


Fig. 1.1 The 20 mm bore propellant gun used in most of the shock consolidation experiments. The breach is on the left while the muzzle and the target recovery chamber are on the far right.

CHAPTER 1 REFERENCES

1. Hirshhorn, J. S., Introduction to Powder Metallurgy, American Powder Metallurgy Institute, Princeton, 1969.
2. Raybould, D., Int. J. Powder Metallurgy and Powder Tech., 16, 9 (1980).
3. Raybould, D., D. G. Morris, and G. A. Cooper, J. Material Sci., 14, 2523 (1979).
4. Staver, A. M., in Shock Waves and High-Strain-Rate Phenomena in Metals, Ch. 49, M. A. Meyers and L. E. Murr, ed., Plenum Press, New York, 1981.
5. Hoenig, C. L. and C. Yost, Bull. Am. Ceramic Soc., 60, 1175 (1981).
6. Raybould, D., J. Mat. Sci., 16, 589 (1981).
7. Morris, D. G., Metal Sci., 16, 457 (1982).
8. Meyers, M. A., B. B. Gupta, and L. E. Murr, J. of Metals, 33, 21 (1981).
9. Pruemmen, R. A. and A. Ziegler, Powder Metallurgy Int., 9, 11 (1977).
10. LaRocca, E. W. and J. Pearson, Rev. Sci. Instrum., 29, 848 (1958).
11. Raybould, D., in Proc. 15th Int. Mach. Tool Design and Res. Conf., S. A. Tobias and F. Koengsberger, ed., MacMillan Publishing Co., London, 1975.
12. Morris, D. G., Metal Sci., 14, 216 (1980).
13. Morris, D. G., Metal Sci., 15, 116 (1981).
14. Gourdin, W. H., J. Appl. Phys., 55, 172 (1984).
15. Schwarz, R. B., P. Kasiraj, T. Vreeland, Jr., and T. J. Ahrens, Acta Metall., 1984, in press.
16. Kasiraj, P., T. Vreeland, Jr., R. B. Schwarz, and T. J. Ahrens, Acta Metall., 1984, in press.
17. Schwarz, R. B., P. Kasiraj, T. Vreeland, Jr., and T. J. Ahrens, in Shock Waves in Condensed Matter - 1983, Ch. X:2, J. R. Asay, R. A. Graham, G. K. Straub, ed., North-Holland Physics Publishing, New York, 1984.

18. Kasiraj, P., T. Vreeland, Jr., R. B. Schwarz, and T. J. Ahrens, in Shock Waves in Condensed Matter - 1983, Ch. X:3, J. R. Asay, R. A. Graham, G. K. Straub, ed., North-Holland Physics Publishing, New York, 1984.
19. Vreeland, T., Jr., P. Kasiraj, T. J. Ahrens, and R. B. Schwarz, in Proc. Material Research Soc. Conf., Nov. 14-17, 1983, Boston, Mass., in press.

CHAPTER 2

PHYSICS OF SHOCK CONSOLIDATION

2.1 Introduction

The theory as well as experimental aspects of the formation and propagation of shock waves is covered by several excellent texts [1,2]. In the the present chapter, only the concepts which are relevant and useful for the passage of shock waves in powder media will be reviewed and discussed.

In most materials the isentropic compressibility decreases with increasing pressure so that small acoustical disturbances propagate faster with increasing pressure. Thus an initial pressure wave of an arbitrary spatial profile and sufficient amplitude will steepen its pressure gradient as the higher pressure components overrun the beginning of the wave. This process continues until the wave steepens and stabilizes into a single shock transition, which is an almost discontinuous jump in the pressure profile. This jump is mediated by a transition zone which will be referred to as the shock front.

In addition to pressure, other quantities, such as entropy and temperature, also discontinuously increase across the shock front due to the dissipative nature of shock compression of most materials. The spatial width and structure of the shock front depend on the details of the dissipative mechanisms. The width of the shock front in gases cannot be smaller than the collisional mean free path of the molecules, while in solids the width can be as small as a few atomic spacings.

However, in the case of powder media which are composed of individual solid particles and voids in the size range of tens of microns, one can consider two types of shocks, depending on the scale of description. In the atomic scale, there are the normal shocks in solids which reverberate throughout the powder particle and are responsible for the deformation of the particle. These shocks are produced by collisions with the surrounding particles. The strength and shape of these shocks can be quite complicated and are beyond the scope of the present study. However, there is also an effective deformation front which is determined by the time required to eliminate voids by particle deformation. The width of this deformation front depends on the details of the particle deformation and cannot be smaller than the particle size. It is usually assumed that these deformation fronts are indeed true shock fronts, and that the shock reverberations in the particles are just details within the shock front. This important assumption will be tested and validated for metallic powders in Chapter 3. Henceforth, the term shock front will be used to refer to the deformation front in powder media.

In section 2.2 the conservation laws which apply only to true shock wave propagation will be introduced. Although these laws are independent of the details of the dissipative mechanisms in the shock front, they will be very useful in the study of shock wave consolidation. The discussion on the mechanisms which are responsible for the preferential deposition of energy on the particle surfaces during the shock consolidation process will be deferred until Chapter 5. In section 2.3, the concept of separating the internal energy gain into thermal and nonthermal components will be introduced. The analytical

model used in our present treatment of the shock Hugoniot in powder media will be introduced in section 2.4. In section 2.5 the thermal component of shock energy is used to calculate the homogenous shock temperatures. The techniques used to calculate the shock pressures attained in our experiments will be explained in section 2.6.

2.2 Conservation Laws

Consider the motion of a steady-state plane shock wave. For steady-state conditions, the shock front size and shape do not change as the shock wave propagates through a medium. The plane wave condition reduces the motion into a one-dimensional problem. A shock wave traveling from left to right is schematically depicted in Fig. 2.1. The unshocked state is denoted by the subscript 0, while the shocked state is denoted by the subscript 1. The shock parameters E , u , P , and ρ are the specific internal energy (kJ/kg), particle velocity (km/s), pressure (GPa), and mass density (kg/m^3) of the medium, respectively. The shock velocity is denoted by C_s . The above mentioned variables can be considered to be in thermodynamic equilibrium if far enough removed from the shock front. Thus in the following discussion, the values of E , u , P , and ρ will be assumed to be constant and uniform on both sides of the shock front.

By invoking conservation of mass, momentum, and energy, one can derive three independent equations which relate the shocked state parameters to the initial unshocked state parameters and the shock velocity. To simplify the equations to be presented, we will assume that the unshocked medium is at rest, i.e., $u_0 = 0$. However, this does not reduce the generality of the equations since by a Galilean transformation one can always choose a reference frame in which the

medium is initially at rest.

When applying the conservation laws, the appropriate quantities to consider are fluxes, i.e., quantity per unit area per unit time. Hence, conservation of mass flux across a shock front requires

$$\rho_0 C_s = \rho_1 (C_s - u_1). \quad (2.2.1)$$

The change in momentum flux across the shock front must be equal to the difference in pressure, and is given by

$$P_1 - P_0 = u_1 \rho_1 (C_s - u_1).$$

Finally the difference in the flux of the sums of the internal and kinetic energies must be equal to the rate of work done by the moving shock front. This relation is given by

$$u_1 P_1 = \rho_1 E_1 (C_s - u_1) + \frac{1}{2} \rho_1 u_1^2 (C_s - u_1) - \rho_0 E_0 C_s.$$

The above three equations can be combined and reformulated to give:

$$P_1 - P_0 = \rho_0 C_s u_1 \quad (2.2.2)$$

and

$$E_1 - E_0 = \frac{1}{2} (P_1 + P_0) (V_0 - V_1) \quad (2.2.3)$$

where $V = 1/\rho$ is the specific volume. Equation 2.2.1, 2.2.2, and

2.2.3 are the usual forms of the so called Rankine-Hugoniot equations which relate the conditions ahead of the the shock front to the conditions behind the shock front. With further manipulations, one can get other useful relations such as

$$u_1 = [(P_1 - P_0)(v_0 - v_1)]^{1/2} \quad (2.2.4)$$

and

$$c_s = v_0 [(P_1 - P_0)/(v_0 - v_1)]^{1/2}. \quad (2.2.5)$$

Since the initial unshocked state parameters are known, knowledge of the values of any two of the shocked state parameters is all that is needed to uniquely define all of the parameters because of the conservation laws.

The set of shocked states that a medium can reach through a single shock wave from an initial state can be determined through series of experiments. The results of these experiments are usually presented in the form of pressure vs. specific volume, pressure vs. particle velocity, or shock velocity vs. particle velocity. These curves which give the response of the particular medium to shock waves are referred to as the Hugoniot of the medium. The Hugoniot of many types of materials have been experimentally determined and tabulated [2,3]. The various Hugoniot curves convey the same information but are useful for different applications. The pressure vs. specific volume curve is used for internal energy considerations and will be discussed further in section 2.3. The pressure vs. particle velocity curve represents the shock impedance, analogous to acoustic impedance (see eq. 2.2.2).

This curve is useful for calculating the shock states produced in flyer impact experiments. This procedure is discussed in section 2.6. One must note that the Hugoniot of a material depend on the initial state. Thus a material already in a shocked state will follow a different set of curves, although the difference is negligible when there is minimal shock heating.

2.3 Thermal Shock Energy

For non-gaseous media, the increase in the internal energy due to the passage of a shock wave (see eq.2.2.3) includes both the elastic energy as well as the thermal energy. In the shock consolidation process, the thermal energy is more relevant since we are interested in the melting and bonding of powder particles. This separation in energy can be formally written as

$$E_1 - E_0 = E_e + E_T \quad (2.3.1)$$

where the subscripts e and T stand for elastic and thermal, respectively. In the strict sense, the elastic and thermal energies cannot be completely separated since there are cross terms. However, these cross terms are usually absorbed into the definition of the thermal energy term so that E_e has only volume dependence while E_T has both volume and temperature dependence. In practice these cross terms are usually small, especially in the case of porous media.

Similarly the shock pressure can also be broken down into the elastic and thermal components and can be written as

$$P_1 - P_0 = P_e + P_T \quad (2.3.2)$$

since P is equal to the negative of the partial derivative of E with respect to V . Much of the theoretical and experimental work in shock wave physics of solid media have involved attempts to find the relationships between the various terms of eqs. 2.3.1 and 2.3.2, i.e., the equation of state of media under high pressure and temperature [4-7].

Equations 2.3.1 and 2.3.2 can be better understood by looking at figure 2.2 which shows the pressure vs. volume diagram for a solid medium shocked from the (P_0, V_0) state to the (P_1, V_1) state. The amount of separation among the various curves in the figure has been exaggerated from realistic differences to better illustrate the concepts. The total internal energy gain is equal to the area of the shaded triangle. The isentropic curve is the path followed if the material was isentropically compressed. The isothermal curve is the path followed if the material was compressed under constant temperature conditions. The difference between the isothermal and isentropic curves arises from the cross terms which link the elastic and thermal energies. The vertically striped region corresponds to energy by the dissipative mechanisms in the shock front. The horizontally striped region is usually referred to as the elastic or nonthermal energy of the shock. Typically in solid media, the nonthermal component dominates for low pressure and both terms are comparable only at pressures of hundreds of gigapascals. Thus in solids, extracting the thermal component from the total energy requires accurate knowledge of the high pressure interatomic potential of the material.

The residual heating left in a shocked solid which is released back

to P_0 is schematically illustrated in Fig. 2.3. Unlike the compression which is a shock wave, the release waves for normal material are dispersive in nature. The residual thermal energy is equal to the difference in areas between the two shaded regions in the figure (vertically stripped area minus the horizontally stripped area). The value of $V_R - V_0$ depends on the thermal expansion coefficient and the residual energy. Solid copper shocked to 10 GPa has a temperature rise of 39 C, but when released to zero pressure has a residual temperature rise of only 6 C [4]. Thus for pressures of interest in shock consolidation of powders, both the shock heating and the residual energy after release are very small in a solid.

2.4 Powder Hugoniot

The basic ideas used in constructing the shock Hugoniot of a powder medium are well known [1]. Nonetheless, applications of these ideas usually result in unwieldy equations and involve several empirically derived thermodynamic variables [8,9,10]. Recently, however, a simple but accurate analytical model for the shock Hugoniot of a powder medium has been introduced [11]. This model will be used in our treatment of shock wave consolidation. The present section will describe the basic ideas and their application in constructing the shock Hugoniot for powders.

Since P_0 is normally one atmosphere (10^{-4} GPa), we can neglect P_0 in comparison to P_1 . Thus eq. 2.2.3 can be combined with eq. 2.3.1 and written as

$$E_T = \frac{1}{2} P_1 (V_{00} - V_1) - E_e \quad (2.4.1)$$

for powder media. V_{00} is the initial specific volume of the powder. V_0 will now refer to the solid specific volume of the material. The thermal energy, E_T , is related to the thermal pressure, P_T , by

$$P_T = \gamma_1 E_T / V_1 \quad (2.4.2)$$

which is the Mie-Gruneisen formulation for the equation of state [1]. γ_1 is known as the Gruneisen coefficient and is defined thermodynamically as

$$\gamma = v \left(\frac{\partial P}{\partial E} \right)_v = \frac{v \chi}{\eta_T C_v} \quad (2.4.3)$$

The volume thermal expansion coefficient, χ , is defined by

$$\chi = \frac{1}{V} \left(\frac{\partial V}{\partial T} \right)_P$$

The isothermal compressibility, η_T , is defined as

$$\eta_T = - \frac{1}{V} \left(\frac{\partial V}{\partial P} \right)_T$$

Finally, C_v is the specific heat capacity at constant volume.

The Mie-Gruneisen equation of state can be derived by treating the solid as a collection of semiclassical harmonic oscillators with a different frequency for each atomic vibrational mode of the solid. The fractional change in frequencies due to changes in volume is assumed to be the same for all the oscillators [12]. The Gruneisen coefficient, whose statistical mechanics definition is the logarithmic derivative

of the frequency with respect to volume, typically varies in value from 1.5 to 2.5 for most metals. The Gruneisen coefficient is a function of volume only [4] in the Mie-Gruneisen theory and is usually treated as an empirically determined parameter.

In order to treat the nonthermal component in eq. 2.4.1, a basic difference between the shocked state of a solid and that of a powder medium has to be exploited. The shock consolidation of a powder medium results in a volume change much larger than that accompanying the shock compression of a solid of the same material. As a result, a relatively large amount of work is expended irreversibly compacting the initially porous medium, and thus the thermal energy component of eq. 2.3.1 is dominant even at modest shock pressures, unlike the situation for solids. This fact is illustrated by the schematic pressure vs. volume diagram shown in Fig. 2.4. The diagram shows a powder medium at an initial specific volume of V_{00} being shock consolidated to a volume V_1 by a single shock wave of amplitude P_1 . The powder Hugoniot is shown to originate from V_0 although the true curve should originate from V_{00} . This difference is represented by the dashed line in Fig. 2.4. This so-called crush-up approximation [13] is justified when the pressure required to go from V_{00} to V_0 is negligible compared to P_1 . The lower pressure limitation imposed by the above approximation depends on the material but is typically less than 1 GPa.

The elastic terms are not as important as the thermal terms. Therefore, a first-order model for the relation between P_e and E_e should be sufficient to describe the elastic behavior of the powder media. Thus the pressure and volume may be linearly related by

$$P_e = \frac{V_0 - V_1}{V_0 \eta_s} \quad (2.4.4)$$

where η_s is the isentropic compressibility of the solid medium. The isentropic compressibility is related to the speed of sound, a_0 , by

$$\eta_s = \frac{V_0}{a_0^2} \quad (2.4.5)$$

The elastic energy is then derived by calculating the elastic work done in compressing the solid from V_0 to V_1 and is given by the expression,

$$E_e = \frac{1}{2V_0 \eta_s} (V_0 - V_1)^2 \quad (2.4.6)$$

Using eqs. 2.3.2, 2.4.1, 2.4.2, 2.4.4, and 2.4.6 and keeping only first-order terms in $V_0 - V_1$, the shock Hugoniot for a powder becomes

$$\frac{V_1}{V_0} = \frac{1 + \gamma_1 m P_1 \eta_s / 2}{1 + (1 + \gamma_1 / 2) P_1 \eta_s} \quad (2.4.7)$$

where

$$m = V_{00} / V_0 \quad (2.4.8)$$

is called the distension of the powder. Typically for metals $\eta_s = 10^{-2}$ GPa and the pressures of interest for shock consolidation are usually less than 20 GPa. Thus at $P_1 = 20$ GPa with $m = 1.69$ and $\gamma = 2$, evaluation of eq. 2.4.7 gives 0.96, which justifies keeping only the first-order terms in $V_0 - V_1$. However, for very large distension and pressure, the volume approximation becomes a poor one. This particular

model for the Hugoniot of a powder medium is valid when

$$|P_1 \eta_S [1 - \gamma_1 (m - 1)/2]| \ll 1 \quad (2.4.9)$$

and

$$P_1 > P_{\text{crush-up}} \quad (2.4.10)$$

The first condition is obtained by expanding eq. 2.4.7 and requiring $V_1/V_0 \approx 1$. The second condition comes from the crush-up approximation discussed earlier.

Equation 2.4.7 can be substituted into eq. 2.2.4 to get

$$u_1^2 = P_1 V_0 \left[\frac{m(1 + P_1 \eta_S) - 1}{1 + (1 + \gamma_1/2)P_1 \eta_S} \right] \quad (2.4.11)$$

which is the shock impedance relation for powder media. The shock velocity relation for powder media becomes

$$C_S^2 = m^2 P_1 V_0 \left[\frac{1 + (1 + \gamma_1/2)P_1 \eta_S}{m(1 + P_1 \eta_S) - 1} \right]. \quad (2.4.12)$$

For a given material, a constant γ can be used since the equations are accurate only to the first order in $V_0 - V_1$. Comparisons of the model predictions with experimental data for porous copper, iron, tungsten, and aluminum give good agreement over a wide range of pressures, although the values of the isentropic compressibilities were slightly altered to improve the fit of the model to the data [11]. The fit of the model to porous copper data is shown in Fig. 2.5.

2.5 Homogeneous Shock Temperature

Although the initial thermal energy deposition in the powder after the passage of a shock wave is inhomogeneous, the shocked sample will reach a homogeneous temperature via heat conduction. This homogeneous temperature depends on the total thermal energy deposited by the shock wave. The total shock energy gain can be calculated with the use of eqs. 2.2.3 and 2.4.7. From the arguments given in section 2.4, it is clear that most of the the internal energy is thermal. Thus with very little knowledge of the details of the shock energy deposition mechanisms, the homogeneous temperatures produced in shocked powder media can be calculated. The formalism for calculating the homogeneous shock temperature in solids will be first introduced [14], and then the approximations valid for powder media will be applied.

The first law of thermodynamics in the differential form is

$$dE = TdS - PdV$$

which can be rewritten as

$$dS = \frac{1}{T} dE + \frac{P}{T} dV \quad (2.5.1)$$

where S is the entropy per unit mass. Consider the internal energy and entropy when they are functions of only the temperature and volume. Thus one can expand dS as

$$dS = \left(\frac{\partial S}{\partial T}\right)_V dT + \left(\frac{\partial S}{\partial V}\right)_T dV . \quad (2.5.2)$$

From eq. 2.5.1, we have the relation

$$\left(\frac{\partial S}{\partial T}\right)_V + \frac{1}{T} \left(\frac{\partial E}{\partial T}\right)_V = \frac{1}{T} C_V.$$

The thermodynamic state variables S, T, V, and P are related by the well known Maxwell's relations [15], one of which is

$$\left(\frac{\partial S}{\partial V}\right)_T = \left(\frac{\partial P}{\partial T}\right)_V.$$

The derivative of P with respect to E at constant V can be written as

$$\left(\frac{\partial P}{\partial E}\right)_V = \left(\frac{\partial T}{\partial E}\right)_V \left(\frac{\partial P}{\partial T}\right)_V = \frac{1}{C_V} \left(\frac{\partial P}{\partial T}\right)_V.$$

Thus, using the definition of γ (see eq. 2.4.3) and the above relations, we can rewrite eq. 2.5.2 as

$$dS = \frac{1}{T} C_V dT + \frac{\gamma C_V}{V} dV. \quad (2.5.3)$$

Equation 2.5.3 can be combined with eq. 2.5.1 to get

$$dE = C_V dT + (P - \gamma C_V T/V) (- dV) \quad (2.5.4)$$

which is the basic relation to be used in the shock temperature calculations.

The significance of the differential volume term is made clear by noting that the $\gamma C_V T/V$ term corresponds to the thermal pressure for a Mie-Gruneisen solid discussed in section 2.4. Thus the differential

volume term is simply the contribution of the elastic energy to the total shock energy. In the crush-up approximation, the elastic energy of the powder is equal to that of an elastically compressed solid. For powder media, this term is small compared to the total internal energy. Consider the typical case when copper powder of $m = 1.69$ is compacted by a 10 GPa shock wave. The elastic energy gain in the shocked state is approximately 3 kJ/kg (from eq. 2.3.6) while the total energy gain is 400 kJ/kg (from eq. 2.2.3). Thus the elastic energy term can be neglected. This approximation leads to a very simple relation for the homogeneous temperature rise in shocked powder media and is given by

$$\int_{T_0}^{T_1} C_V dT = \frac{1}{2} P_1 V_0 (m - V_1/V_0) \quad (2.5.5)$$

which slightly overestimates the temperature rise. Equation 2.5.5 predicts that the homogeneous temperature of the copper powder in the above mentioned example will rise about 1000 K. Recall that solid copper shocked to 10 GPa has a temperature rise of only about 39 K.

The regimes under which eq. 2.5.5 is valid are given by the condition that

$$P_1 (m - V_1/V_0) \gg \frac{1}{\eta_s} (1 - V_1/V_0)^2. \quad (2.5.6)$$

The above condition is derived by requiring that the total shock energy given by eq. 2.2.3 be much greater than the approximate elastic energy relation of eq. 2.5.6.

Another aspect of the fact that the shock heating in a solid is

small compared to that in powder is that, after the passage of the initial shock wave, subsequent shocks or release waves do not significantly alter the total amount of thermal energy. This is true only if the powder medium acts as a solid after the passage of the first shock wave. Thus the initial shock wave is of primary importance in shock wave consolidation. In addition the homogeneous temperature should not vary except for a few tens of degrees after the initial shock. This makes the experimental measurement of the temperature much simpler and will be discussed in the next chapter.

2.6 Impedance Matching Calculations

The shock state attained by a material under the plane impact of a high velocity flyer can be determined by imposing boundary conditions at the impact interface for the propagation of a steady shock wave. These boundary conditions are that the shock pressure and particle velocity must be the same on both sides of the interface. If the shock impedance curves for the two materials are known, then the continuity conditions coupled with the impact velocity are sufficient to uniquely define the shock state produced by the impact. Figure 2.6 schematically illustrates the technique.

Consider the case where a steel flyer with a 1.2 km/s velocity impacts a steel powder layer backed by a steel base (see Fig. 2.7). This is a typical geometry used in many of our recovery experiments described in Chapter 4. The graphical representation in which the continuity conditions are used to determine the shock states produced in the above mentioned example is shown in Fig. 2.8. The powder is initially at state 00 and the flyer is at state 6. After the impact, a shock wave travels into the flyer in the opposite direction to the shock

wave traveling into the powder. These shocks take the flyer and powder to shock state 1. The position vs. time diagram for the propagation of the shock fronts is shown in Fig. 2.9 where the encircled numbers correspond to the shock state shown in Fig. 2.8. The shock velocities required for constructing the diagram are obtained from equations introduced in sections 2.2 and 2.4 and the information in Fig. 2.8. Subsequent reflections of the shock waves from the base and the free surface at the rear of the flyer produce other shock states as shown in the diagram. Figure 2.10 gives the pressure vs. time history experienced at the impact face and at the powder-base interface. The pressure history information was obtained from Fig. 2.9. Although the initial shock pressure state is the most relevant in terms of thermal energy deposition which bonds the powder particles together, knowledge of the subsequent shock history is crucial for designing experiments in which the consolidated powder is to be recovered with minimal damage. For example, the duration of the compressive shock state can be obtained from Fig. 2.10 (or Fig. 2.9) and depends on the thickness of the flyer. Such information is important for the modeling of the conditions required for successful powder consolidation which is discussed in Chapter 5.

Except for the initial shock wave calculation which is as accurate as the shock impedance information, the subsequent shocked states are approximate since several assumptions were made in order to calculate them. The assumptions are: 1) the powder layer acts as a solid after the first shock, 2) the heating of the solid only shifts the Hugoniot and does not affect their slope, and 3) the release waves follow the shape of the shock Hugoniot.

All of the above mentioned shock states are correct only if the one-dimensional flow conditions are realized. Since the flyers are of a finite diameter, disturbances will propagate into the impacted material from these edges and will change the one-dimensional nature of the shock state. In certain areas of the sample near the edges and away from the impact face, the edge waves arrive before the one-dimensional shock waves calculated by the impedance matching method described earlier. These areas can be delineated from the areas in which the initial shock state is one-dimensional (and thus well-defined) by a cone depicted in Fig. 2.11. The angle of the cone is given by [7]

$$\cot \theta_e = \left[\left(\frac{c_s}{a_1} \right)^2 - \left(\frac{c_s - u_1}{c_s} \right)^2 \right]^{1/2} \quad (2.6.1)$$

where a_1 is the speed of sound in the shocked medium and θ_e is the cone angle defined in Fig. 2.11. This equation is derived by assuming that the edge waves travel at velocity a_1 and that the initial medium is at rest. In a typical experiment, the values of a_1 , c_s , and u_1 are 4, 2, and 0.9 km/s, respectively. This gives a θ_e of 27 degrees.

The duration of the one-dimensional conditions before edge waves arrive depends on the exact location but is a maximum at the center of the impact face. The typical flyer diameter was 16 mm and resulted in a duration of well-defined shock conditions of about 2.5 μ s at the center of the impact face.

In the case when the shock Hugoniot of the powder material is unknown but the shock Hugoniot of the flyer material is known, the initial shock state can be determined by measuring only one of the shock

state parameters. For example, if the shock velocity is measured, the shock state can be determined by using eq. 2.2.2, the flyer velocity, and the shock impedance of the flyer. This calculation is illustrated in Fig. 2.12. This technique is often used to measure the shock Hugoniot of materials since it requires only one shock parameter measurement per experiment to determine a point on the shock Hugoniot [16].

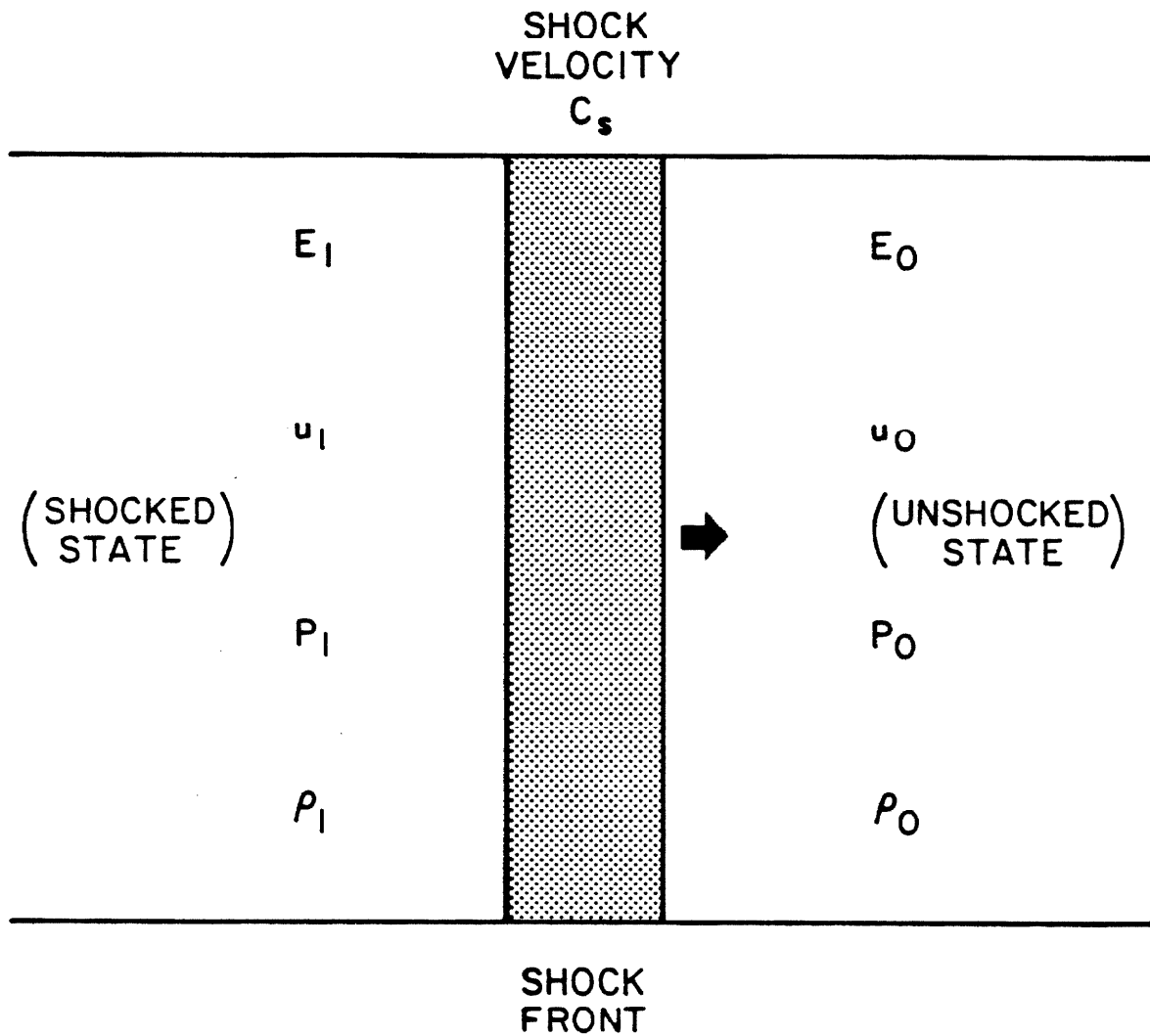


Fig. 2.1 Schematic drawing of a shock wave traveling to the right. E , u , P , and ρ stand for specific internal energy, particle velocity, pressure, and mass density, respectively.

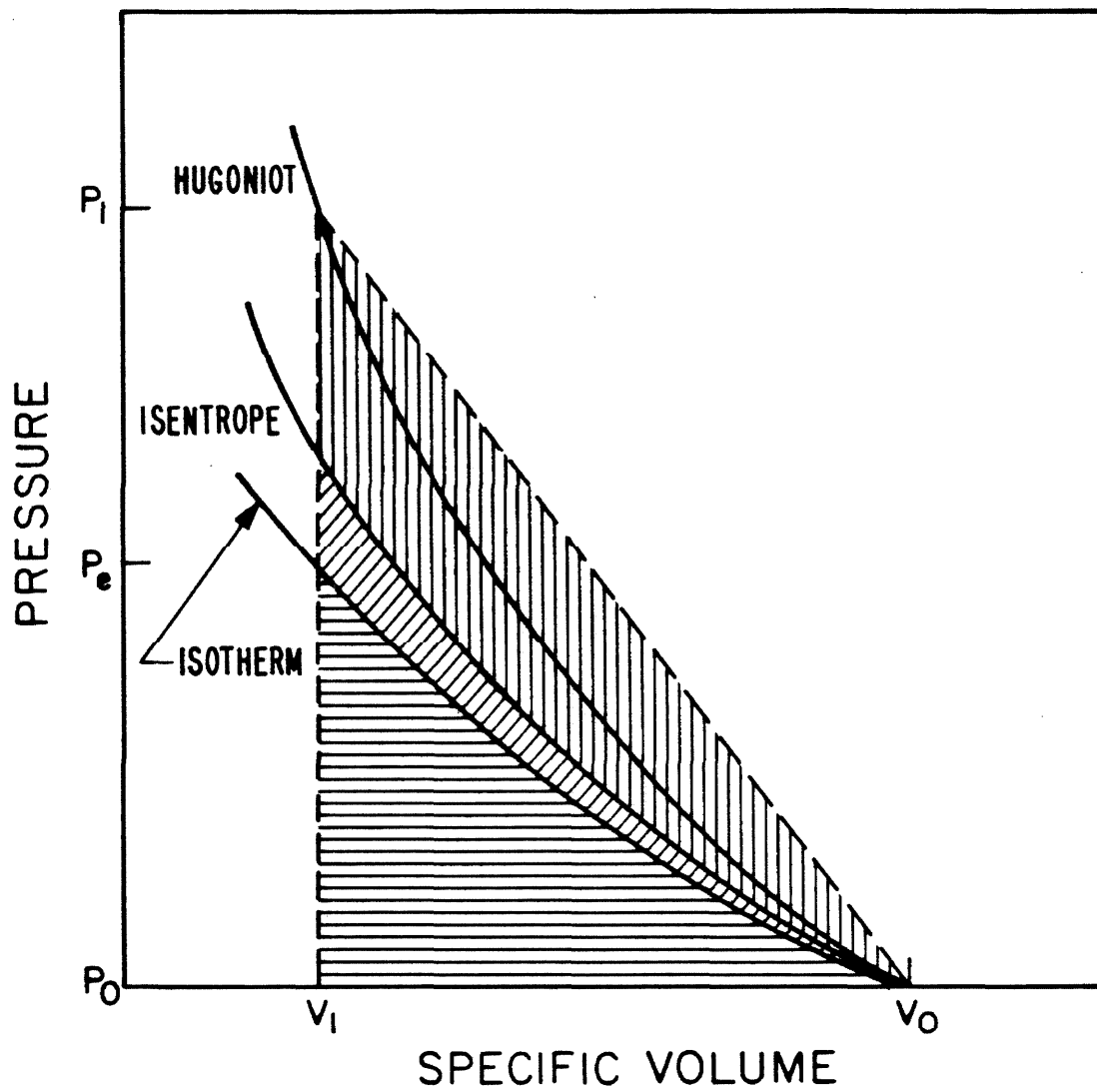


Fig. 2.2 Schematic diagram of shock pressure vs. specific volume for a shocked solid.

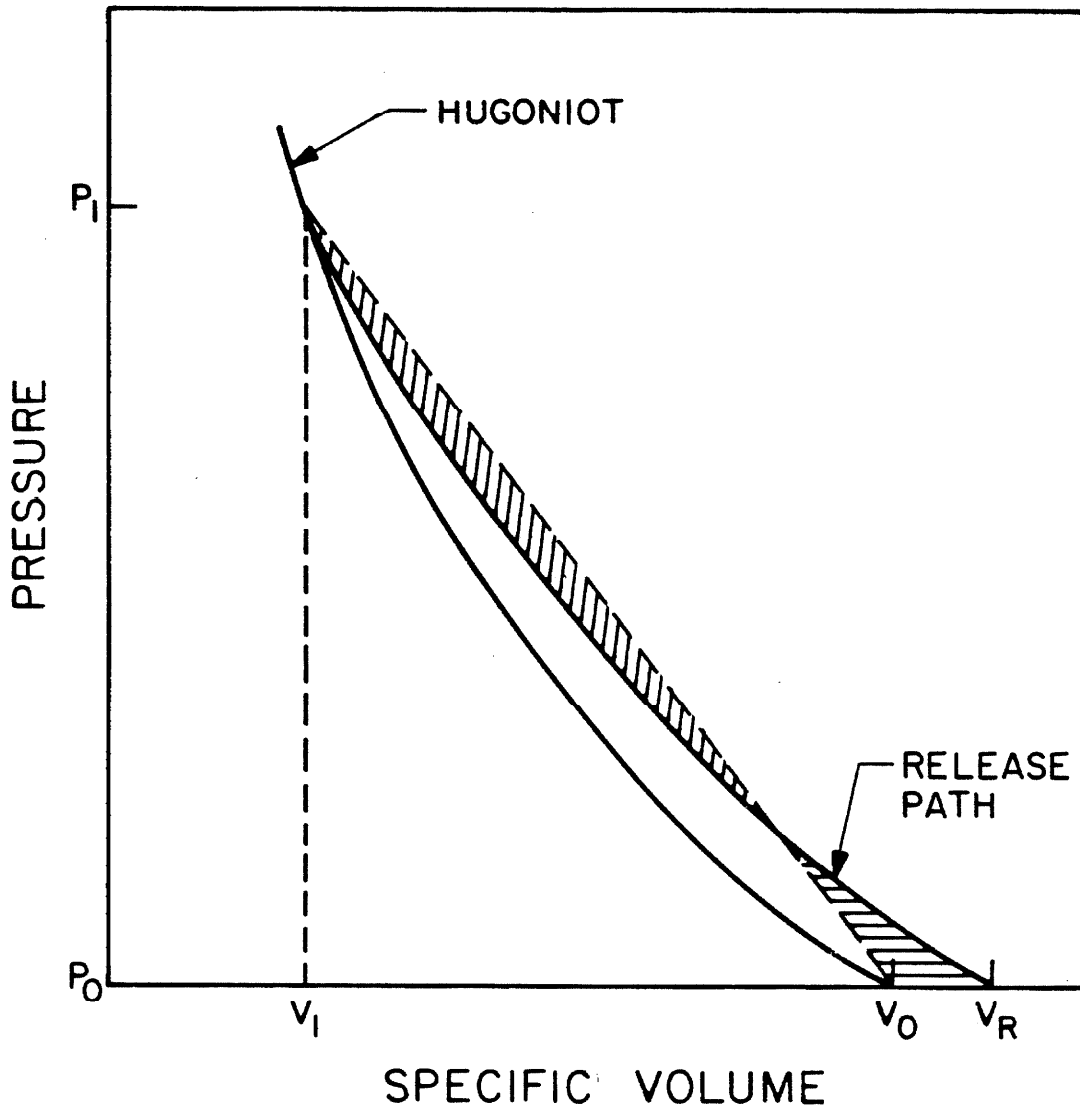


Fig. 2.3 . Schematic diagram of pressure vs. volume for a solid which is released from the shocked state.

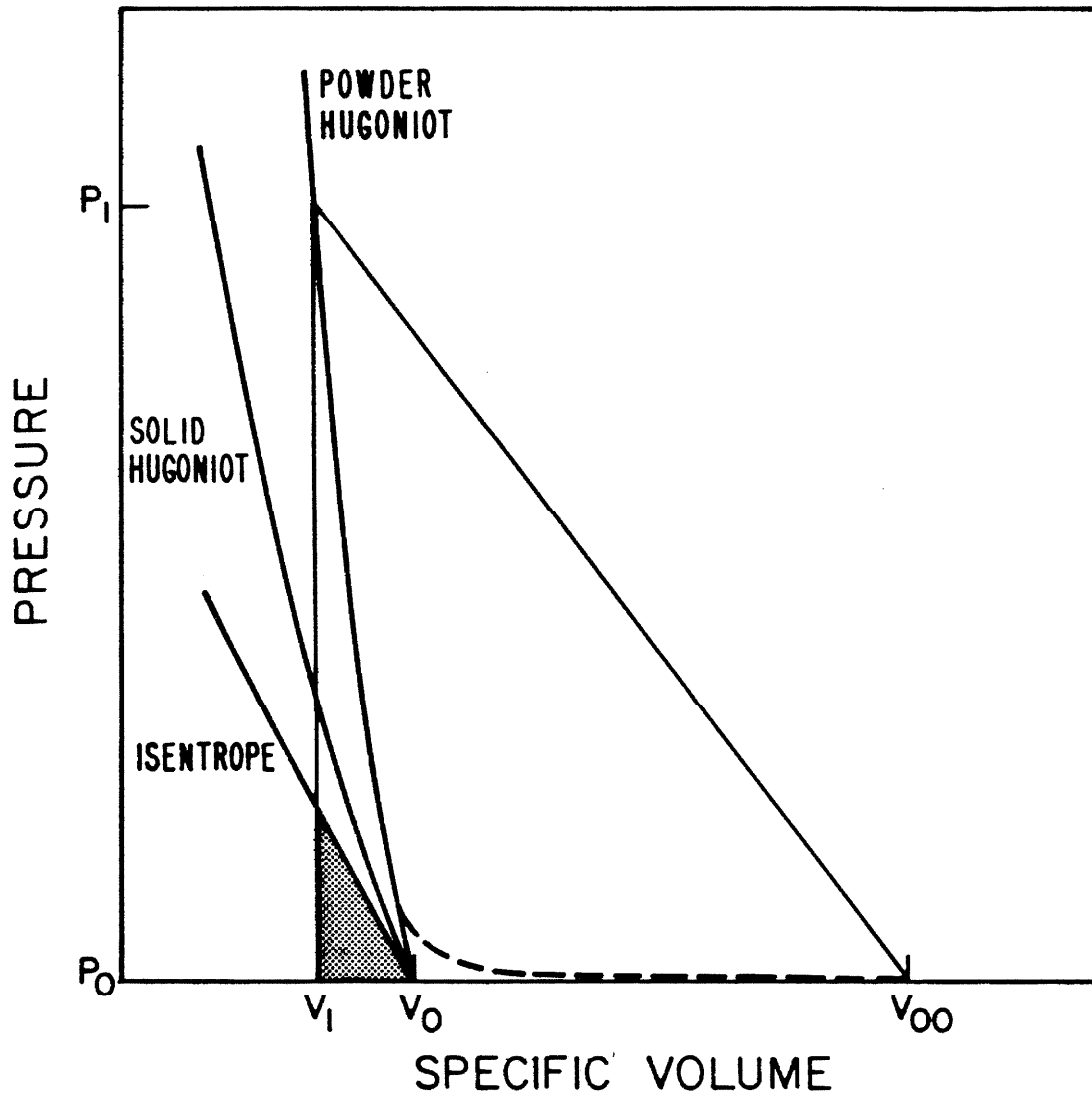


Fig. 2.4 Schematic diagram of pressure vs. volume for a shocked powder medium.

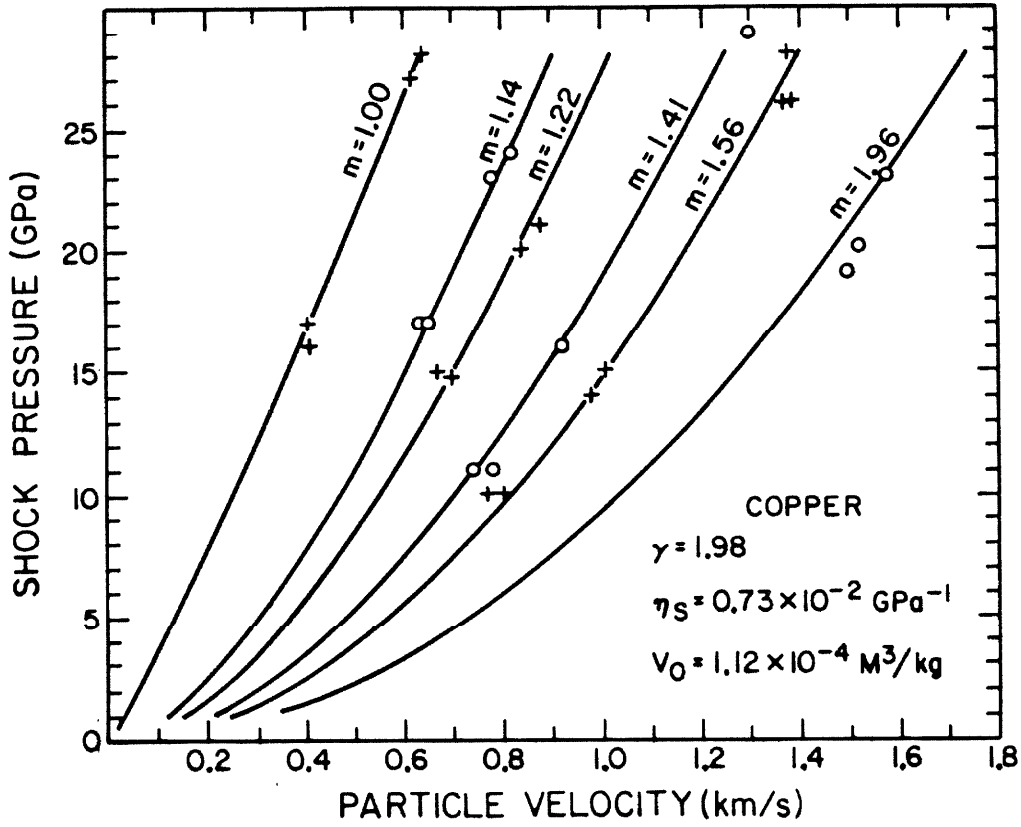


Fig. 2.5 Shock impedance data for solid and porous copper [4]. The solid lines are from the porous Hugoniot model described in text. The values used for γ , η_s , and V_0 are 1.98, 0.0073 GPa^{-1} , and 1.12×10^{-4} , respectively [11].

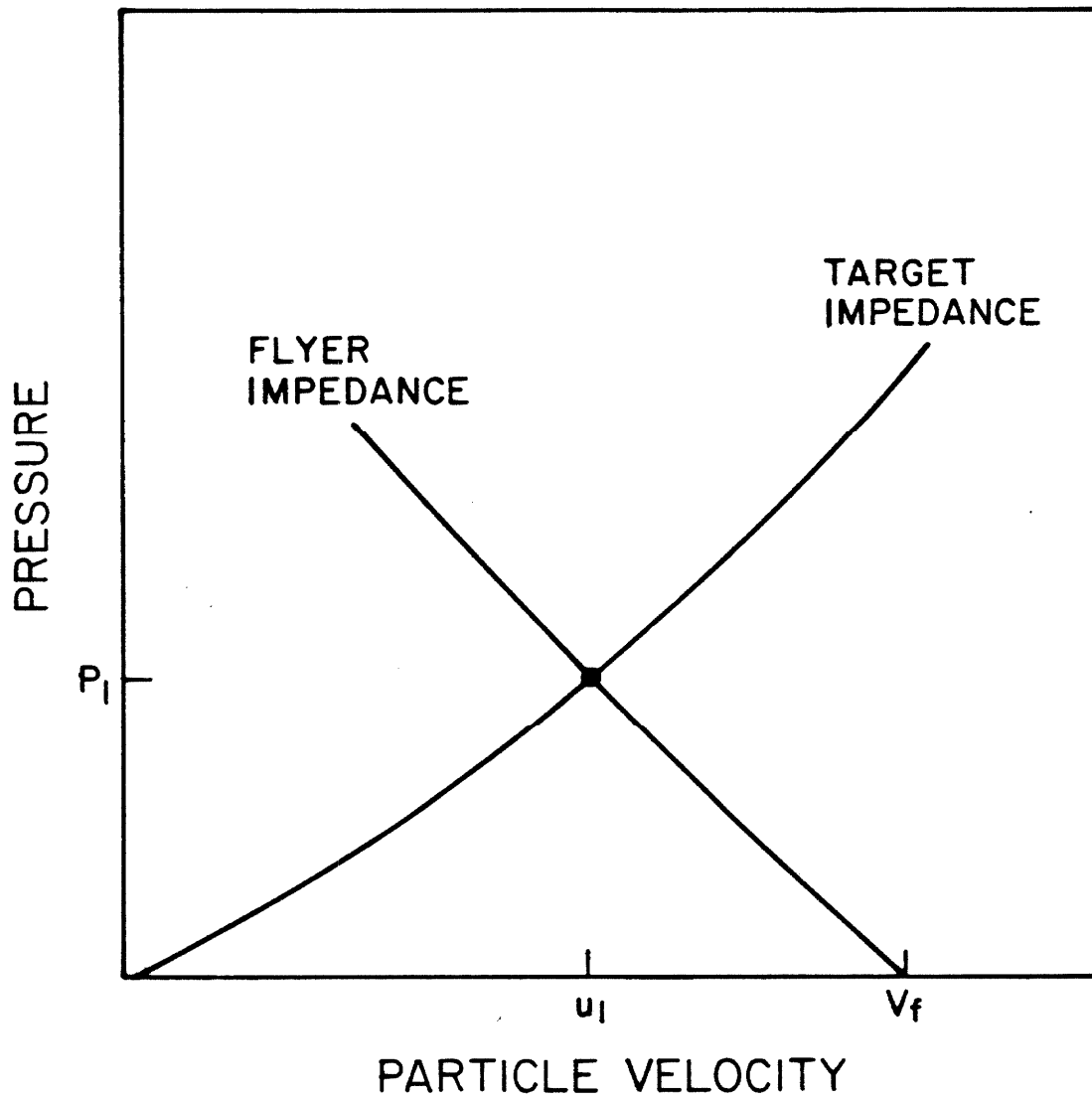


Fig. 2.6 Schematic diagram showing the shock state (P_1, u_1) produced by the impact of a flyer on a target. v_f is the flyer velocity.

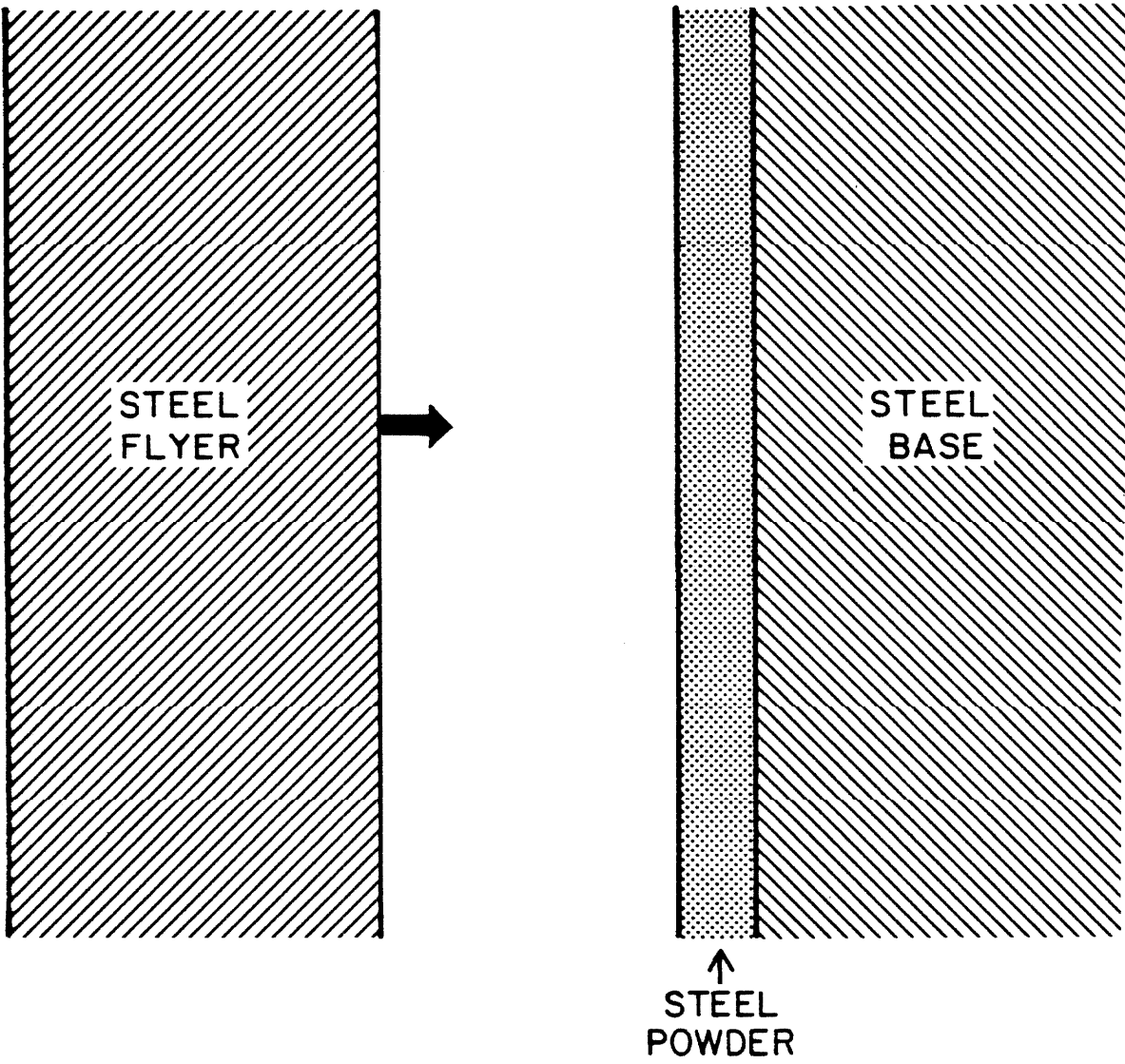


Fig. 2.7 Schematic drawing of a steel flyer plate impacting a steel powder layer which is backed by a steel base.

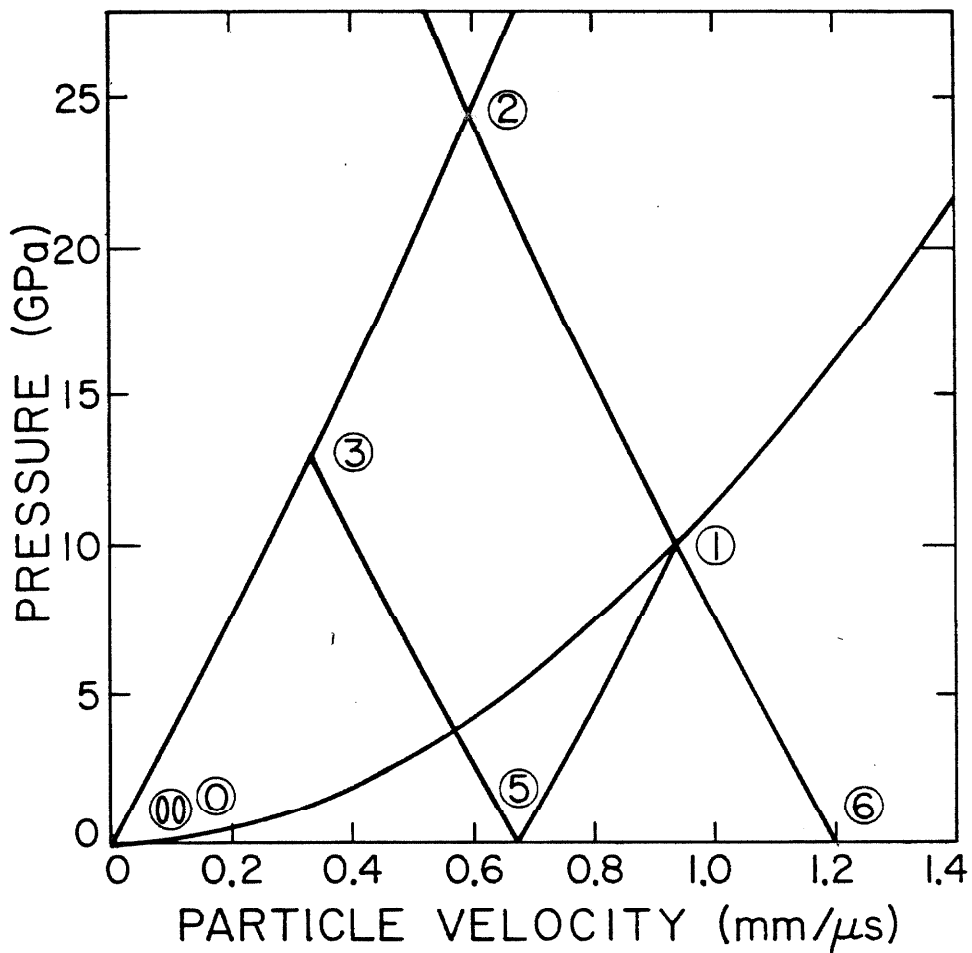


Fig. 2.8 The impedance curves used in calculating the shocked states produced in the experiment depicted in Fig. 2.7 with a flyer velocity of 1.2 km/s.

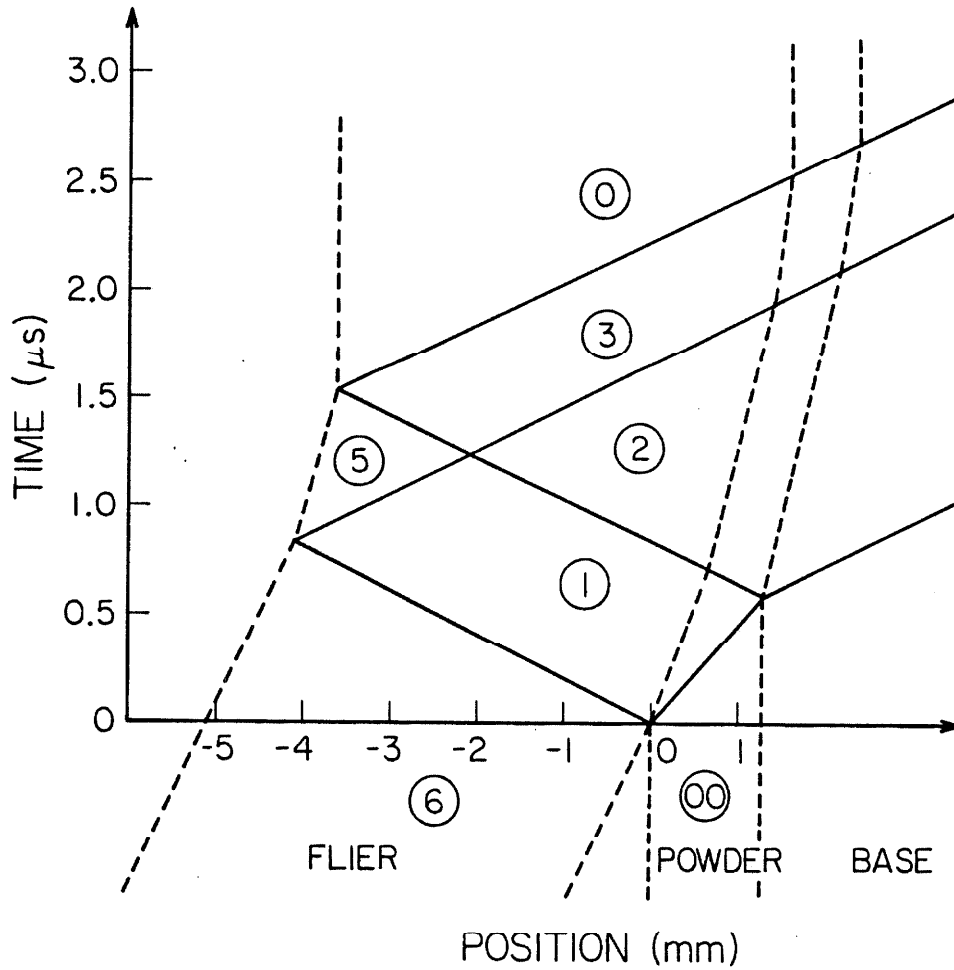


Fig. 2.9 The position vs. time diagram of the shock fronts and release waves produced in the experiment depicted in Fig. 2.7. The encircled numbers correspond to the shock states shown in Fig. 2.8.

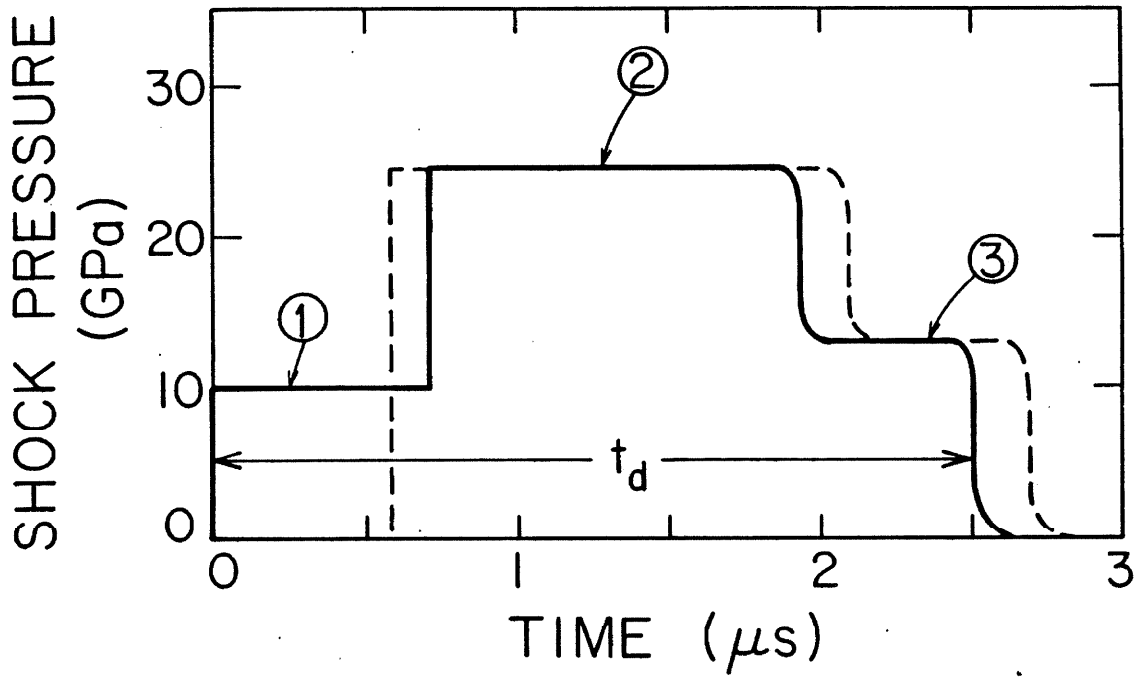


Fig. 2.10 Pressure-time history in the shocked powder at the surface of impact (solid line) and at the surface of contact with base (dashed line). This diagram follows from analysis shown in Fig. 2.9.

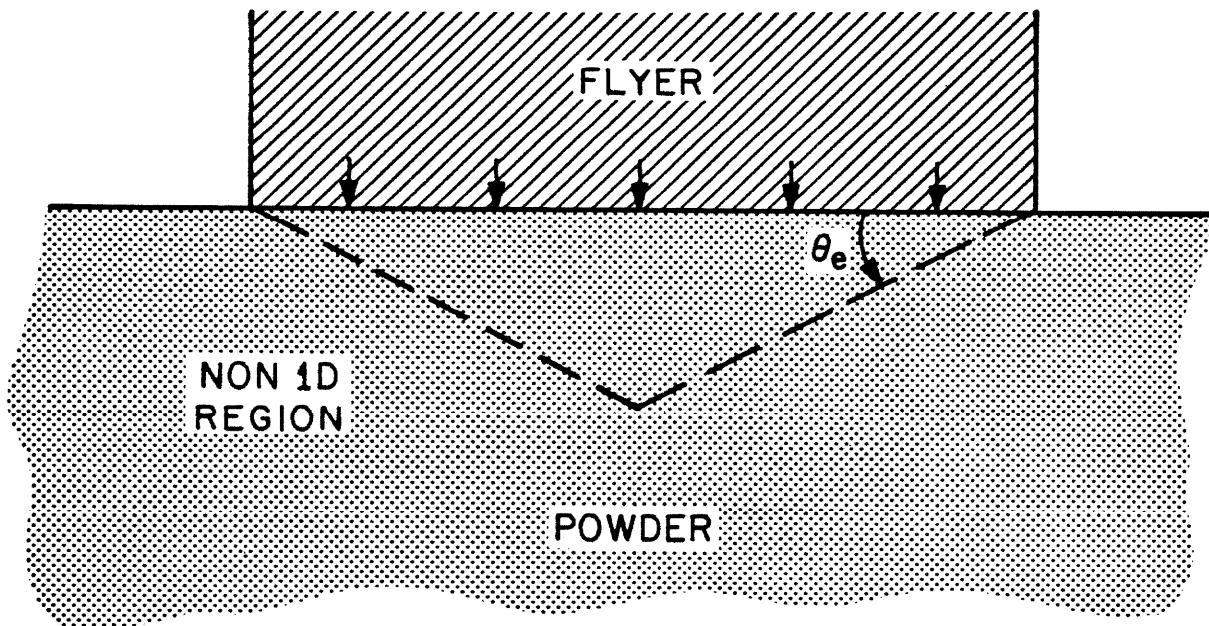


Fig. 2.11 Schematic depiction of cone-like volume in which the one-dimensional analysis of shock wave propagation is valid. The duration of the one dimensional conditions inside of the cone depends on the location and speed of the edge disturbances.

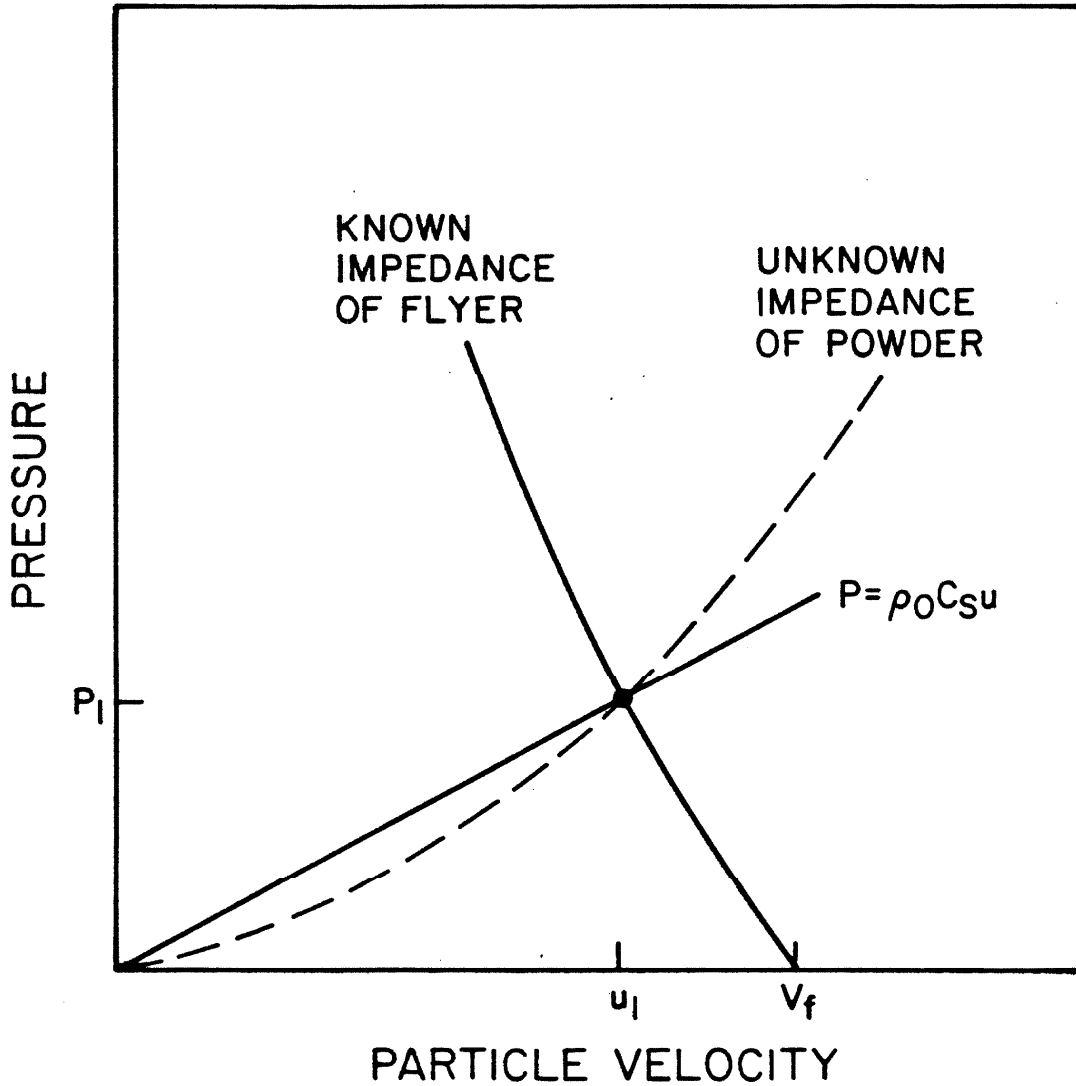


Fig. 2.12 Schematic diagram of how the shock state (P_1, u_1) produced by the impact of a flyer (whose shock impedance is known) on a powder medium (whose shock impedance is unknown) can be determined by measuring the shock velocity C_s and flyer velocity V_f .

CHAPTER 2 REFERENCES

1. Zel'dovich, Y. B. and Y. P. Raizer, Physics of Shock Waves and High-Temperature Hydrodynamic Phenomena, Vol. I and II, Academic Press, San Francisco, 1967.
2. Kinslow, R., ed., High-Velocity Impact Phenomena, Academic Press, New York, 1970.
3. Marsh, S. P., ed., LASL Shock Hugoniot Data, University of California Press, Los Angeles, 1980.
4. McQueen, R. G., S. P. Marsh, J. W. Taylor, J. N. Fritz, and W. J. Carter, in High-Velocity Impact Phenomena, R. Kinslow, ed., Academic Press, New York, 1970.
5. Davison, L. and R. A. Graham, Phys. Report, 55, 943 (1982).
6. McQueen, R. G. and S. P. Marsh, J. Appl. Phys., 31, 1253 (1960).
7. Al'tshuler, L. V., S. B. Kormer, M. I. Brazhnik, L. A. Vladimirov, M. P. Speranskaya, and A. I. Funtikov, Sov. Phys. JETP, 11, 766 (1960).
8. Herrman, W., J. Appl. Phys., 40, 2490 (1969).
9. Davison, L., J. Appl. Phys., 42, 5503 (1971).
10. Drumheller, D. S., Int. J. Solids Structures, 14, 441 (1977).
11. Simon, G. A. and H. H. Legner, J. Appl. Phys., 53, 943 (1982).
12. Gruneisen, E., Handbuch der Physik, 10, 22 (1962).
13. Linde, R. K. and D. N. Schmidt, J. Appl. Phys., 37, 3259 (1966).
14. Walsh, J. M. and S. P. Marsh, Phys. Rev., 97, 1544 (1955).
15. Pippard, A. B., The Elements of Classical Thermodynamics, Cambridge University Press, New York, 1964.
16. Walsh, J. M., M. H. Rice, R. G. McQueen, and F. L. Yarger, Phys. Rev., 108, 196 (1957).

CHAPTER 3

SHOCK TEMPERATURE MEASUREMENTS

3.1 Introduction

The passage of a shock wave through a porous medium causes inhomogeneous heating of the individual powder particles. The areas which correspond to the powder particle surfaces in the uncompact state will be the hottest, while interiors will be relatively cool. However, with the conduction of heat, the shocked sample will approach a homogeneous temperature which reflects the total energy deposited by the shock wave. Therefore, if one knows the specific heat of the medium, the measurement of the homogeneous temperature attained by the shock consolidated sample can be used to calculate the irreversible energy input by the shock wave.

In this chapter, the temperature measurements in copper powder shocked from 1.3 to 9.4 GPa (50 to 360 kJ/kg shock energy, respectively) are described and presented. Such measurements are necessary to check the validity of the shock conservation laws introduced in Chapter 2 when applied to powder compaction. Furthermore, the fundamental assumption that total densification occurs during the passage of the first shock can be tested. Although these assumptions are usually made in the treatment of shock consolidation of powders, they had not been verified until the present study. In addition, if the shock rise-time could also be determined during the temperature measurements, useful insights into the nature of the particle

deformation mechanisms could be gained.

3.2 Temperature Measurement Techniques

The nature of shock wave experiments makes temperature measurements difficult. The time scales involved are very short (typically 10^{-7} seconds or less), and any temperature measuring device must withstand very high pressures (> 1 GPa). Presently three different physical effects have been used to measure temperature in shocked nonporous media: 1) the emission of thermal radiation, 2) the temperature dependence of electrical resistivity, and 3) the thermoelectric effect. However, temperatures in shocked powder media have not been reliably measured. The ideal technique for shock consolidation of metallic powders should be able to measure temperatures in the 300-1800 K range, produce negligible disturbance of the shocked state in the powder, and have less than 10 nanosecond response time. The technique described in this chapter satisfied most of these conditions. First, however, other currently used techniques to measure shock temperature will be reviewed and their applicability to our present situation evaluated.

The optical pyrometry technique was developed when investigators observed that highly shocked transparent dielectrics emit characteristic blackbody radiation [1,2]. Thus, by measuring the blackbody curve, one can deduce the temperature. An advantage of this technique is that no in situ devices have to be introduced into the media which might affect the shocked state and thus the temperature being measured. This technique has been extended to opaque media with the use of transparent windows which allow the media to remain in a shocked state while still permitting the emission of observable thermal radiation [3-5]. Temperatures of shocked opaque media after release from the shocked

state have also been measured using the optical pyrometry technique [6]. The main limitations of the technique are that temperatures above several thousand degrees Kelvin are required for reliable and unambiguous results, and for opaque media the shock impedance of the window must be matched to prevent unwanted shock reflections at the window-medium interface.

The changes in electrical resistivity of metallic foils embedded in shocked media have been used to deduce temperature [7-9]. The foils were typically thicker than 5 μm because the devices must survive long enough (10^{-6} s) in order to obtain reliable and interpretable results. However, such large thicknesses produce slow thermal equilibration of the foils with the media, which prevents the measurement of the shock rise time. Furthermore, to prevent unwanted shock reflections, the shock impedance of the foil should be matched to the medium impedance which is difficult when dealing with metallic powders. In addition, converting the resistance change to a temperature change requires a fairly large pressure correction [10]. Thus the pressure dependence of the resistivity of the chosen foil material must be known to the accuracy desired for the temperature measurement.

There have been numerous attempts to measure temperatures in solid media with the use of embedded thermocouples. However, most of these experiments consistently measured higher temperatures than expected. Much of the discrepancy can be explained by localized heating near gaps and pores at the thermocouple-medium interface since those areas can absorb more shock energy than the solid medium [11]. Such effects can and have been minimized by careful fabrication of the thermocouple-medium interface [9,12]. The shock temperature of PMMA and epoxy have

been measured with the use of embedded 5 μm thick copper-constantan and chromel-alumel thermocouples [13]. However, these thermocouples had an anomalously fast rise times which the authors attributed to a factor of 10^3 increase in the thermal conductivity of PMMA and epoxy under shock loading [13]. Also the investigators reported that the temperature measurements depended on the orientation of the thermocouple with respect to shock wave direction [14]. Such effects, although very interesting to study, do not make the embedded thermocouple technique very attractive for measuring reliable and unambiguous shock temperatures. For a more thorough review of the history and problems of embedded thermocouple experiments, the reader is referred to reference [15].

3.3 Bimetallic Powder Thermocouple

Good and reliable temperature measurements can be made using the thermoelectric effect without the use of embedded foils in host media [11,16]. The basic method involves the use of the medium itself as one arm of the thermocouple. Figure 3.1 schematically illustrates the method. The material whose temperature is to be measured, metal A, is in contact with a metal B with similar shock impedance to metal A. Metal B is chosen such that the thermoelectric EMF between A-B is measurable for the temperature range under consideration. Furthermore, the temperatures produced in metal B under shock loading must be known. These conditions necessarily restrict this method to a few metallic media. Nonetheless, the purpose of present study is to improve our general understanding of shock wave travel through metallic powders and thus the restrictions are not too severe. Although this method has been previously applied only to solid media, it is equally valid for metallic

powders and will be the basis for the experiments described in this chapter.

The experiment is designed such that a plane shock wave enters metal B from metal A through a plane interface. With appropriate wiring and referencing of the thermoelectric voltage produced at the A-B junction, the temperature can be measured. Such a thermocouple can be made to survive for many microseconds. In addition, the intrinsic electrical response time of the voltage produced at the junction is very fast and is essentially limited by the recording oscilloscopes used in the experiment to about 3 ns. Nonetheless, the effective thermal response time is limited by the planarity and definition of the junction interface and by the tilt of the impinging planar shock wave with respect to the interface. With tilt, different parts of the junction are heated as the shock wave sweeps across the junction causing an effective temperature rise-time. However, by limiting the size of the active thermocouple junction, one can, in principle, reduce this rise-time to any desired value. The definition of the interface cannot be any smaller than the average size of the powder particle; thus under ideal conditions the optimum shock front width resolution limit of this method is the powder size.

The geometry of the junction is such that simple one-dimensional heat flow calculations are applicable. If the temperatures of the two metals are uniform after the passage of the shock wave, the time independent temperature of the junction, T_j , is related to the temperatures of the two metals by [17]

$$T_j = T_A - (T_A - T_B)/\beta \quad (3.3.1)$$

where β is given by

$$\beta = \frac{\kappa_A}{\kappa_B} \left(\frac{D_B}{D_A} \right)^{1/2} . \quad (3.3.2)$$

T, K, and D are the temperature, thermal conductivity, and diffusivity of the two metals, respectively. With the use of powders, equation 3.3.1 is valid only after the homogeneous temperature has been reached by both metallic powders. One should note that the larger the β , the closer the temperature of the junction is to that of metal A.

The metallic powders have to be nonferromagnetic since ferromagnetic materials produce electrical noises of equal magnitude to actual thermal EMF under shock loading [15]. The exact nature of the noise is not known but may be due to shock induced demagnetization from: 1) phase transition to a nonferromagnetic state (such as that caused by temperatures above the Curie temperature) or 2) magnetic anisotropy in which the direction of shock propagation becomes an easy axis of magnetization (thus causing an effective demagnetization in the transverse direction) [15]. This problem precludes the use of such metals as iron and nickel.

3.4 Experimental Method

For the present study, the set of metallic powders chosen was copper (as metal A) and constantan (as metal B), a nonferromagnetic alloy composed of 55% copper and 45% nickel, by weight. The thermoelectric power of the copper-constantan system is fairly large. Static pressure corrections for the copper-constantan thermocouple up to 7 GPa are available [18], and the correction is less than 10% for

pressures of interest. The shock impedances of copper and constantan are almost identical for the pressure range of interest [15]. The specific heat of constantan is only 10-20 % higher than copper. In addition, for the copper-constantan pair β is between 2 to 4; thus the junction temperature will be only about 5 % lower than that of the shocked copper powder.

The copper powder used in our experiments was obtained from Wilshire Chemical and had a nominal size of -100 mesh, i.e., particles which passed through 149 μm sieve openings. Figure 3.2 shows an SEM picture of the copper powder. Although the copper powder included many small particles as seen in Fig. 3.2, the dominant larger particles typically varied from 40 to 70 μm in size. The metallic compositional purity of the powder was 99.5% by weight.

Powder of constantan could not be obtained commercially. The present constantan powder was made by mechanical alloying pure copper and nickel powders, by a colleague at Argonne National Labs [19]. Loads of pure copper and nickel powders with a weight ratio of 55:45 and a total weight of ten grams were mixed in a laboratory ball mill. The ball mill is an apparatus containing a cylindrical hardened steel chamber with many hardened steel balls. The chamber is violently agitated, and the collisions of the balls pulverize the powders. As new and fresh surfaces of copper and nickel are produced, the powders alloy by interdiffusion. The progress of the reaction was monitored through X-ray diffraction patterns of the product, and the ball milling was continued until the dominant (111) lines of copper and nickel merged into one indistinguishable peak (see Fig. 3.3). The nonferromagnetic character of the final powder mixture was tested with a small permanent

magnet. Figure 3.4 shows an SEM picture of the constantan powder produced by the above mentioned process. Similar to the copper powder, the larger dominant particles vary from 30 to 90 μm in size as seen in Fig. 3.4. The voltage-temperature calibration for a copper-constantan powder thermocouple is plotted in Fig. 3.5 [20]. The influence of high pressure on the thermoelectric effect of the copper-constantan system is plotted in Fig. 3.6 [18].

Figure 3.7 shows a schematic cross-sectional view of the powder thermocouple assembly used in our experiments. The figure shows a flyer just before impact, a copper buffer plate, and the cylindrical powder pill which acts as the thermocouple as well as the powder medium being shock consolidated. This particular geometry was chosen for ease of fabrication and does not allow for the recovery of the consolidated powder. The density of the copper and constantan powder in the powder pill was 5.27 g/cm^3 which corresponds to a distension of $m = 1.69$. The experimental assembly included a thin enameled copper wire on the impact face which was used to trigger the oscilloscopes.

The effective diameter of the thermocouple junction was chosen to be 4.7 mm. Although, because of the tilt problem, one would like this diameter to be as small as possible, compromise with other considerations dictated the chosen size. Larger sizes are easier to fabricate and have smaller electrical impedances. The electrical impedance of the thermocouple should be much less than the 50 ohms of series resistance in the measuring circuit, in order to minimize the modulation of the thermocouple signal from resistive changes during the experiment. The electrical impedances of the powder thermocouples were typically less than 60 milliohms.

Appendix A gives more details of the powder pill fabrication procedure and reasons for particular design features. The buffer plate also had a vacuum chamber attached (not shown in Fig. 3.7) which allowed the powder pill to be evacuated to 60 μm Hg pressure prior to shock consolidation. Figure 3.8 shows a picture of the complete assembly before loading onto the 20 mm gun.

In the following discussion, the shock waves are all assumed to be plane. This is true only in a cone whose base coincides with the impacting face of the flyer. The angles of the cone can be calculated as discussed in section 2.6. The dimensions of the thermocouple pill were chosen such that the active copper-constantan powder interface lay within this cone. The critical cone is delineated by the dashed line in Fig. 3.7 for a typical experiment.

Flyers made from lexan, 2024 aluminum, and copper were used to generate the shock waves. The impact of the flyer with the buffer plate produces a shock wave whose amplitude is determined by the continuity conditions on the pressure and particle velocity at the impact face as shown in Fig. 3.9. Figure 3.9 contains the actual Hugoniot used in the calculations for an aluminum flyer. The buffer plate is shocked from the unshocked state, 00, to shock state 2 while the flyer is shocked from state 0 to state 2. When the shock front of amplitude P_2 arrives at the copper buffer-copper powder interface, a shock wave of amplitude P_1 enters the powder while a release wave travels back into the buffer plate and reduces the pressure from P_2 to P_1 . An insulating layer of alumina (Al_2O_3) powder was placed between the copper and constantan powder to reduce the effective thermocouple area to a region near the center of the pill where the initial shock is planar. When the shock

arrives at the copper powder-constantan powder interface, there is negligible shock reflection and a shock wave of amplitude P_1 continues on into the constantan powder. Since the copper buffer plate and the adjoining copper powder are held at ground potential, the thermoelectric EMF measured through the constantan will be negative. Although shortly thereafter ($1 \mu s$), the thermocouple junction will no longer be in shock state 1 because of release waves from the free surface edges of the powder pill and reflected shocks from the flyer, the temperature signal should not be affected very much if the first shock fully consolidated the powder. Subsequent shocks will change the temperature very slightly as discussed in section 2.5. The shock wave continuing on into the constantan powder quickly loses much of its strength since most of the constantan lay outside of the critical cone where edge effects cannot be neglected. When the weakened shock wave finally arrives at the back constantan-copper interface, a positive thermoelectric EMF is produced which reduces the larger negative voltage produced at the front copper-constantan interface. This defines the effective lifetime of the thermocouple measurement. Although this lifetime cannot be precisely calculated, a lower bound for the lifetime may be obtained by determining the transit time of an unweakened P_1 shock wave. The thickness of the constantan powder was chosen so that a $P_1 = 10$ GPa shock will take at least $2 \mu s$. The actual lifetimes will be longer, and in fact, experimental results (to be presented in section 3.6) indicate that thermocouple lifetimes are longer than $4 \mu s$.

3.5 Calculated Homogeneous Temperature

The homogeneous temperature of the shocked copper and constantan powder can be calculated from energy balance. The basis for these

temperature calculations was set forth in Chapter 2. In fact, one of the main goals of this chapter is to give experimental verification of those calculations.

In all of the experiments, the copper powder had an initial density of 5.27 g/cm^3 which corresponds to a distension of 1.69. The shock amplitude, P_1 , was calculated from the impedance matching method described in section 2.6. The temperature rise in copper and constantan was then calculated with the use of eq. 2.5.5. Figure 3.10 shows the specific heat at constant pressure, C_p , for copper and constantan. The specific heat data for nickel are included for comparison. The spike is associated with the ferromagnetic phase transition in nickel (Curie temperature). However, neither copper nor constantan have such a phase transition. Since the specific heat data for constantan exist only up to 700 K, the data were linearly extrapolated to 1300 K. This is justified for metals with no phase transition at temperatures above the Debye temperature, when the phonon specific heat is constant and the electronic specific heat has a linear dependence [21]. The Debye temperatures for copper and nickel are 343 K and 450 K, respectively [21]. The constantan specific heat data become linear above 450 K, thus indicating that its Debye temperature is similar to nickel's.

The thermal conductivity of copper and constantan are plotted in Fig. 3.11. Thermal diffusivity, D , was calculated from the relation

$$D = \frac{K}{\rho C_p} \quad (3.5.1)$$

where ρ is the density. Using the thermal conductivity and diffusivity data, β of eq 3.3.2 was calculated at different temperatures. The value

of β varied from 4 to 2 over the 300-1300 K temperature range for copper and constantan. Finally, the homogeneous junction temperatures were calculated using eq. 3.3.1 from the calculated homogeneous temperatures of the copper and constantan powders.

3.6 Results and Discussion

Table 3.1 contains the results from the copper-constantan powder thermocouple experiments. As indicated earlier, the initial shock pressure and shock energy were calculated for each shot. Figure 3.12 shows a typical oscilloscope record of a temperature measurement. The trace is essentially free of noise and has the expected response. The scope trace begins when the projectile impacts with the buffer plate and measures zero voltage until the arrival of the shock front at the thermocouple interface. The sharp negative voltage drop is followed by a slower decay to a constant negative voltage which corresponds to the homogeneous temperature. The rise-time in Table 3.1 was defined as the time it takes for the signal to go from 10% to 90% of the peak voltage. The decay time was defined as the time required for the difference in peak voltage to the constant homogeneous temperature voltage to go from 100% to 37%. Finally, the voltages were converted into temperatures using the calibration curve of Fig. 3.5 and the pressure correction curve of Fig. 3.6.

The measured temperature rise-times are typically around 60 ns. Before we can deduce the shock rise-times from these results, we must consider the effect of the sweep time due to the tilt of the shock plane with respect to the planar thermocouple interface. This tilt mainly arises from the misalignment of the flyer face to the impact face of the copper buffer plate. Although the tilt at impact was not measured

during this set of experiments, data from previous work on the 20 mm gun can be used to estimate the effect of the tilt on the temperature rise-time.

The existing tilt data were normalized by following relation,

$$t_{\text{sweep}} = \frac{d \tan \theta_{\text{tilt}}}{V_f} \quad (3.6.1)$$

where t_{sweep} is the time required for a shock front to sweep across a surface of diameter d when struck by a flyer which has a velocity of V_f and a tilt of θ_{tilt} with respect to the impact face. The value of d used to normalize the data was 4.7 mm since that is the diameter of the effective thermocouple area in the experiments. The normalized tilt data are plotted in Fig. 3.13 with the measured temperature rise-times. It is clear from the figure that almost all of the temperature rise-time is probably due to the tilt. Thus from the present results, we can conservatively place an upper limit on the shock rise-time as one half of the measured temperature rise-time. For shot 800 this corresponds to a shock rise-time of less than 23 ns. Since the shock velocity for shot 800 was 1.63 km/s, the shock front must be less than 37 μm wide, which is comparable to the larger particle sizes of the copper and constantan powders.

The peak interfacial temperature measurements are not true peak temperatures because the interfacial temperatures are very inhomogeneous. Since the equivalent electrical circuit of the thermocouple interface is a continuum of voltage sources in parallel, in the limit of the perfect electrical shorting of the higher voltages by the lower voltages, one would measure the coolest temperature of the

interface region. However, in the limit of no shorting, one would measure the spatial average of the temperature distribution at the interface. Furthermore, since the initial decay of the voltage is comparable to the rise-time which is mainly due to the heating of the thermocouple junction at different times, the measured peak voltage is attenuated by the parts of the junction which were heated first and have had time to reach the cooler homogeneous temperature. Nonetheless, the existence of peak junction temperatures give qualitative support for the claim of inhomogeneous and surface preferential deposition of shock energy during the consolidation of metallic powders.

The shape and duration of the decay times depend on the thermal diffusivity and the geometry of the temperature distribution. An exact analysis of the decay time is not feasible because of: 1) complicated particle geometry and variation in particle sizes, 2) possible existence of melted regions, 3) weighted averaging of measured interface temperature, 4) the effect of rise-time due to tilt, and 5) the difference in thermal diffusivity of copper and constantan. However, the decay times are related to the spatial scale of the inhomogeneous temperature distribution. The largest spatial scale possible is the size of the powder particle. From dimensional analysis the decay time, t_h , should be proportional to

$$t_h = \delta a^2/D \quad (3.6.2)$$

where a is the spatial scale (i.e., the particle diameter) and D is the thermal diffusivity. The proportionality constant, δ , will depend upon the exact geometry of the temperature distribution.

In the idealized case of a spherical particle with radially symmetric temperature distribution and no heat flow through its surface, the temperature evolution at the radial surface is given by [17]

$$T(r = a, t) = \bar{T} + \frac{2}{a^2} \sum_{n=1}^{\infty} W_n e^{-K\alpha_n^2 t} \quad (3.6.3)$$

where

$$\bar{T} = \frac{3}{a^3} \int_0^a r^2 f(r) dr,$$

$$W_n = \frac{a^2 \alpha_n^2 + 1}{a^2 \alpha_n^2} \sin a\alpha_n \int_0^a r f(r) \sin \alpha_n r dr,$$

and α_n are solutions of the transcendental equation

$$a\alpha_n \cot a\alpha_n = 1. \quad (3.6.4)$$

The function $f(r)$ is the initial temperature distribution. Thus the coefficients W_n depend on the exact nature of $f(r)$. The first 5 roots of eq. 3.6.4 are $a\alpha = 4.49, 7.92, 10.1, 14.0,$ and 17.2 . The slowest possible decay time is when $a\alpha = 4.49$ mode dominates. This corresponds to a δ of 0.013. It may be possible to have faster decay times depending on the initial temperature distribution. For $D = 0.84 \text{ cm}^2/\text{s}$ which is the value for copper at 900 K, the decay times are 0.25 to 0.75 μs with the particle size varying from 40 to 70 μm . Thus the measured decay times given in Table 3.1 are reasonably consistent with the rough approximate times expected from the idealized argument.

The dependence of the measured homogeneous copper-constantan

junction temperatures on the shock energy is plotted in Fig. 3.14. In addition the calculated homogeneous temperature of the copper powder and the thermocouple junction are included in the figure. The experimental data agree remarkably well with the calculated values over a wide range in shock energy and in temperature. Although the measured junction temperature is consistently about 6% higher than the calculated junction temperature, the differences are within the uncertainty caused by the approximations and accuracy of the data used in the calculations.

In fact, the slightly lower calculated temperatures may be explained by the following argument. The specific heat required in eq. 2.5.5 is for constant volume, C_v , while the existing data are for constant pressure. The difference between the two specific heats is given by [22]

$$C_p - C_v = \frac{VT\chi^2}{\eta_T} \quad (3.6.5)$$

where χ is the thermal expansion coefficient and η_T is the isothermal compressibility of the solid. V and T are specific volume and temperature, respectively. In solids the differences between the two are small. For example, in copper $\eta_T = 0.73 \times 10^{-11} \text{ m}^2/\text{N}$, $\chi = 5.5 \times 10^{-5}/\text{K}$, and $V = 1.12 \times 10^{-4} \text{ m}^3/\text{kg}$ at 600 K, thus $C_p - C_v = 27 \text{ J/kg/K}$ while $C_p = 410 \text{ J/kg/K}$ at 600 K. Therefore, the difference between C_p and C_v is less than seven percent, which would cause the underestimation of the temperature when C_p is used instead of C_v .

The accuracy of the shock pressure and energy calculations depend on the accuracy of the Hugoniot. Although the Hugoniot were based on reliable published data [23], the copper powder Hugoniot was tested,

nevertheless, by calculating the shock transit time from impact of the flyer to arrival at the thermocouple interface from the assumed Hugoniot and checked with the experimentally measured transit time. Table 3.2 contains these results. The calculated shock pressure, shock velocity, and transit times through both the copper buffer plate and the copper powder are given as well as the measured total transit times. The measured transit time was defined as the time from the beginning of the scope trace to the half maximum point of the negative voltage deflection minus 40 ns which is the displayed pretrigger time for the Tecktronix 485 oscilloscope. Before we can compare transit times, a potential source of error in the measured transit times must be taken into account. Only one wire was used for triggering the scope on impact; thus the measured transit times have an uncertainty due to the tilt of the flyer with respect to the impacted face. The average tilt in a 20 mm gun flyer is about 1.3 degrees. Thus, for a 15.8 mm diameter flyer with an impact velocity of 1.03 km/s, it takes about $0.35 \mu\text{s}$ (using eq. 3.3) for the closure of the flyer and impact face. Therefore, in the worst case of tilt, the trigger wire could break up $0.35/2 = 0.17 \mu\text{s}$ earlier than in the absence of tilt. This potential error, which can only increase the measured transit time, is given in the last column of Table 3.2 below the transit times. The comparison of the predicted transit times with the measured times show good agreement when the tilt error is taken into account. This gives us confidence in the interpretation of our results and on the accuracy of the published Hugoniots.

3.7 Summary

In this chapter we measured the homogeneous temperature rise of

shocked copper powder using the powder itself as a thermocouple. The measured temperatures agreed very well with the temperatures calculated from eq. 2.5.5 which gave the amount of irreversible energy deposited by a shock wave traveling through a powder medium (see Fig. 3.14). These measurements support all the assumptions usually made in dealing with shocked powders: 1) the deformation front in a metallic powder medium is indeed a true steady state one dimensional shock front, 2) most of the internal energy gain is thermal, and 3) total densification has occurred after the passage of the first shock wave.

The shock front was determined to be less than $37 \mu\text{m}$ wide. Thus the powder particle deformation and void elimination occurs as the shock wave traverses a powder particle.

Table 3.1. Results of the powder copper-constantan thermocouple experiments.

Shot #	Flyer Material	Calculated				Temperature Rise-Time (ns)	Time (μs)	Junction Temperature	
		Flyer Velocity (mm/μs)	P ₁ (GPa)	ΔE (kJ/kg)	Peak (C)			Homogeneous (C)	
798	2024 Al	1.03 ± .05	3.5 ± .2	135 ± 9	81 ± 13	0.22 ± .03	612 ± 40	397 ± 30	
800	2024 Al	1.39	6.0	232	45 ± 12	0.20 ± .02	857 ± 17	622 ± 20	
801	Lexan	1.49	1.3	50	67 ± 13	0.14 ± .03	202 ± 8	152 ± 8	
802	Copper	1.13	9.4	363	63 ± 31	0.63 ± .06	> 1150	942 ± 50	

Table 3.2. Comparison of predicted shock transit times with the measured transit times.

Shot #	Copper Buffer Plate (3.18 ± .03 mm thick)				Copper Powder (0.775 ± 0.025 mm thick)				Total Transit Time (μs)	
	Shock Pressure (GPa)	Shock Velocity (mm/μs)	Shock Transit Time (μs)	Shock Pressure (GPa)	Shock Velocity (mm/μs)	Shock Transit Time (μs)	Predicted	Measured		
798	12.8 ± .6	4.48 ± .22	0.71 ± .05	3.5 ± .2	1.23 ± .06	0.63 ± .04	1.34 ± .06	1.47 ± .17		
800	18.0	4.69	0.68	6.0	1.63	0.48	1.16 ± .05	1.26 ± .12		
801	7.0	4.24	0.75	1.3	0.75	1.03	1.78 ± .08	1.71 ± .14		
802	24.5	4.86	0.65	9.4	2.03	0.38	1.03 ± .05	1.12 ± .15		

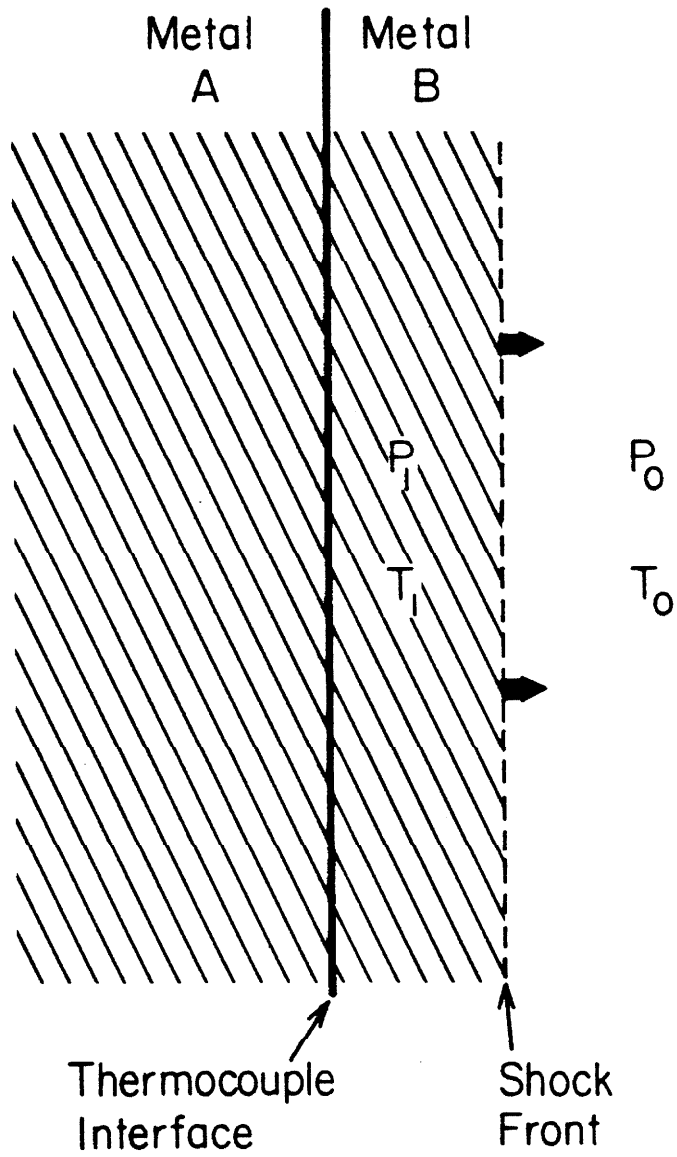
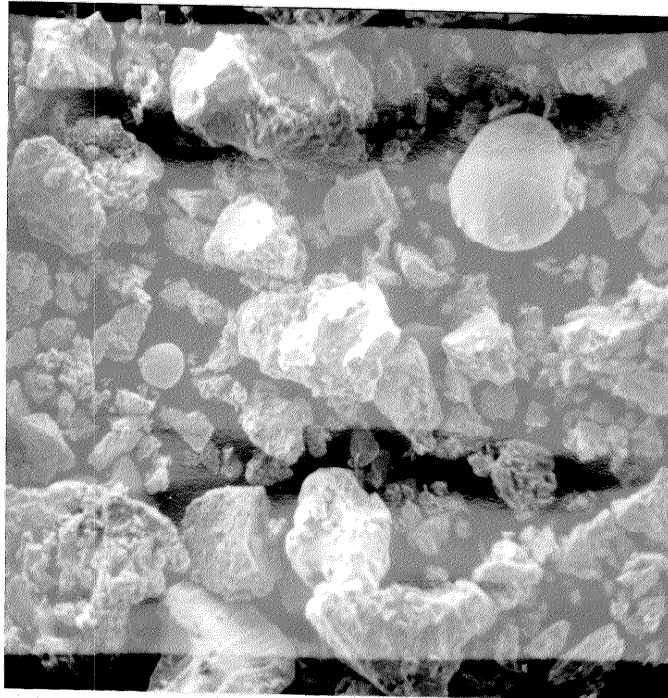


Fig. 3.1 Schematic representation of the idea for measuring shock temperatures with the shocked media generating the thermoelectric signals at the interface between two metals.



—
20 μm

Fig. 3.2 SEM photomicrograph of -100 mesh copper powder used in the experiments.

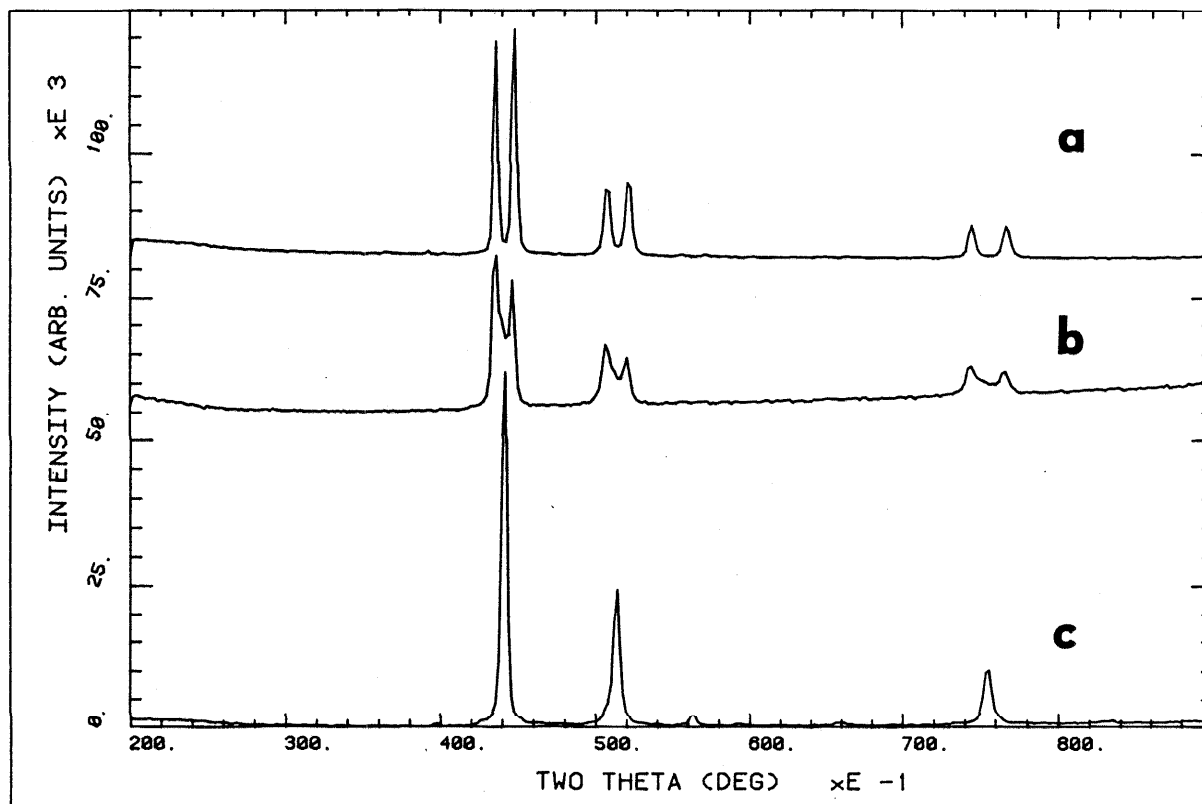
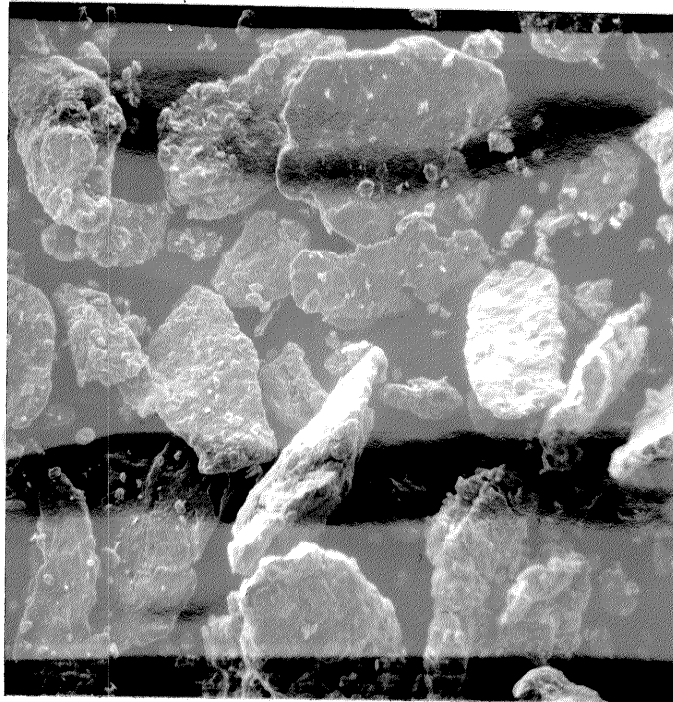


Fig. 3.3 X-ray diffraction intensity lines of a mixture of 55% copper and 45% nickel powders at different stages of mechanical alloying: (a) after mechanical alloying for 10 min.; (b) after 3.5 hrs.; (c) after 5 hrs. and thermal anneal in purified hydrogen atmosphere at 750 C for 16 hrs. Powder (c) was used in the thermocouple experiments.



—
20 μm

Fig. 3.4 SEM photomicrograph of constantan powder used in experiments. Note the flat shape obtained from the ball milling fabrication procedure.

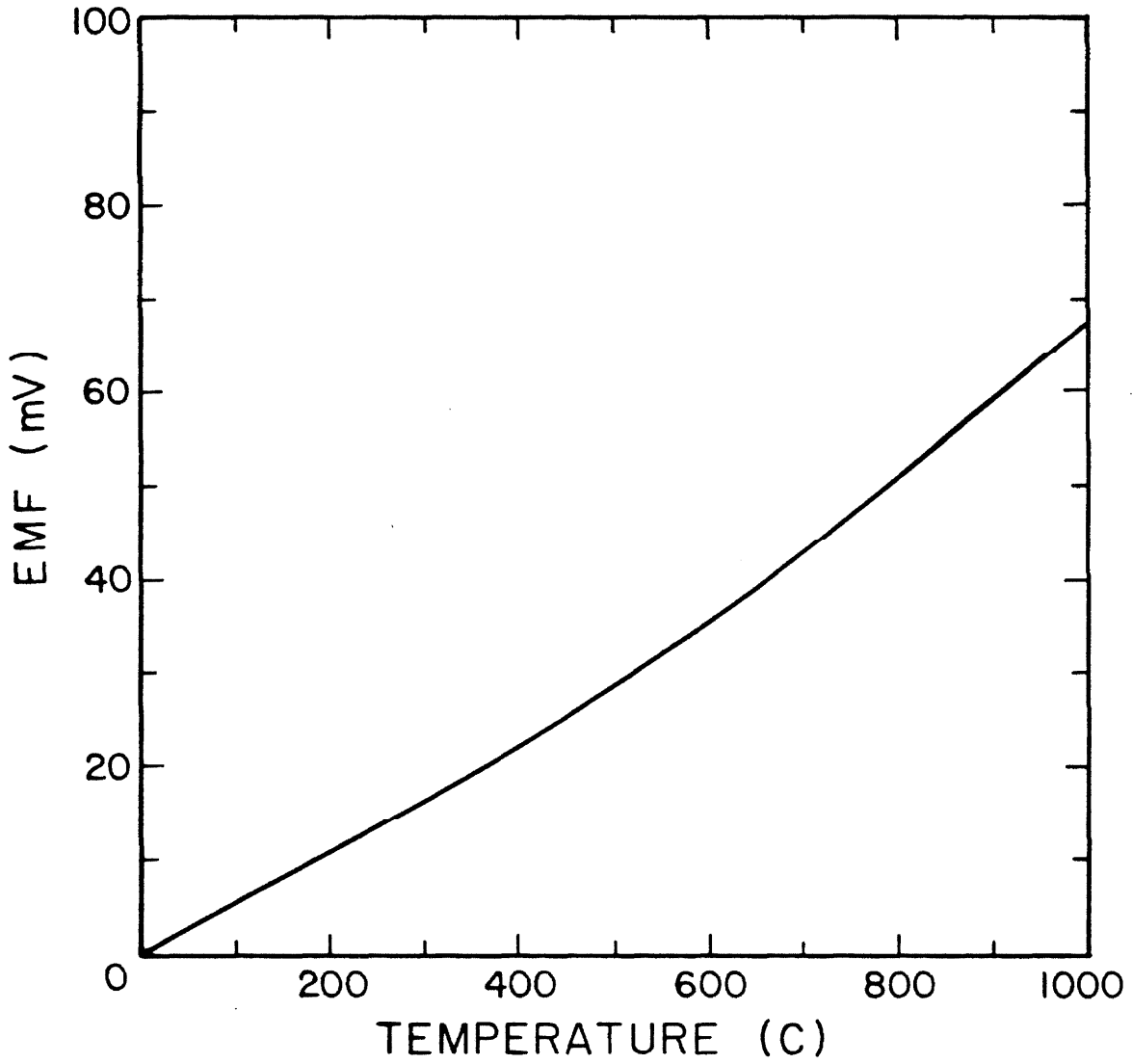


Fig. 3.5 Thermoelectric voltage of the copper-constantan powder junction as a function of temperature with the constantan as the reference ground [20].

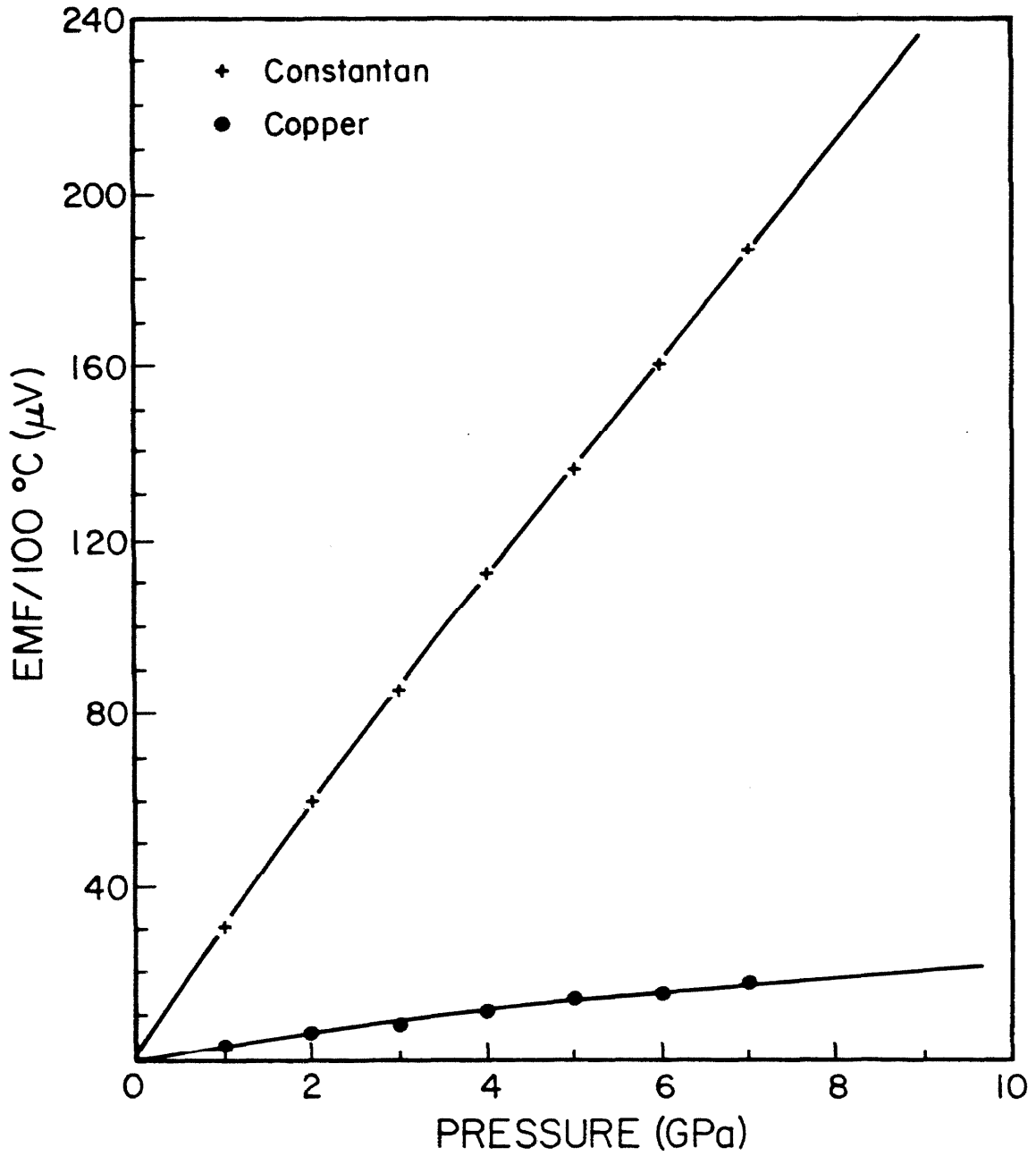


Fig. 3.6 The change in thermoelectric voltage (per 100 C) as a function of pressure [18].

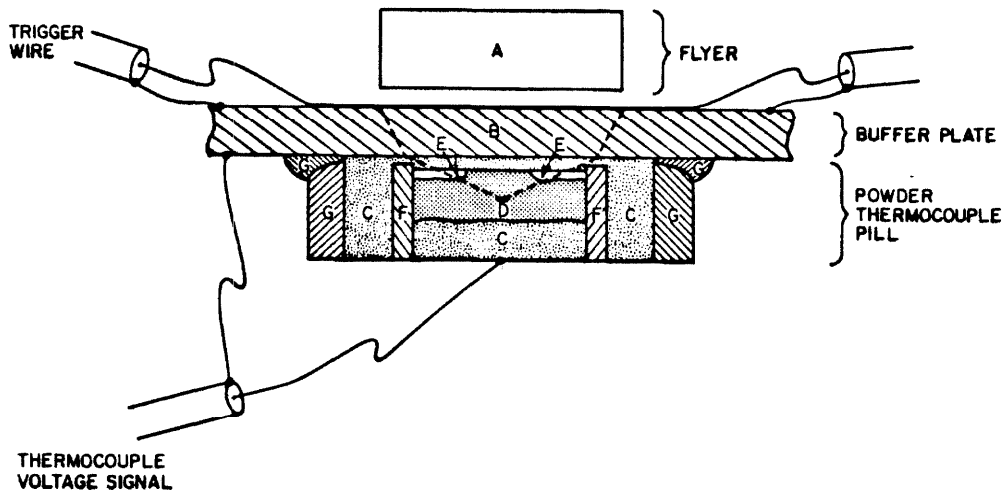


Fig. 3.7 Schematic cross-sectional view of the powder thermocouple assembly. The dimensions of the real assembly are: A) 5.08 mm thick X 15.88 mm diameter flyer, B) 3.18 mm thick copper buffer plate, C) copper powder, 0.78 mm thick at center, D) constantan powder, 4 mm thick at center, E) 0.5 mm thick alumina powder, F) 6mm long quartz tube with 11.7 mm I.D. and 14.0 mm O.D., and G) epoxy coating. The diameter of the powder pill was 2 cm. The diameter of the copper-constantan interface was 4.7 mm.

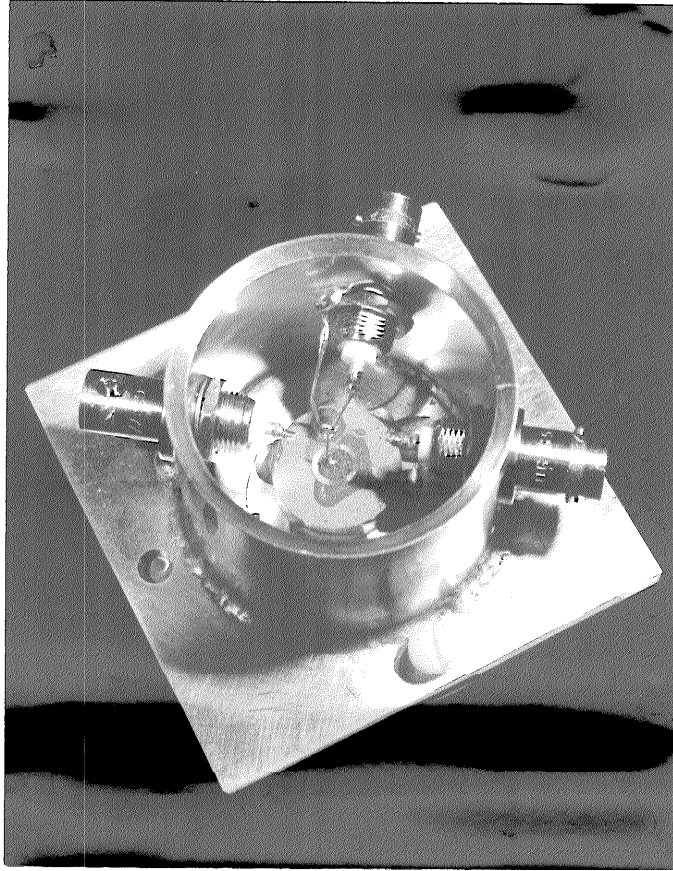


Fig. 3.8 Photograph of experimental assembly prior to loading onto the 20 mm gun barrel. The vacuum chamber was 5 cm wide and 3.8 cm long. The 7.6 cm X 7.6 cm copper buffer plate was 3.18 mm thick.

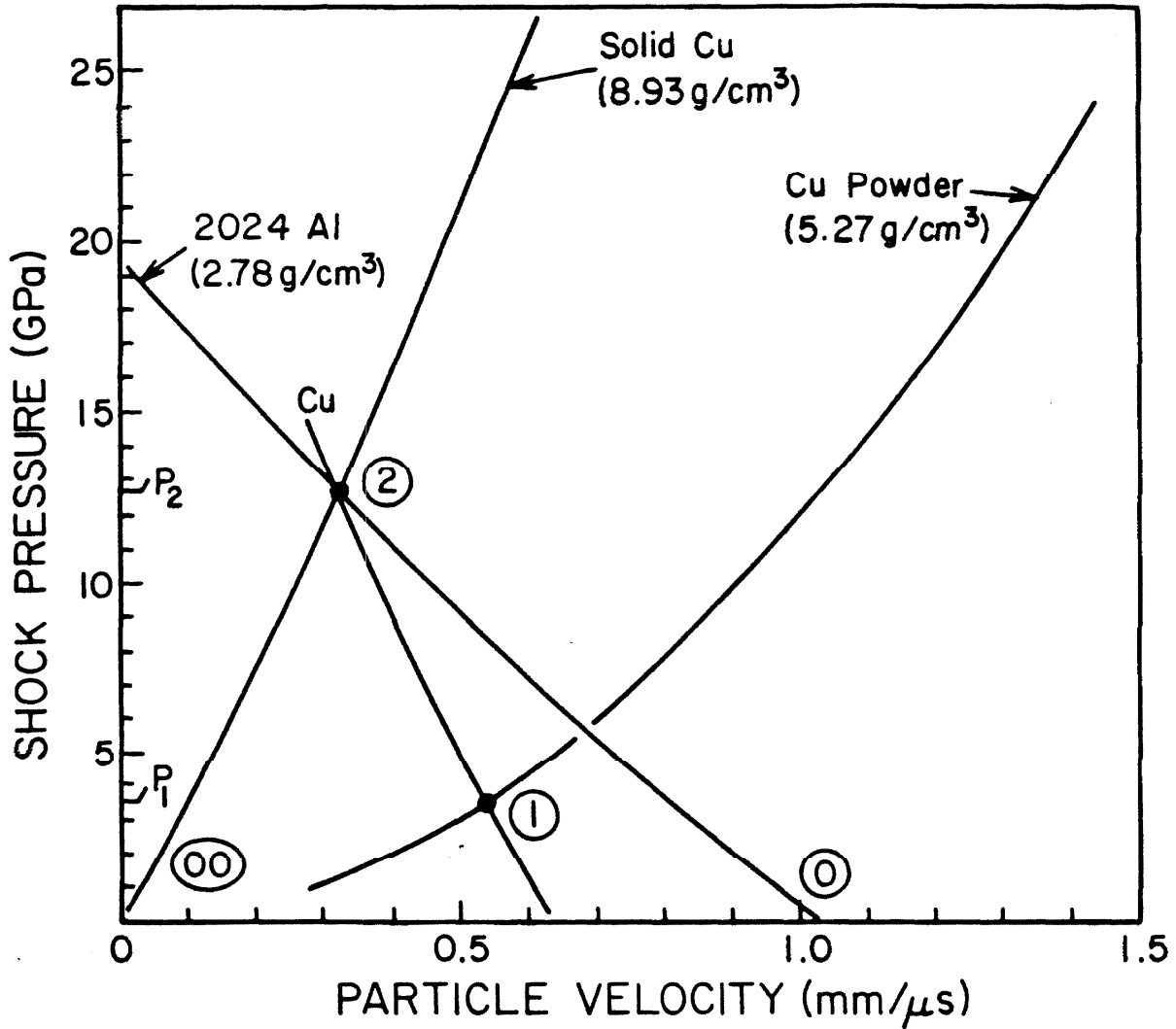


Fig 3.9 Shock impedance matching solution for the impact of 1.03 km/s aluminum flyer on a copper buffer plate and the subsequent shocking of the copper powder by the buffer plate. Hugoniot data for the copper powder from Ref. [23] was fit by the analytical equation for porous media from Ref. [24]. Hugoniot for solid copper and aluminum are from Ref. [25].

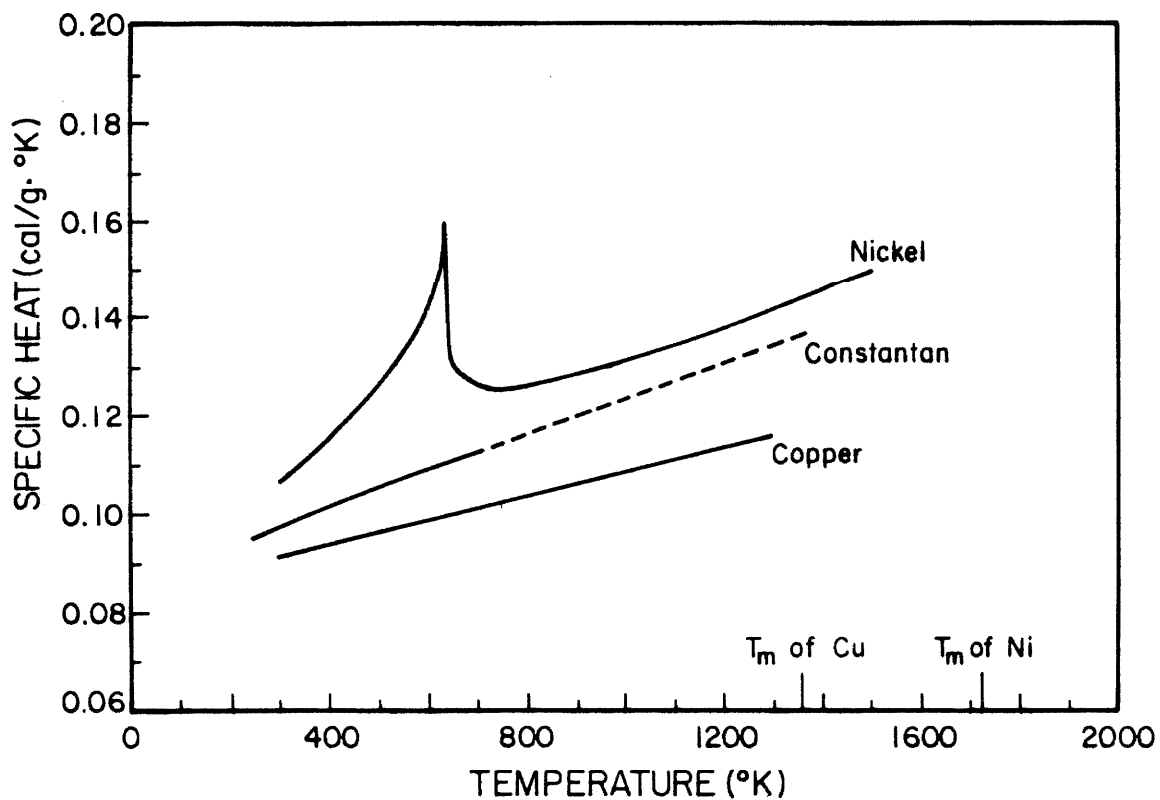


Fig. 3.10 The specific heat at constant pressure of nickel, constantan, and copper [26].

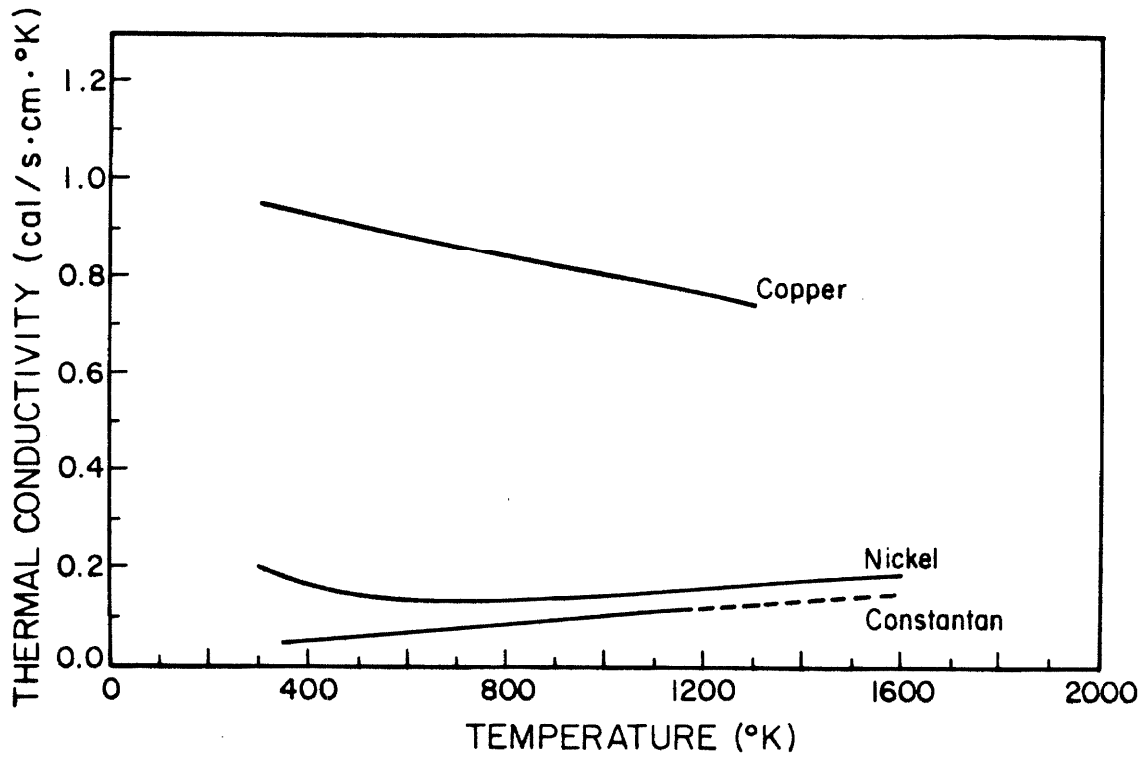


Fig. 3.11 Thermal conductivity data of copper, nickel, and constantan [26].

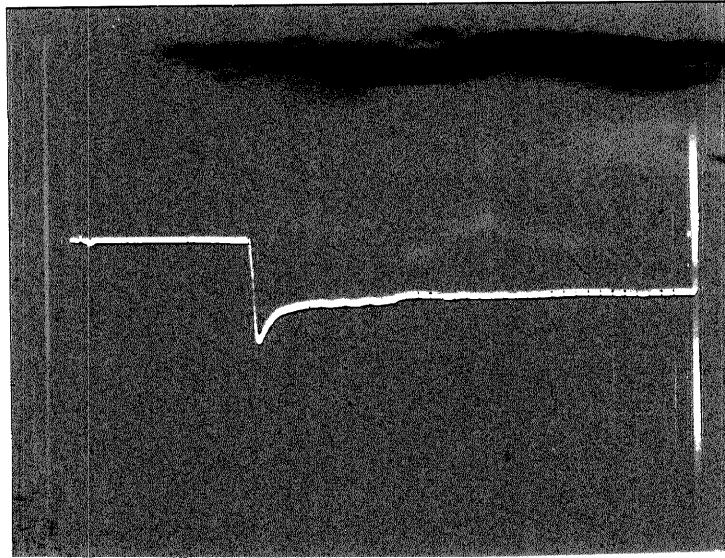


Fig. 3.12 Oscilloscope trace of the thermocouple signal from shot # 798.

Vertical scale: 20 mv/div. Sweep rate: 0.5 μ s/div.

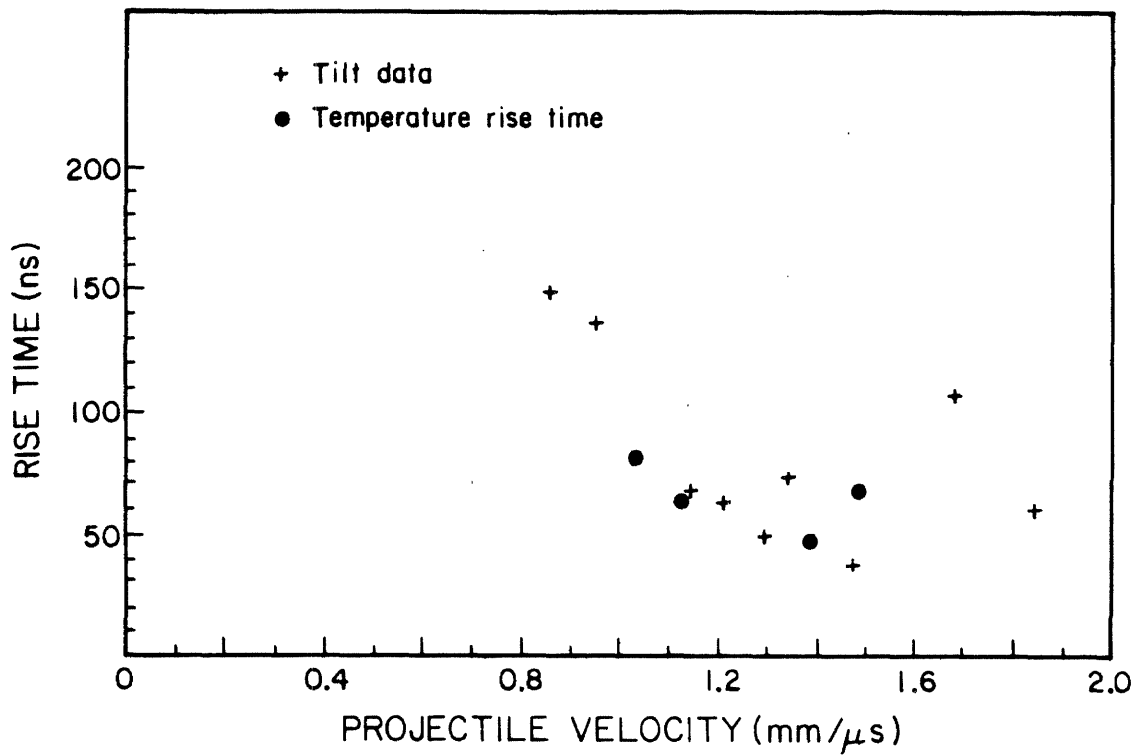


Fig. 3.13 Shock sweep times across a 4.7 mm diameter area due to measured tilt in flyer face for different velocities on the Caltech 20 mm gun.

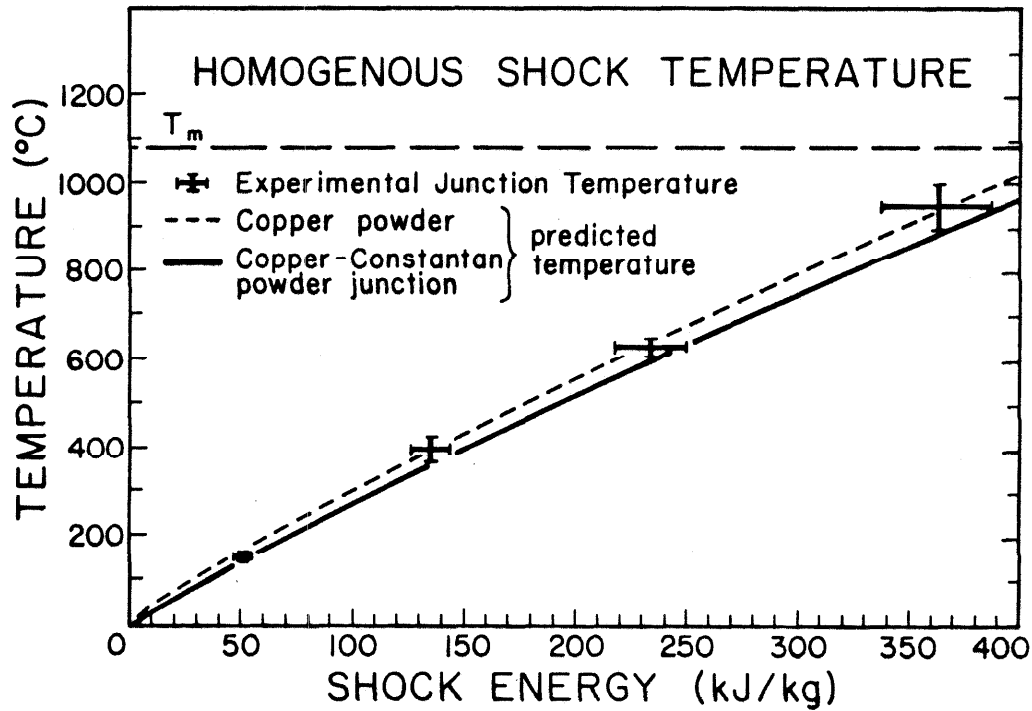


Fig. 3.14 The measurements of the homogeneous junction temperature plotted as a function of shock energy. The solid line is the calculated junction temperature and the dashed line is the calculated copper temperature. The calculated homogeneous temperature of the constantan is not shown on the figure, but lies about 10% lower than the copper temperature curve.

CHAPTER 3 REFERENCES

1. Kormer, S. B., M. V. Sinitsyn, G. A. Kirillov, and V. D. Urlin, Sov. Phys. JETP, 21, 689 (1965).
2. Kormer, S. B., Sov. Phys. JETP, 11, 229 (1968).
3. Utriw, P. A. and R. Grover, J. Appl. Phys., 45, 140 (1974).
4. Grover, R. and P. A. Utriw, J. Appl. Phys., 45, 146 (1974).
5. Lyzenza, G. A., PhD Thesis, Caltech, Pasadena, California, 1980.
6. Raikes, S. A., PhD Thesis, Caltech, Pasadena, California, 1978.
7. Dremine, A. N., B. P. Ivanov, and A. N. Mikhailov, Comb. Explos. Shock Waves, 9, 784 (1975).
8. Rosenberg, Z. and Y. Parton, J. Appl. Phys., 52, 6133 (1981).
9. Bloomquist, D. D. and S. A. Sheffield, Appl. Phys. Lett., 38, 185 (1981).
10. Keeler, R. N., in Proc. of the Int. Sch. of Phys. Enrico Fermi, Course XLVIII, Phys. of High Energy Density, Academic Press, New York, 1971.
11. Bloomquist, D. D., G. E. Duvall, and J. J. Dick, J. Appl. Phys., 30, 4838 (1979).
12. Nesterenko, V. F., Comb. Explos. Shock Waves, 11, 376 (1975).
13. Bloomquist, D. D. and S. A. Sheffield, J. Appl. Phys., 51, 5260 (1980).
14. Bloomquist, D. D. and S. A. Sheffield, J. Appl. Phys., 53, 5966 (1982).
15. Bloomquist, D. D., G. E. Duvall, and J. J. Dick, Washington State University Report F49620-77-C-0034, 1978.
16. Imaoka, K., K. Kondo, and A. Sawaoka, Jpn. J. Appl. Phys., 19, 1011 (1980).
17. Carslaw, H. S. and J. C. Jaeger, Conduction of Heat in Solids, Oxford University Press, New York, 1947.
18. Blatt, F. J., P. A. Schroeder, C. L. Foiles, and D. Greig, Thermoelectric Power of Metals, Plenum Press, New York, 1976.
19. Schwarz, R. B., private communication.

20. Bartels, J., P. T. Bruggencate, H. Hausen, K. H. Hellwege, K. L. Schafer, and E. Schmidt, ed., Landolt-Bornstein: Zahlenwerte und Funktionen aus Physik, Chemie, Astronomie, Geophysik, und Technik, 6th Ed., Vol. IV, Part 3, Spring-Verlag, Berlin, 1957.
21. Kittel, C., Introduction to Solid State Physics, 5th Ed., John Wiley and Sons, New York, 1976.
22. Pippard, A. B., The Elements of Classical Thermodynamics, Cambridge University Press, New York, 1964.
23. Boade, R. R., J. Appl. Phys., 39, 5693 (1968).
24. Simons, G. A. and H. H. Legner, J. Appl. Phys., 53, 934 (1982).
25. McQueen, R. G., S. P. Marsh, J. W. Taylor, J. N. Fritz, and W. J. Carter, in High-Velocity Impact Phenomena, R. Kinslow, ed., Academic Press, New York, 1970.
26. Touloukian, Y. S., ed., Thermophysical Properties of High Temperature Solid Materials, Vols. 1-6, The MacMillan Company, New York, 1967.

CHAPTER 4

SHOCK CONSOLIDATION AND RECOVERY EXPERIMENTS

4.1 Introduction

A powerful yet simple technique for studying shock wave consolidation of powders is to examine recovered samples which have been subjected to well-defined shock wave conditions. For example, metallographic observations can be used to study the deformation and interparticle bonding of the powder particles. Powder characteristics such as shape and size distribution were held constant and only the influences of the shock pressure and duration on the shock consolidation process were studied in the present investigation, although some preliminary results on the importance of surface oxides on the powder particles are also presented. In this chapter, results from the recovery experiments on steel, molybdenum, and glass forming nickel alloy powders are presented and discussed.

The experimental methods used to recover samples in shock wave experiments are described in section 4.2. The steel powder was used to study the effects of shock energy and shock duration which are presented in section 4.3 and 4.4, respectively. In section 4.5 the adverse effect of surface oxides on molybdenum powder is demonstrated. A glass forming nickel-molybdenum alloy powder was used to study the interparticle melting produced in shock wave consolidation experiments. These results are presented in section 4.6. The results presented in the chapter are briefly summarized in section 4.7.

4.2 Experimental Method

In order to shock compact powder samples of well-defined initial density and shape, cylindrical powder charges were statically compressed inside the shock recovery assemblies into discs. Typically these discs were 15.2 mm in diameter and 1.3 mm in thickness. The powders used in the various recovery experiments are listed in Table 4.1. Figure 4.1 shows a schematic cross section of a shock recovery assembly. The powder is contained inside a steel washer and sandwiched between a 76 μm thick copper cover and a steel base. It was found that this arrangement facilitates the recovery and easy removal of compacted samples. Fly-away momentum traps (labeled axial spall plate in Fig. 4.1) were used to absorb much of the shock energy after its passage through the powder [1].

The 20 mm bore propellant gun from the Caltech Seismology Laboratory was used to launch disc-shaped flyer plates, 14.8 mm in diameter to speeds of 0.89 to 1.72 km/s for most of the work reported here. The 40 mm bore gun from the Seimology Laboratory was used for the shock duration experiment described in section 4.4. Most flyers were made from 304 stainless steel. Flyers made of 2024 Al and of Lexan were also used to obtain lower shock pressures. The flyer velocity before impact was measured to 2 percent accuracy by timing the interruption of two laser beams set 57.8 mm apart in the path of the projectile. Prior to shock consolidation, the gun and recovery assemblies were evacuated to 20 mTorr.

The initial shock pressure through the porous sample, and the subsequent shock history achieved via reflection from the supporting base, were calculated by the impedance match method, as described in

Chapter 2, section 2.6. In some cases the shock Hugoniot of the powder were determined by experimentally measuring the shock velocity and fitting the result to the analytical expression for the Hugoniot of a porous medium derived in section 2.4 of Chapter 2.

In order to correlate the mechanical properties of the compacts with the shock pressures, it was desired that the consolidation be as homogeneous and one-dimensional as possible. To achieve this, typical aspect ratios (diameter/thickness) of 12 were used. Unavoidable edge effects become important in the central region of the compact when waves arrive from these edges before complete consolidation has occurred. The compacts produced were large enough so that several small tensile test specimens could be made from the central region of the recovered discs.

The duration of the compressive shock state is proportional to the flyer thickness. Most of our flyers were 5.1 mm thick, giving a flyer-to-sample thickness ratio of 4. The typical shocked state in the central portion of the samples lasted from 2.7 μ s (at the front surface) to 2.1 μ s (at the back surface). Furthermore, the maximum shock pressure attained was the same throughout this central portion.

The recovered samples were sectioned for density measurements, metallographic examination, diamond pyramid hardness (DPH) measurements, and the preparation of tensile test samples. The etchants used in the metallographic examinations are listed in Appendix B. The density of the compact was determined from weight measurements in air and toluene. The sections for tensile test samples were mechanically polished to a thickness of about 1/4 mm using wet SiC paper and diamond paste through 1 μ m grit. Dog-bone shaped tensile samples, with a gauge section 2 mm long and 0.7 mm wide were spark machined from the polished sections.

These were pulled to failure in an Instron Universal Testing Machine at a strain rate of approximately 4×10^{-3} /sec utilizing a tensile system designed to minimize sample bending. Further details on the tensile tests are presented in Appendix C. Because shock compaction deforms the powder particles anisotropically, the UTS may also be anisotropic. However, in the present study the tensile axes of the samples studied were parallel to the impact face. The fracture surfaces of the tensile specimens were then examined by scanning electron microscopy.

4.3 Shock Energy

Rapidly solidified powders (RSP) of AISI 9310 alloy, which passed through 200 mesh (74 μm) but were retained in 325 mesh (44 μm) screens, were used for the shock energy dependence study. These iron-based powders were provided by United Technology Research center and had 3.2 Ni, 1.39 Cr, 0.65 Mn, 0.24 Mo, and 0.10 C percent by weight [2]. The powders were produced by a centrifugal atomization process and were mostly spherical, as shown in Fig. 4.2. Optical and x-ray metallography studies [2] revealed that individual particles have little variation in microstructure and composition. The major constituent phase was bcc with a lattice constant of 2.86 \AA . A small amount of fcc structure, with a lattice constant of 3.58 \AA , was also detected. The diamond pyramid hardness of the individual particles was 344 ± 34 which is comparable to the hardness of wrought AISI 9310 [3]. Table 4.2 contains some of the properties of the wrought AISI 9310 steel. The powders were stored at ambient conditions and no attempt was made to remove surface oxides prior to shock consolidation.

Table 4.3 is a summary of the data from the present investigation. The powders had a nominal size between 44 and 74 μm . However, as seen

in Fig. 4.2, the powder also contains particles smaller than the lower value quoted. These are attached to the larger particles, presumably during the centrifugal atomization process.

The shock pressures, energies, and velocities were calculated as explained in Chapter 2. The analytical expression for the porous Hugoniot was fit to the shock wave data for iron powder [4] and is shown in Fig. 4.3. The values of γ , η_s , and V_0 are 1.69, 0.006 GPa^{-1} , and $1.22 \times 10^{-4} \text{ m}^3/\text{kg}$, respectively [5]. This analytical expression (eq. 2.4.11) was then used to describe the properties of our AISI 9310 steel powder. The use of the Hugoniot for iron to describe that of iron-based alloys is supported by 1) the observation that the Hugoniot of solid iron and stainless steel are very similar in the pressure range of our experiments, and 2) a few direct Hugoniot measurements made on porous AISI 9310 samples.

The final densities of samples 754, 733, and 734 were 7.86 ± 0.28 , 7.84 ± 0.08 , and $7.86 \pm 0.09 \text{ g/cm}^3$, respectively. Therefore, within the uncertainty of the density measurements, these samples reached the bulk alloy density of 7.90 g/cm^3 . Since porous iron behaves as a solid after the passage of shock waves above 2.6 GPa [4] and our lowest shock pressure was 3.6 GPa, we can assume that nearly full density was achieved for all shock conditions used in the present study. This conclusion was further corroborated by the metallographic observations which revealed void-free surfaces on all of our compacts.

Photomicrographs of etched sections of consolidated samples, cut parallel to the impact face, are shown in Fig. 4.4. In our consolidations of AISI 9310 RSP, the regions which presumably melted are not delineated by the etchant. Thus we were not able to estimate the

amount of melt from the photomicrographs as had been done previously in studies of tool steel powders [6,7]. However, the figure provides what can be interpreted as indirect evidence of interparticle melting. Figure 4.4 (a) shows a sample consolidated by a shock energy of 240 kJ/kg where the boundaries between individual particles are easily discernible by the preferential etching. In the 500 kJ/kg consolidation shown in Fig. 4.4 (b), most of the particle boundaries are difficult to resolve. Figure 4.4 (c) shows the sample consolidated at the shock energy of 730 kJ/kg. Here no particle boundaries are resolved. We attribute the preferential etching which reveals particle boundaries to oxides and other impurities on the particle surfaces. The disappearance of this preferential etching indicates that the oxides are more thoroughly broken and mixed with increasing pressure and shock energy input. Breakup of the oxide films on the particle surfaces appears to be a requisite for strong interparticle bonding.

SEM scans of the fractured surfaces of three tensile test specimens are shown in Fig. 4.5. This series of scans show that, as the shock energy is increased, the nature of the fracture changes from predominantly interparticle to intraparticle. At the lowest shock energy (Fig. 4.5 (a)) the fracture surface shows mostly particle-like protrusions which disappear progressively at higher energies (Fig. 4.5 (b) and (c)). At the highest shock energy the fracture is much smoother although some particle boundaries are still discernible. Figure 4.5 (c) also shows a crack, oriented nearly parallel to the tensile axis, which we believe existed before the tensile test.

Normal views of the same three fractured surfaces of Fig. 4.5 are shown in Fig. 4.6 at a higher magnification. These pictures indicate

that the area exhibiting ductile fracture increases with shock energy. The ductile bonding of the particles is almost nonexistent at 240 kJ/kg, while at 500 kJ/kg the ductile bonds are mostly at localized areas which resemble microscopic spot welds. Thus, at lower shock energies, shock waves tend to produce well-bonded surfaces only at localized spots around a particle where very large stresses and deformations occur. These spots are presumably areas of point-like contacts between particles and voids which are filled by high-rate deformation of neighboring particles. However, as the shock energy is increased, sufficient melt is produced to cover most of the interparticle surfaces as evidenced by the almost entirely ductile fracture surface of the 730 kJ/kg compaction (Fig. 4.6 (c)).

In order to obtain hardness values which minimize surface hardening effects due to the mechanical polishing, 500 g loads were used whenever possible. However, when small indentation sizes were required, the hardness was determined with 100 g loads. This load was used to measure the DPH of the powder itself and that of sample 754, where the 500 g load was observed to push out particles from the poorly bonded compact. In cases where both 500 g and 100 g loads were used, the former hardness readings were lower by 10 percent.

The 500 g indentations produce diagonals of approximately 43 μm and penetration depths of 6 μm . Since the particle sizes are in the 44-74 μm range, our measurements average out possible differences in hardness between particle interiors and boundaries, which have been noted by other investigators [6,7]. Nevertheless, our measurements give the average bulk hardness which allows us to estimate the intrinsic strength of the shocked material using the simple linear relationship between

hardness and UTS observed in wrought steel [8].

When the DPH values are considered as dimensionless numbers, the ratio of the UTS and DPH has a value of 3.3×10^{-3} GPa for wrought steel [8]. This constant was determined for the shock hardened AISI 9310 steel by using an AISI 9310 flyer plate in a 15 GPa shock consolidation experiment. The recovered flyer had a DPH of 405 ± 10 and a UTS of 1.16 GPa, which corresponds to a proportionality constant of 2.9×10^{-3} GPa. Therefore, for a given DPH, the UTS in the shocked AISI 9310 steel is 88 percent of that in wrought steel.

Figure 4.7 shows the DPH and UTS data as a function of shock energy. The ordinate scales for the DPH and UTS measurements were chosen so as to have the proportionality found by shocking the solid AISI 9310 steel. Although the DPH should also depend on the shock pressure, it is plotted against shock energy for the purpose of comparing the UTS expected from the DPH with the actual measured UTS. With the exception of the test at the lowest shock energy of 94 kJ/kg, the powder distension was 1.64. Thus the shock energy scales linearly with shock pressure, and there should be little distortion of the qualitative behavior of the DPH with shock energy.

The DPH shows a gradual increase with shock energy. The rate of increase is lower than that observed in other alloys [9]. This is explained by the fact that, in the RSP, the particles are already fairly hard due to the rapid solidification fabrication process. The increase in hardness of shock loaded metals can be attributed to increased dislocation density from work hardening and shock-induced microstructural refinements [10]. With increasing shock energy the DPH goes through a broad maximum around 500 kJ/kg before decreasing.

Nonetheless, the hardness at the highest energy consolidation of 770 kJ/kg is still slightly larger than the hardness of the initial powder.

The UTS of the compacts has a very strong dependence on shock energy. There is negligible strength in the compacts for consolidations at shock energies below 200 kJ/kg. Above this threshold in shock energy the compact strength increases rapidly, until a maximum strength of 1.4 GPa is reached at the 500 kJ/kg shock energy consolidation. Similar to the DPH, the UTS declines for the higher shock energy consolidations.

At the highest shock energies, the recovery of compacts free of cracks requires special attention. For example, a 1.3 mm thickness sample shocked to 730 kJ/kg shock energy yielded a particularly weak tensile specimen due to the existence of a crack in a plane nearly parallel to the tensile axis (see Fig. 4.5 (c)). Other parts of the recovered compact also showed cracks. However, using improved recovery techniques involving much thicker samples, a consolidation at 770 kJ/kg shock energy resulted in a crack-free sample. Therefore, the UTS of the 770 kJ/kg shock energy compact is considered a more reliable measurement.

The results in Fig. 4.7 show that, with increasing shock energy, the measured UTS of the compacts approach the UTS expected from the DPH, implying improvement in interparticle bonding. There are two distinct regions in the convergence of UTS and DPH measurements. For shock energies from 200 to 400 kJ/kg, the UTS rapidly approaches the DPH curve, implying a very rapid increase in the effectiveness of the interparticles bonds. For shock energies above 400 kJ/kg, the UTS and DPH curves converge much more slowly. The UTS is limited by the stress required to initiate and propagate a crack across the tensile specimen.

This propagation path, through weak and poorly bonded regions in the tensile specimen, is of a statistical nature. The UTS and DPH curves indicate that complete interparticle bonding is achieved at approximately 800 kJ/kg, where these curves merge together. However, at these high shock energies, the strength and hardness are already decreasing. This decrease is associated with the softening of the particles due to grain coarsening and/or dislocation recovery as the result of shock heating. The homogeneous temperature and the cooling rate are discussed in Chapter 5 when the consolidation map for AISI 9310 steel is presented.

The interplay of the increase in strength versus the decrease in desirable properties of the compact with increasing shock energy produces an optimum value of shock energy for a given powder. In the case of RSP of AISI 9310 alloy with 44-74 μm diameter particles, the increase in strength with shock energy is rapid enough to insure that most of the high hardness of RSP is retained. The shock consolidation process gives optimum results for the AISI 9310 powders for shock energies between 500 and 600 kJ/kg.

4.4 Shock Duration

The AISI 9310 iron alloy powder with the same specifications as those used in the experiments described in section 4.3 was also used in the study of the effect of shock duration on the strength of the compact. A cylindrical shaped powder sample of 35 mm diameter and 10.2 mm thickness with a distension $m = 1.67$ was shock compacted by a stainless steel flyer, 40 mm in diameter and 5.2 mm in thickness, accelerated to a velocity of 1.16 km/s. The initial shock pressure produced was 9.5 GPa and the shock energy was 404 kJ/kg. Figure 4.8

shows the position-time relation for the initial shock and release waves in the flyer and powder for this experiment. The approximations that are used in constructing the diagram are discussed in Section 2.6 of Chapter 2. The initial shock velocity through the powder is calculated to be 2.2 km/s, while the shock wave through the solid flyer and the subsequent release wave velocity is 4.8 km/s.

Because the densification of the powder occurs at the front of the first shock wave, following shocks should have little relevance in the consolidation. As can be seen in Fig. 4.8, the powder at the impact surface sustains the initial shock pressure for a time interval of 2.1 μ s. Points below the impact surface are subjected to a shorter initial shock pressure. The leading edges of the release waves catch up with initial shock at a depth of approximately 4 mm where a long crack parallel to the shock front was found in the recovered sample. Four slices, parallel to the shock front, were cut from the compact by spark erosion. From each of these, dog-bone shaped tensile specimens were cut, also by spark erosion. For each specimen, the duration t_d of the initial shock was calculated as

$$t_d = 2.1 y/y_0 (\mu\text{s}),$$

where y and y_0 are the distances from the specimen to the impact surface and from the crack to the impact surface, respectively. The value of y_0 was 3.8 mm.

The results of the above mentioned analysis are plotted as squares in Fig. 4.9 which shows the UTS of the specimens as a function of t_d . The circle is the result of tensile tests in compacts of the same powder, consolidated at the same value of shock pressure and energy, but

in the 20 mm bore gun (from section 4.3). The results indicate that the strength of the compact decreases as the shock duration decreases and that the shock duration must be longer than a critical value in order to produce well-bonded compacts. For the 404 kJ/kg shock energy consolidation, the shock duration must be greater than 0.7 μ s for strengths greater than half the maximum.

4.5 Surface Oxides

The molybdenum powder used to demonstrate the effect of surface oxides on the interparticle bonding is shown in Fig. 4.10. The Mo powder had a compositional purity of 99.8 % by weight. The values of γ , η_s , V_0 used in the Hugoniot of Mo powders are 1.70, 0.0025 GPa⁻¹, and 9.80×10^{-5} m³/kg. The value of η_s was calculated from equation 2.4.5 with $a_0 = 6.3$ km/s [11]. The value of γ was estimated by fitting the Hugoniot (equation 2.4.11) to molybdenum shock data [12].

Shock energies in the range of 185 to 894 kJ/kg failed to produce well-bonded compacts of the as-received Mo powder. To test the contention that the problem may be due to surface oxides, the powder was treated at 730 C by a flow of one atmosphere pressure of H₂ gas for 2 hours. Further details of the oxide reduction procedure are contained in Appendix D.

The treated powder was pressed into a target assembly under an Ar atmosphere. The initial powder density was 6.12 g/cm³ ($m = 1.67$). After a less than 1 minute exposure to air, the target assembly was loaded onto the 20 mm gun and evacuated to 40 μ m Hg pressure. A 17.8 GPa shock wave (580 kJ/kg) was used to consolidate the powder. The previous attempt at the same shock energy with the as-received powder resulted in recovery of Mo powder only. However, with the treated

powder the experiment resulted in the recovery of a well-bonded compact whose photomicrograph is shown in Fig. 4.11. The UTS of the consolidated sample was 0.76 GPa which is slightly larger than that of rolled sheet or bar stock [8]. Table 4.2 contains some of the properties of wrought molybdenum. Thus reduction of surface oxides can improve the strength of the compact enormously and is an important procedure for successful shock consolidation.

4.6 Interparticle Melting

In glass forming metals, the amorphous phase usually has a different rate of chemical etching than the microcrystalline phase of the same metal. Thus the amorphous phase can be delineated from the microcrystalline phase in a mixed phase material by simple metallography. If the melted regions are quenched rapidly enough to form the amorphous phase during shock consolidation, glass forming metal powders can be used to study the melting produced by shock waves.

Amorphous Markomet 1064 powders can be shock consolidated to produce entirely amorphous compacts for shock energies of less than 400 kJ/kg [13,14]. Thus for shock consolidations of energies less than 400 kJ/kg, the melted regions of Markomet 1064 powders are solidified quick enough to produce the amorphous phase. Therefore, microcrystalline Markomet 1064 powders can be used to study the shock induced melting in powder consolidations.

Irregularly shaped flakes of Markomet 1064 ($\text{Ni}_{52.5}\text{Mo}_{38}\text{Cr}_8\text{B}_{1.5}$, by weight percentage) amorphous alloy prepared from approximately 25 μm thick melt spun ribbons are shown in Fig. 4.12. Markomet 1064 is a glass forming alloy with a density of 8.96 g/cm^3 , whose amorphous phase crystallizes at 600 C. The shock Hugoniot for Markomet 1064 has been

measured for a distension of $m = 2.0$ and is shown in Fig. 4.13 [13].

The amorphous powder was annealed at 900 C for 2 hours in an atmosphere of helium. X-ray diffraction analyses performed on a standard Norelco diffractometer with a Cu tube verified the transformation from the amorphous phase to the crystalline phase in the annealed powder. Photomicrographs of the etched amorphous and microcrystalline powders are shown in Fig. 4.14. The amorphous powders retained the smooth polish and are still white, while the annealed powders are darkened from the etching of the microcrystals.

The microcrystalline powders were shock consolidated to full density from an initial density of 4.48 g/cm^3 ($m = 2.0$). The recovered samples were sectioned, polished, and etched in the planes parallel and perpendicular to the shock front. The area percentage of the amorphous phase was measured by random area samplings of the photomicrograph.

The results of the present investigation are given in Table 4.4. Photomicrographs of the samples are shown in Figs. 4.15, 4.16, and 4.17. The lowest shock energy consolidation of 190 kJ/kg has little or no melt between the particles while the higher shock energy consolidations have extensive interparticle melting. With increasing shock energy, the amount of interparticle bonding increases as more and more of the interparticle surfaces are covered by melted material.

In the 350 kJ/kg consolidation, most of the particles as seen in the shock plane are surrounded by melted regions (see Fig. 4.18). However, the coverage of the melted material around the particle is not isotropic, as can be seen clearly in Fig. 4.17 (b) where the plate-like particles of Markomet 1064 deform heavily in clusters of particles. In

other words, several particles tend to stack up on top of each other with little or no interparticle melting between them, while there are extensive melt regions surrounding these clusters. This clustering depends on the particles' shape and size distribution and on how the powder particles were initially packed before consolidation.

The melt regions can be grouped into two general categories: 1) thin-long interparticle layers or 2) larger irregularly shaped melt pools. This is seen clearly in Fig. 4.17. The thin interparticle melt layers are to be expected either from the squeezing of the melt layers or from interparticle friction produced as the particles slide against each other. The existence of large melt pools has two possible explanations: 1) intense localized deformation and heating near large voids where the particles are squeezed into the voids or 2) the accumulation of melt in the large voids from melt produced elsewhere.

The melt pools observed in the plate-like Markomet 1064 powder contrasts with the results from the shock consolidation of spherical particles of tool steel where the material which transformed to martensite was distributed more uniformly around the powder particles [15,16]. This suggests that the melt distribution is highly material and particle shape dependent. In terms of shock energy, the melt pools are not efficient in bonding the particles together relative to the thin interparticle layers. Thus, for producing a well-bonded compact for a given amount of melt fraction, the initial void distribution should be as homogeneous as possible.

The area percentages and melt fraction data are presented in the last two columns of Table 4.4. The area percentage from only one micrograph is equal to the volume percentage of melt only if the melt

regions are randomly distributed such that any given plane always contains a random sampling of melt region cross sections. This seems to be the case in the two lower shock energy consolidations where there is no difference in the shock plane and perpendicular plane area percentages. However, the larger melt regions of the 350 kJ/kg shock energy consolidation are not totally random since the area percentage of the one micrograph in the shock plane is larger than that of the micrograph in the perpendicular plane. Thus, in order to get an accurate melt fraction, one must measure the area percentage in many randomly oriented planes and take the average. However, for the present investigation the average will consist of only two planes.

When discussing the melt fraction results, it is convenient to convert the shock energy of consolidation, E , into a dimensional parameter, L , which is an upper bound to the melt fraction for a given shock energy input. The concept of L was introduced in a model for the shock consolidation process in which the maximum amount of melt was calculated from energy balance [17]. L is defined as

$$L = E / [\bar{C}_p (T_m - T_0) + H_m] \quad (4.6.1)$$

where \bar{C}_p is the average specific heat of the solid between the initial temperature, T_0 , and the melting temperature, T_m , and H_m is the specific heat of fusion. We will neglect the effect of pressure on the melting temperature. In iron the melting point is raised by 11% at a pressure of 10 GPa which is a typical change for metals [18]. Thus, by neglecting the changes due to pressure, we will underestimate L by a similar percentage.

If all of the shock energy was deposited near the particle surface such that the molten material remained at the melting temperature, then L would be the melt fraction in that case. L defined in the above manner is convenient because: 1) it removes some of the material dependence and allows for the comparison of melt fraction data from different materials, and 2) the efficiency of the shock wave in depositing energy on the surface can now be readily seen from the comparison of the melt fraction to L .

Figure 4.19 contains the melt fraction data from the shock consolidation of powders of Markomet 1064 and an aluminum alloy. The aluminum alloy results were obtained from Ref. [16]. Table 4.5 contains the thermodynamic data used to calculate L from eq. 4.6.1. The line labeled upper bound corresponds to the maximum amount of melt possible for a given shock energy; i. e., $M_f = L$. The error bar shown on the graph arises from the difference in the melt fraction from the in-plane and out-of-plane micrographs in Marko-1064 results. The aluminum alloy had 6 % Si by weight and was spherical with diameters in the 30 to 70 μm range. The melt fraction reported in the shock consolidation of Al+6%Si powder was determined by microprobe analysis because of the observation that the distribution of Si was much more homogeneous in the melted and rapidly solidified regions. The quantitative melt fraction results found in the literature for steel powders are not as reliable [5]. The steel melt fraction results were obtained from the percentage of material which transformed to the martensitic phase. This estimation of the melt fraction is inaccurate since steel, rapidly cooled from only 800 C, will form the martensitic phase, whereas temperatures up to 1500 C are required for melting [8].

The dependence of melt fraction on shock energy for irregularly shaped Markomet 1064 indicates the existence of a shock energy threshold. Measurable melting occurs only for shock energies above this threshold which is around $L = 0.27$ for Markomet 1064. The spherical aluminum powder data also have a melt threshold, but at $L = 0.16$. The functional dependence of the melt fraction, M_f , on L can be fit by the linear equation,

$$M_f = M_0(L - L_0), \quad (4.6.2)$$

where L_0 is the melt fraction threshold and M_0 is the slope. For the irregularly shaped Markomet 1064 powder, L_0 and M_0 are 0.27 and 0.59, respectively. For the spherically shaped Al+6%Si powder, L_0 and M_0 are 0.16 and 0.89, respectively. Since the melt data are sparse, the linear dependence of melt fraction on shock energy is not firmly established. Nonetheless, it is clear that shock waves are much more efficient in melting the surfaces of the spherical aluminum particles than the irregularly shaped Markomet 1064 particles and that the upper bound does not adequately describe the actual amount of melt.

4.7 Summary

The results presented in this chapter are briefly summarized below.

From the recovery experiments of AISI 9310 steel powders, we have learned that:

1). The interparticle bonding is not effective until the shock energy is above a threshold value of 200 kJ/kg.

2). At a shock energy of 500 kJ/kg, the mechanical strength of the compact reaches a maximum of 1.3 ± 0.1 GPa which is comparable to that of wrought steel.

3). The microhardness measurements alone are insufficient to determine the effectiveness of interparticle bonding in compacts. Nonetheless, when combined with UTS measurements they can be used to determine if complete bonding has been achieved, since the compact cannot be stronger than the particle strength deduced from the hardness.

4). For a shock energy of 400 kJ/kg, the shock duration must exceed 0.4 μ s in order to produce mechanically strong compacts.

5). Photomicrographs and SEM fractographs indicate that the good particle bonding occurs only at select areas where there are large plastic deformations.

The recovery experiments on molybdenum powders indicate that the surface oxides adversely affect the strength of compacted samples. Compaction of as-received molybdenum powders resulted in samples with no cohesive strength, while consolidation of molybdenum powders with reduced surface oxide coatings resulted in compacts with UTS of 0.76 GPa which is comparable to wrought molybdenum.

Microcrystalline powders of a glass forming alloy called Markomet 1064 used to study the interparticle melting produced in the shock consolidation process. The results of this study were:

1). Interparticle melting occurs only for shock energies above 190 kJ/kg.

2). The amount of interparticle melt is much less than that expected from upper bound arguments which assume that all of the shock energy is deposited near the particle surface.

3). The melt regions are inhomogeneously distributed and their geometries are complex.

Table 4.1 Properties of powders used in the shock consolidation and recovery experiments [2].

	<u>AISI 9310</u>	<u>Molybenum</u>	<u>Marko-1064</u>
Composition (by wt. %)	Fe _{94.5} Ni _{3.2} Cr _{1.39} Mn _{0.65} Mo _{0.24} C _{0.10}	Mo _{99.8}	Ni _{52.5} Mo ₃₈ Cr ₈ B _{1.5}
Typical density (g/cm ³)	4.82	6.12	4.48
Hardness (DPH)	344	-	1100
Shape	spherical	irregular	irregular
Size range (μm)	44-74	< 160	25-150

Table 4.2 Properties of the wrought materials whose powder forms were used in the shock consolidation experiments [3,8].

	<u>AISI 9310</u>	<u>Molybdenum</u>	<u>Marko-1064</u>
Density (g/cm ³)	7.90	10.22	8.96
Hardness (DPH)	320	-	-
Tensile strength (GPa)	1.0-1.2	0.7-2.1	-

TABLE 4.3. Shock wave consolidation data for 44-74 μm AISI 9310 powders of distension $m = 1.64$.

Shot #	Flyer Velocity (mm/ μs)	Shock Pressure (GPa)	Shock Energy (kJ/kg)	Shock Velocity (km/s)	DPH	UTS (GPa)
754 ^{1,2}	1.29 \pm 0.03	3.6 \pm 3	94 \pm 9	1.5 \pm 0.2	393 \pm 50	\sim 0
733 ²	1.08	5.9	240	1.7	413 \pm 26	0.34
713	0.96	7.0	280	1.8	413 \pm 26	0.76 \pm 0.09
727	1.21	10.1	410	2.2	510 \pm 20	1.18 \pm 0.02
734	1.22	10.2	410	2.2	441 \pm 10	1.12
728	1/37	12.4	500	2.5	502 \pm 16	1.30 \pm 0.14
730	1.60	16.0	650	2.8	482 \pm 15	1.29
733	1.72	17.9	730	2.9	500 \pm 11	0.81
757	1.79	19.0	770	3.0	422 \pm 13	1.18

¹Initial powder distension was 1.41. All others had a powder distension of 1.64.

²Shot 754 used a Lexan flyer. Shot 733 used a 2024 Al flyer. All other shots used 304 stainless steel flyers.

TABLE 4.4. Results of the shock consolidation of microcrystalline Markomet 1064 powder with distension of $m = 2.0$.

Shot #	Flyer		P_1 (GPa)	ΔE (kJ/kg)	Area Percentage of Melted Region		Melt Percent
	Material	Velocity (km/s)			Shock Plane	I	
807	Lexan	1.44±.10	3.4±0.3	190±15	0	0	0
805	304 S.S.	0.962	5.1	279	6±1	5±1	5±1
808	304 S.S.	1.09	6.3	350	19±4	8±1	13±5

Table 4.5 Thermal data for aluminum [19] and Marko-1064 [20]. The specific heat is the average value from 20 to 600 C.

	<u>Aluminum</u>	<u>Marko-1064</u>
Specific heat	1050 J/kg C	390 J/kg C
Melting Temperature	660 C	1160 C
Latent heat of Melting	3.97×10^5 J/kg	1.9×10^5 J/kg

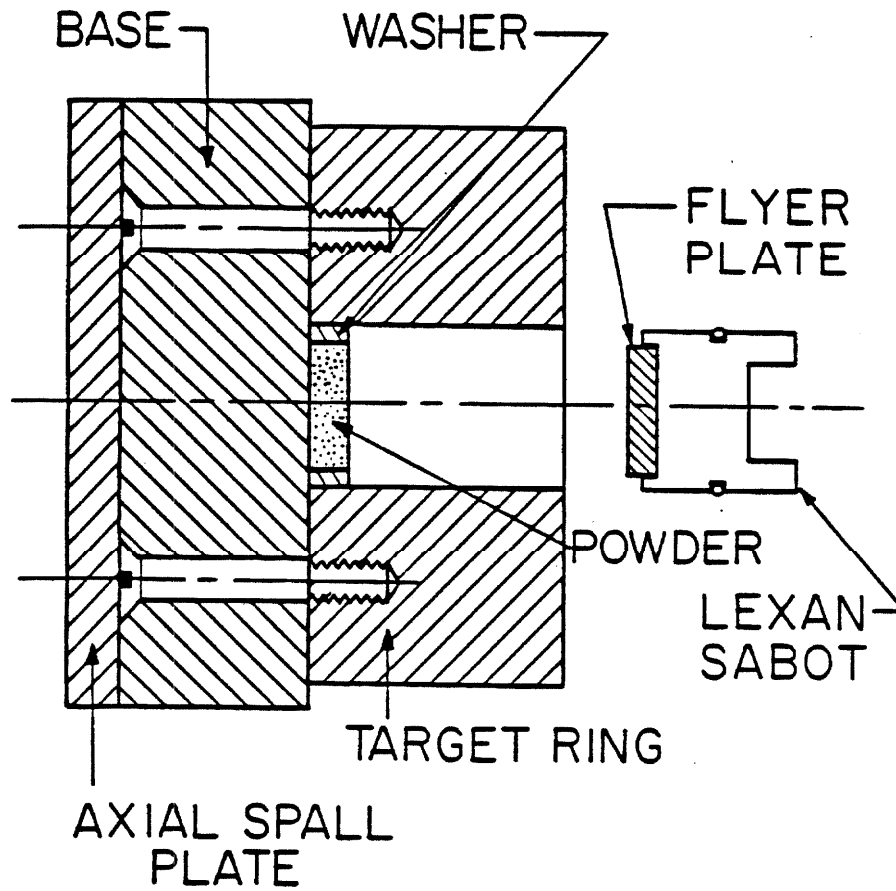


Fig. 4.1 Schematic cross section of the target recovery assembly. The dimensions of the target assembly are: a) 8.3 cm O.D. X 2.0 cm I.D. X 2.5 cm thick target ring, b) 8.9 cm diameter X 2.5 cm thick base, and c) 8.9 cm diameter X 3.8 cm thick axial spall plate.

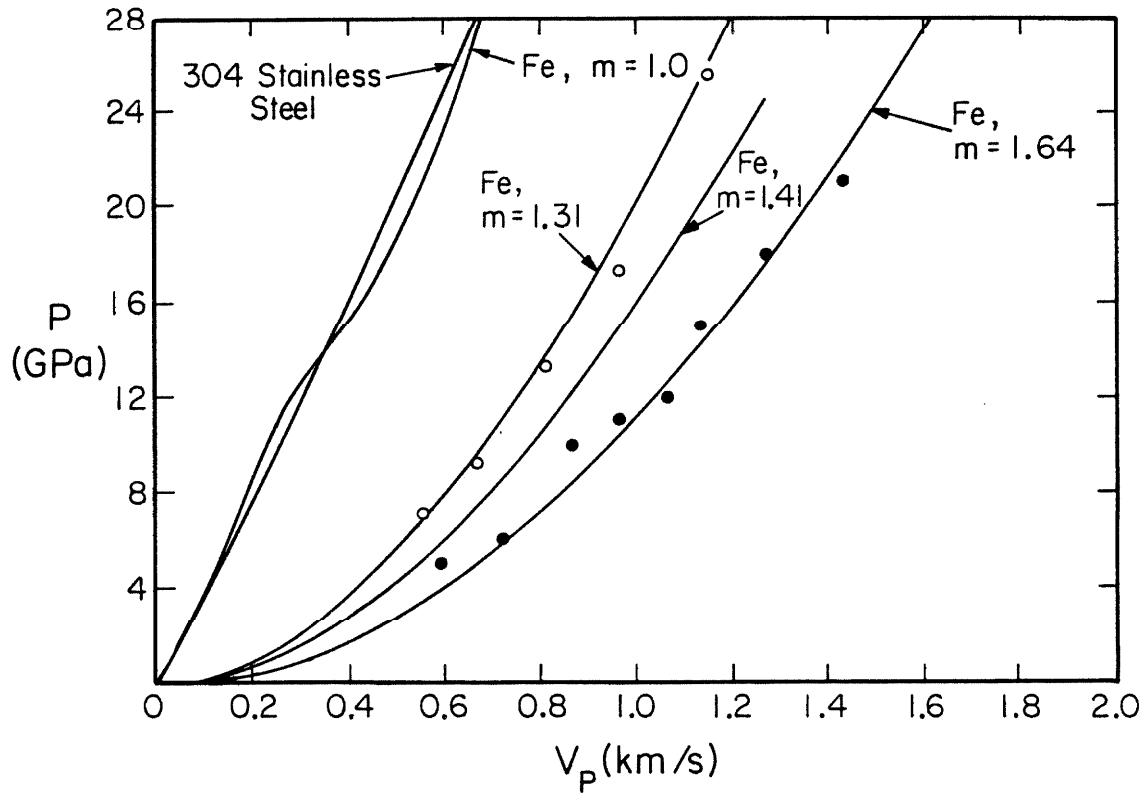
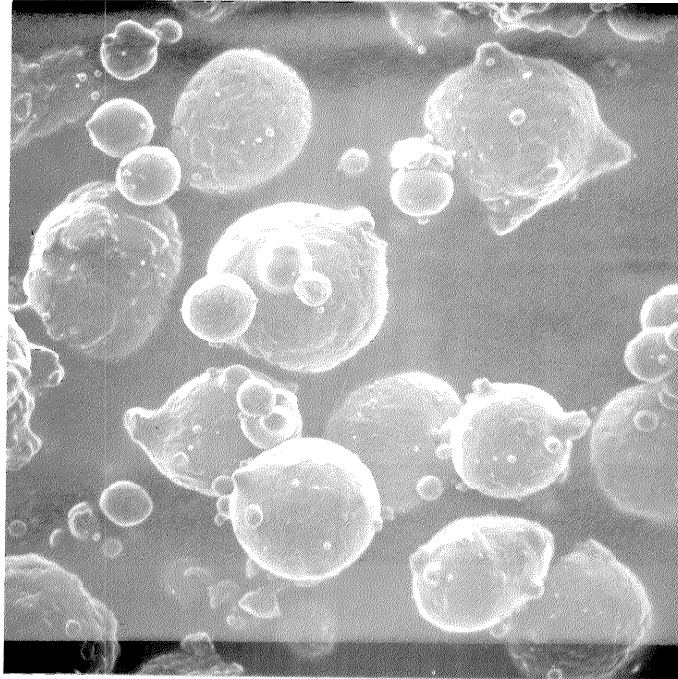


Fig. 4.2 Shock Hugoniot for pure iron [20], 304 stainless steel [21], and porous iron (points from Ref. [3], curves from Ref. [4]) used in calculations. The symbols + and x are the measured points for AISI 9310 with distension $m = 1.67$ and 1.43 , respectively.



20
20 μ m

Fig. 4.3 SEM micrograph of AISI 9310 rapidly solidified powder particles (-200 +300 mesh).

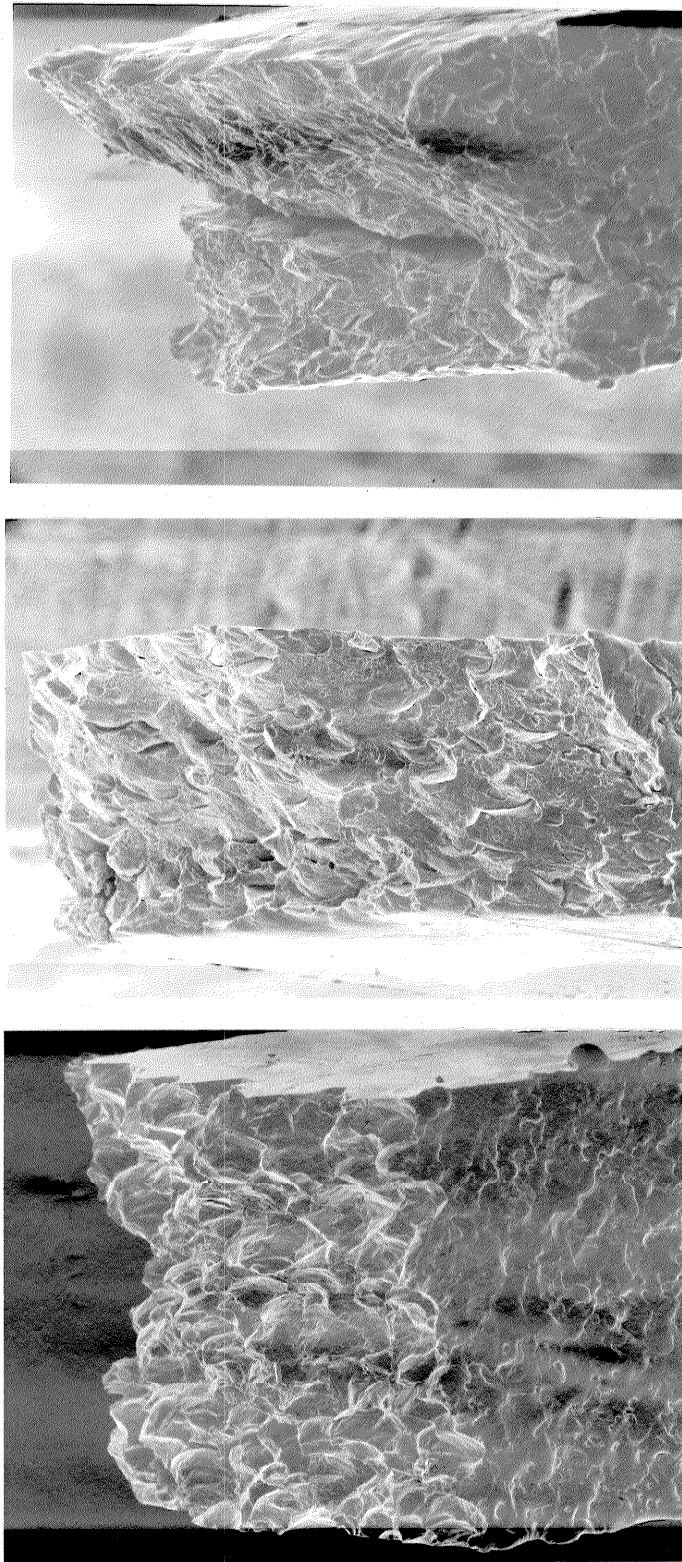


(A)

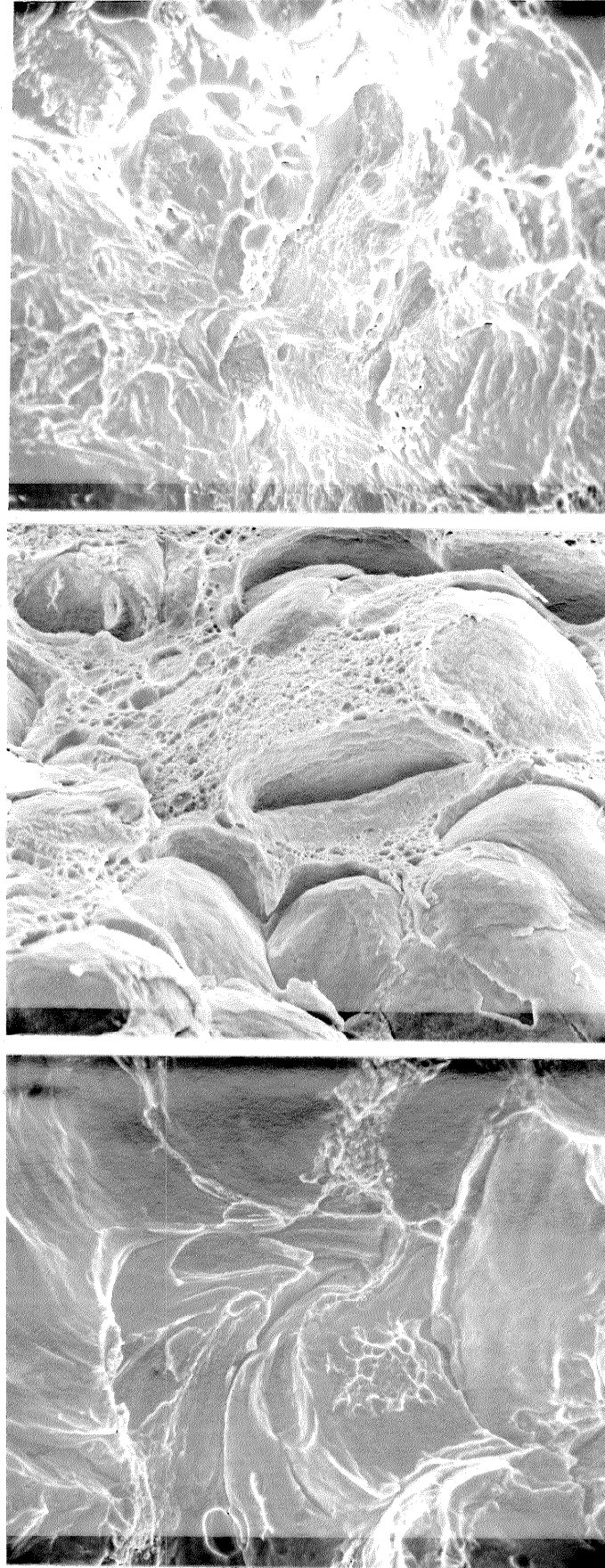
(B)

(C)

Fig. 4.4 Photomicrographs of compacted AISI 9310 samples with shock energies of: A) 240 kJ/kg, B) 500 kJ/kg, and C) 730 kJ/kg. Etchant = 5% nital, room temperature.



(A) (B) (C)
Fig. 4.5 Low magnification SEM fractographs of compacted AISI 9310 samples with shock energies of:
A) 240 kJ/kg, B) 500 kJ/kg, and C) 730 kJ/kg.



(A)

(B)

(C)

Fig. 4.6 Normal SEM views of fractured surfaces from compacted AISI 9310 samples with shock energies of: A) 240 kJ/kg, B) 500 kJ/kg, and C) kJ/kg.

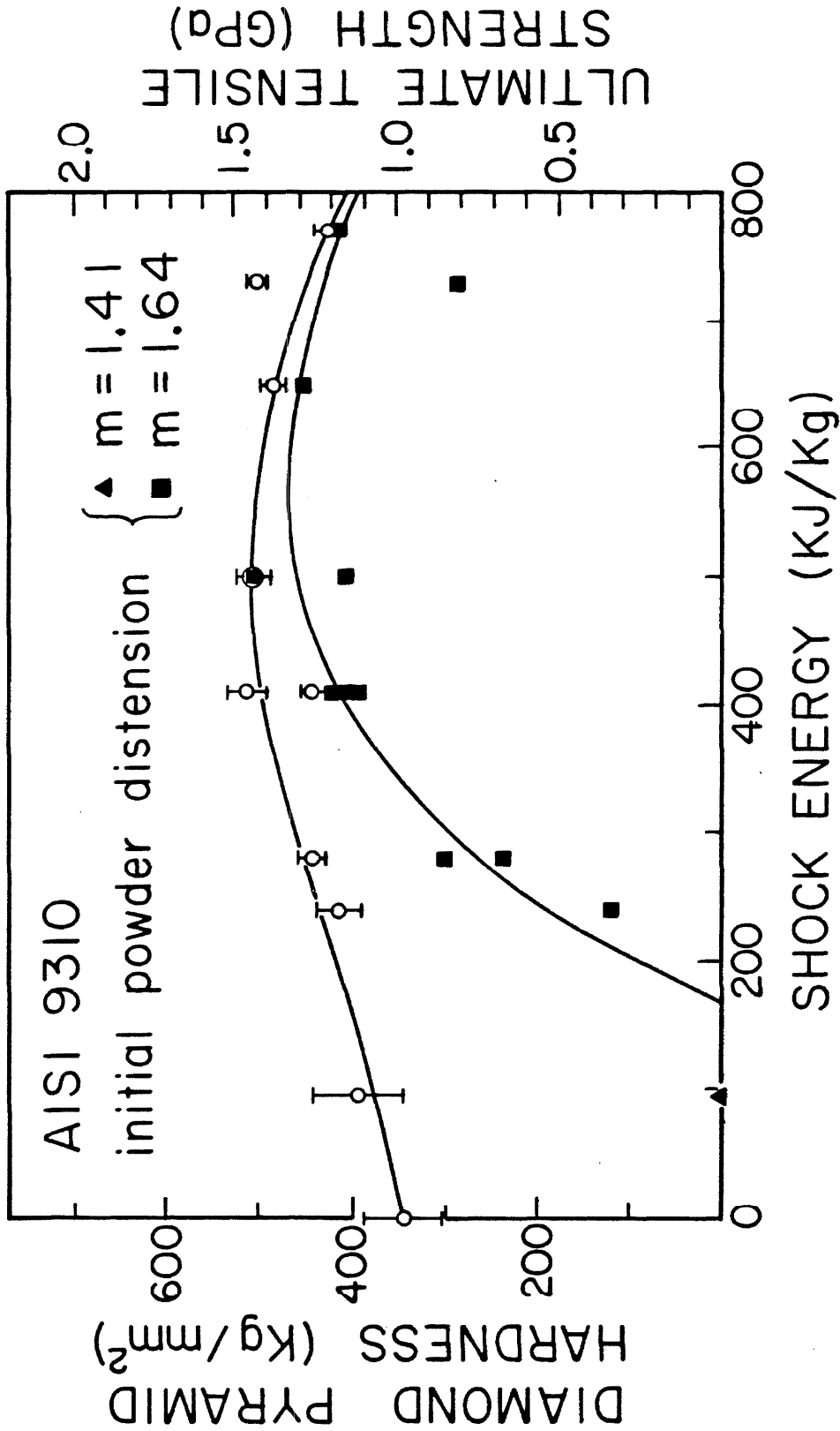


Fig. 4.7 Dependence of diamond pyramid hardness and ultimate tensile strength on the shock energy with a shock duration of 2-3 microseconds. The open circles are the DPH values and the closed squares are the UTS values.

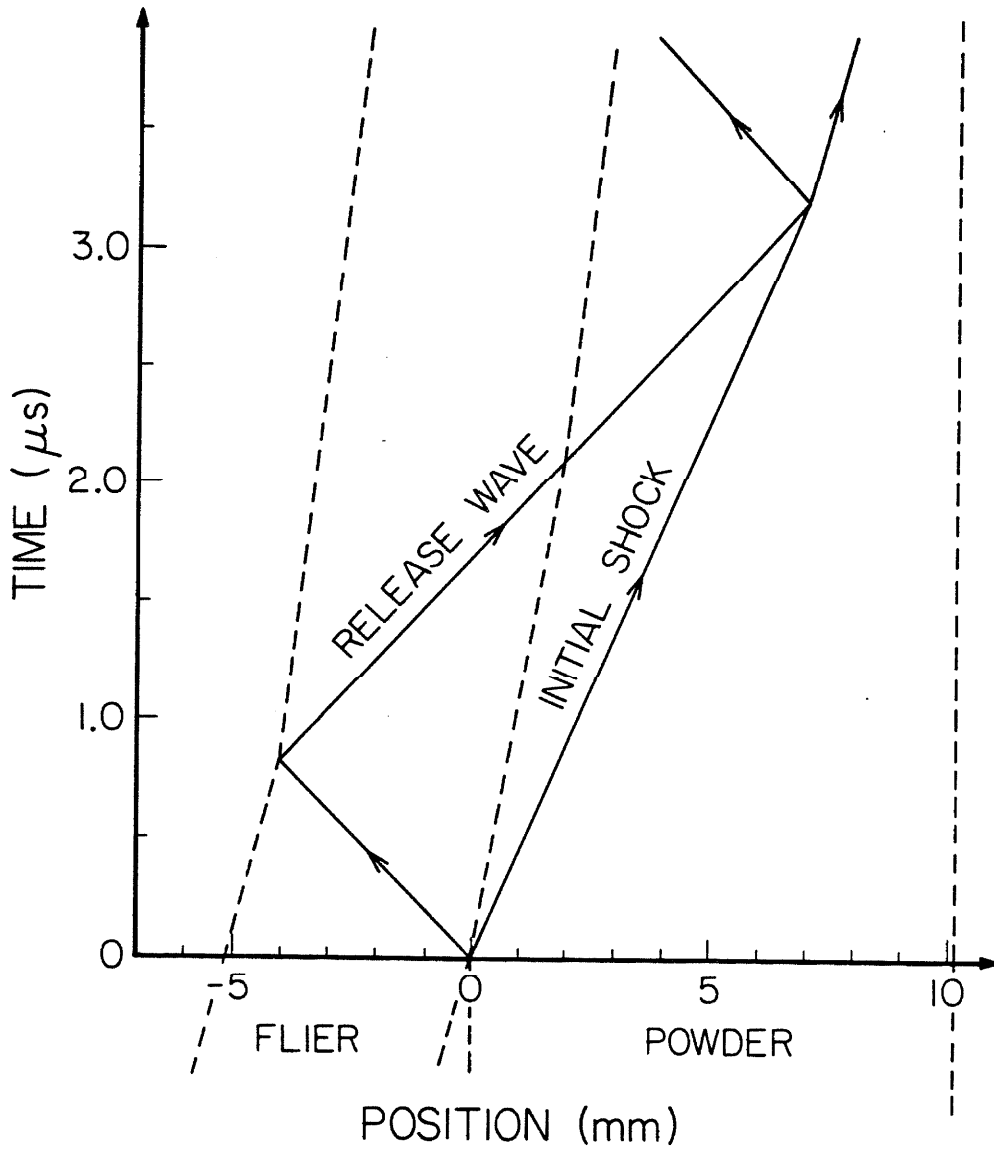


Fig. 4.8 Time-position histogram for the experiment in which the effect of the shock duration on AISI 9310 compact strength was measured. A 304 stainless steel flyer with a velocity of 1.16 km/s is shown impacting an AISI 9310 powder sample with $m = 1.69$. The diagram shows the leading edge of the release fan.

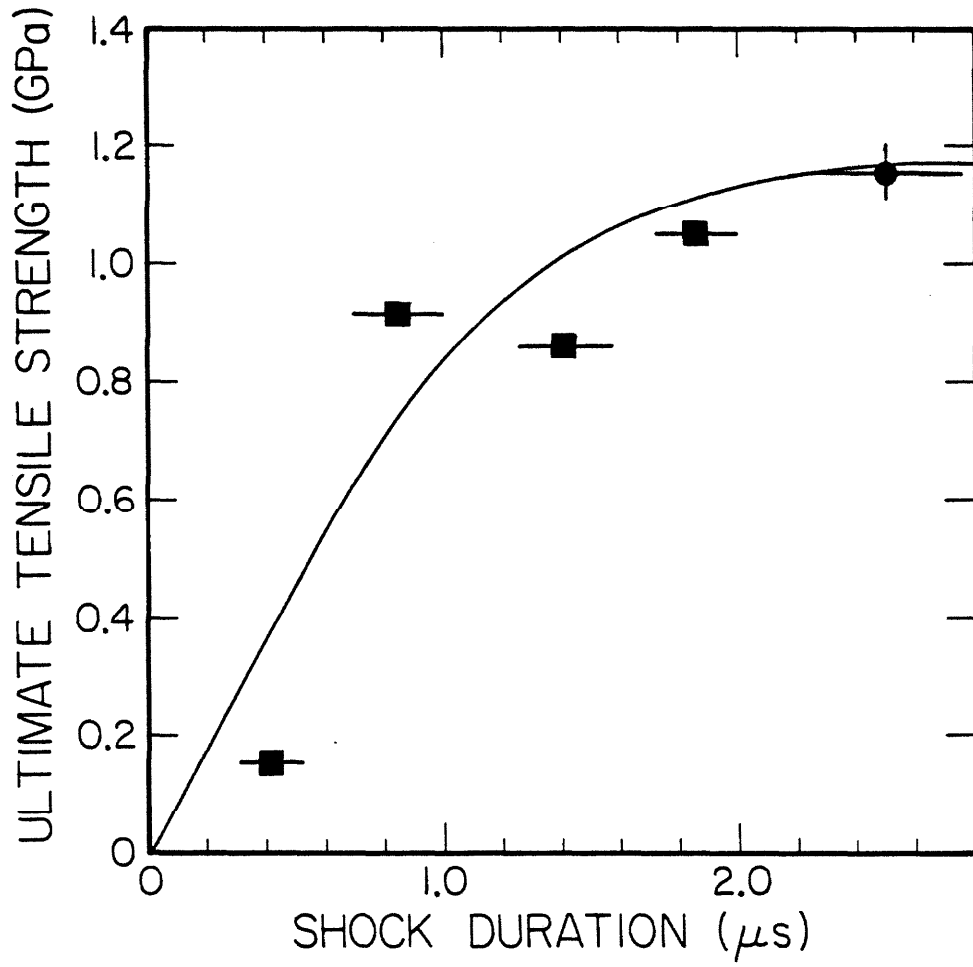
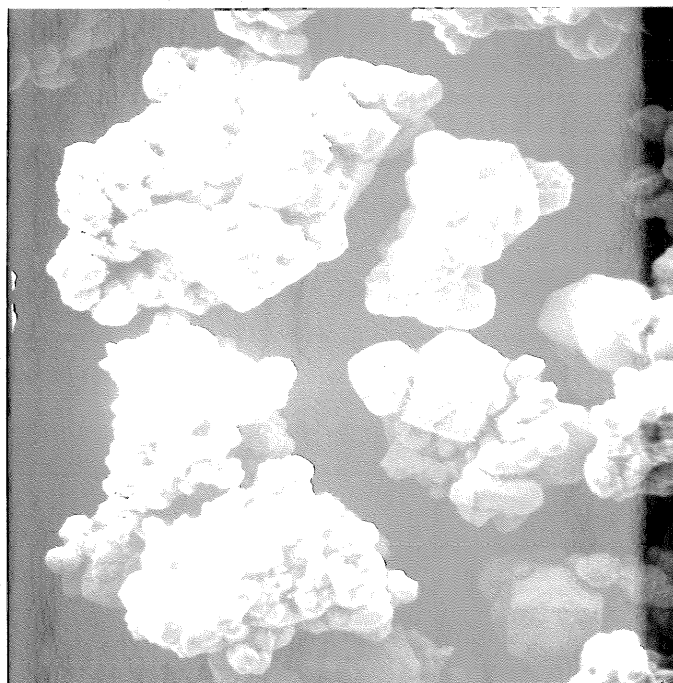


Fig. 4.9 UTS versus shock duration for AISI 9310 alloy consolidated at a shock pressure of 9.5 GPa and shock energy of 404 kJ/kg.



—
20 μm

Fig. 4.10 SEM micrograph of AMAX Mo powder.

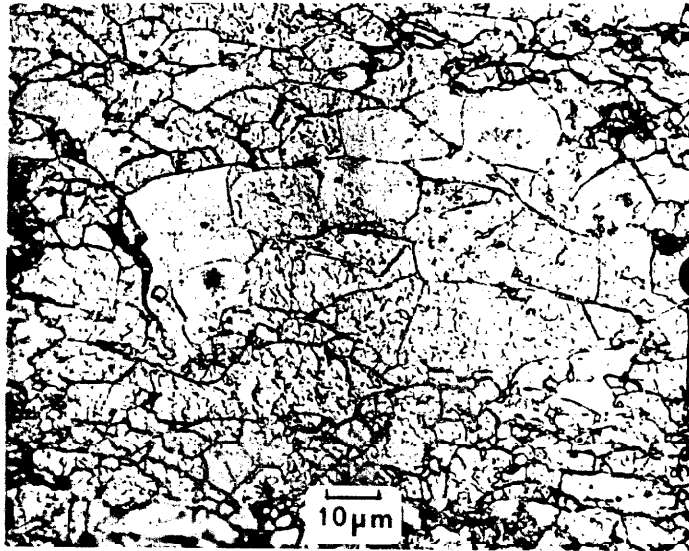
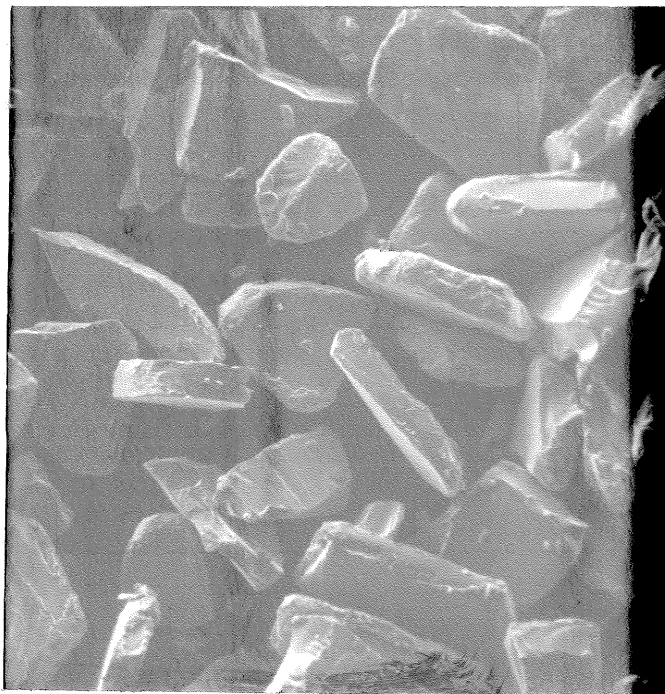


Fig. 4.11 Photomicrograph of the surface treated Mo consolidated with the shock energy of 580 kJ/kg. Etchant = Murikami's solution, room temperature.



┌
20µm

Fig. 4.12 SEM micrograph of Markomet 1064 powder.

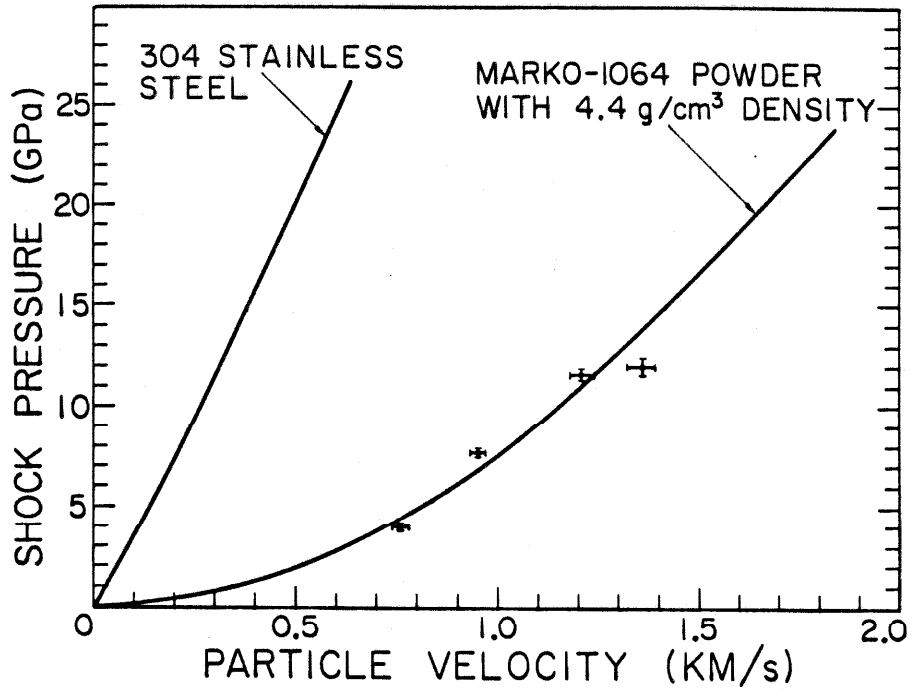
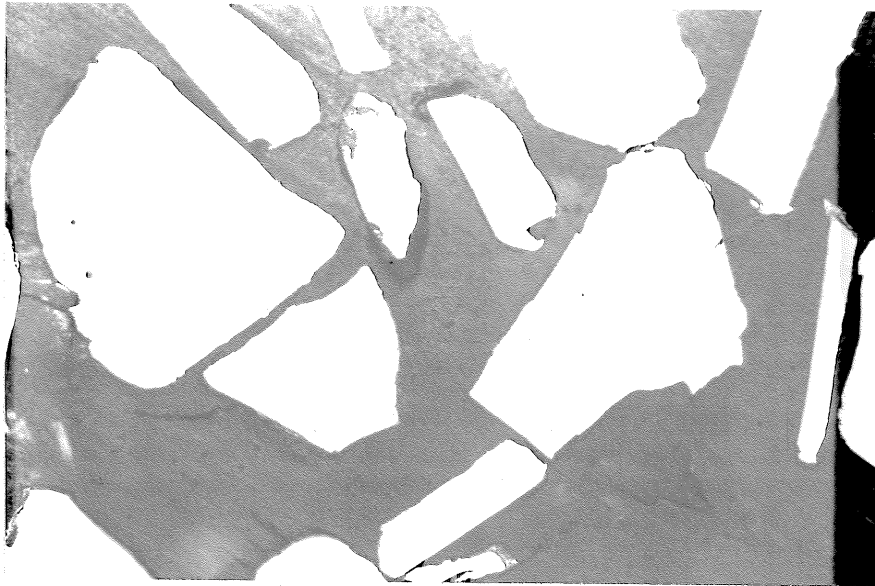
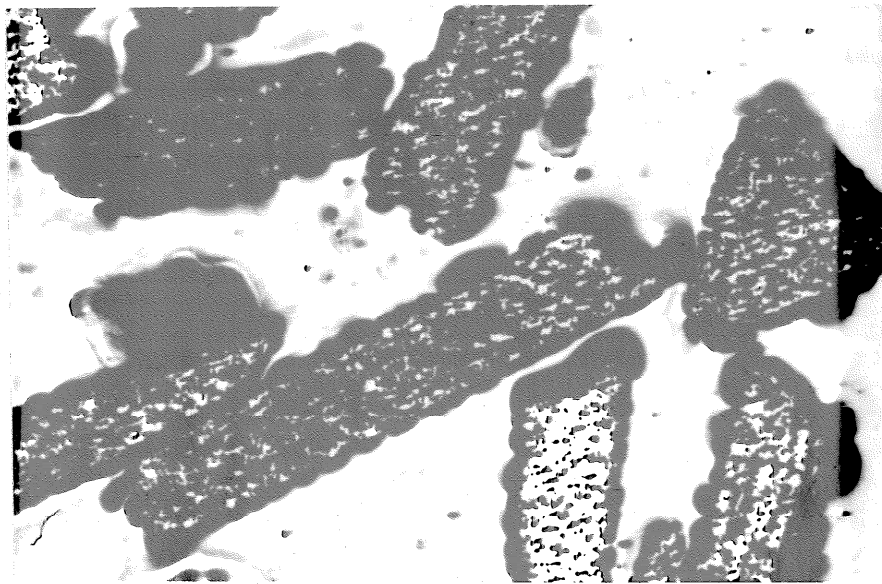


Fig. 4.13 Shock Hugoniot of Markomet 1064 powder for a distension $m = 2.0$ [12].

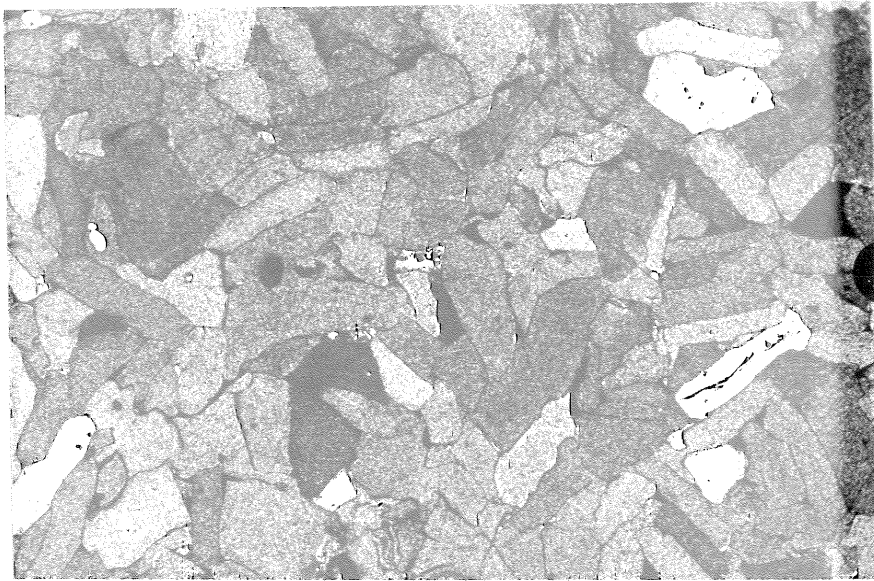


(A)

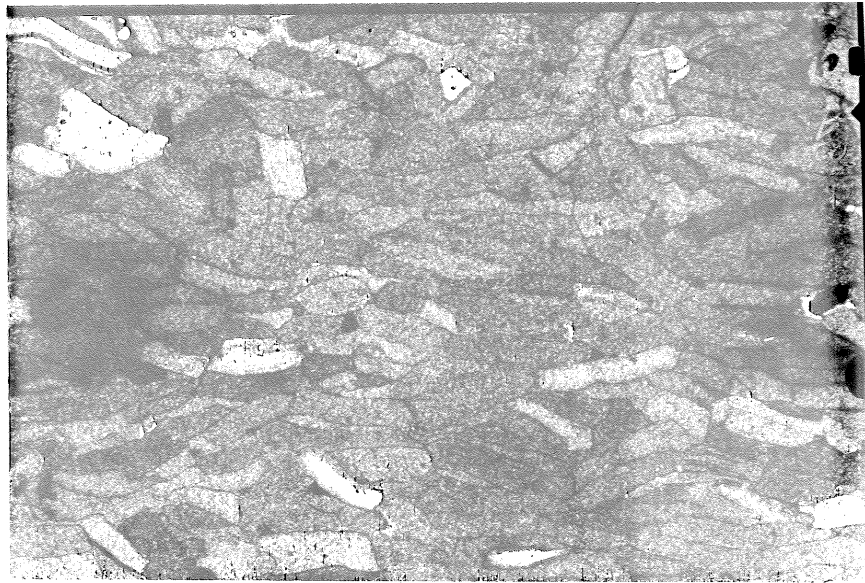


(B)


Fig. 4.14 Photomicrograph of Markomet 1064 powder in the: A) amorphous phase, and B) microcrystalline phase (annealed at 900 C). Etchant = Marble's reagent, room temperature. $10\ \mu\text{m}$

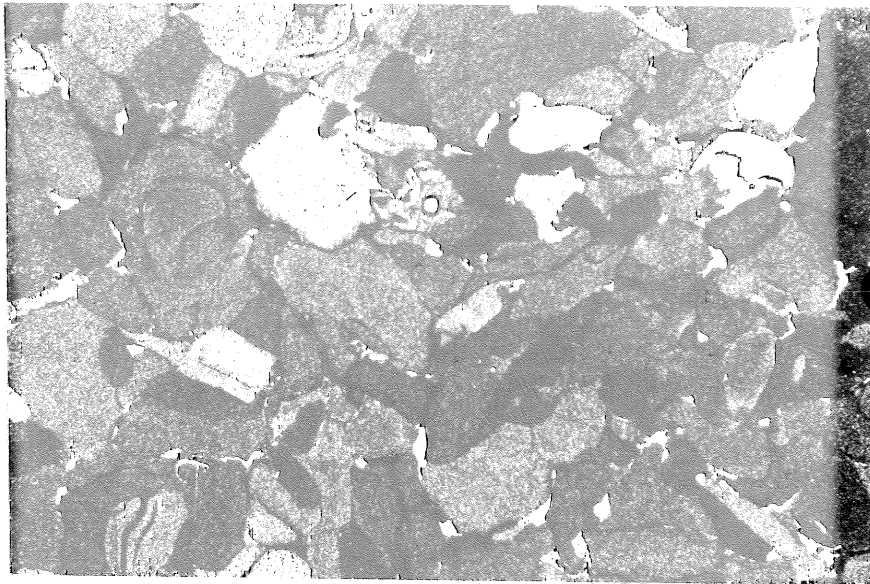


(A)

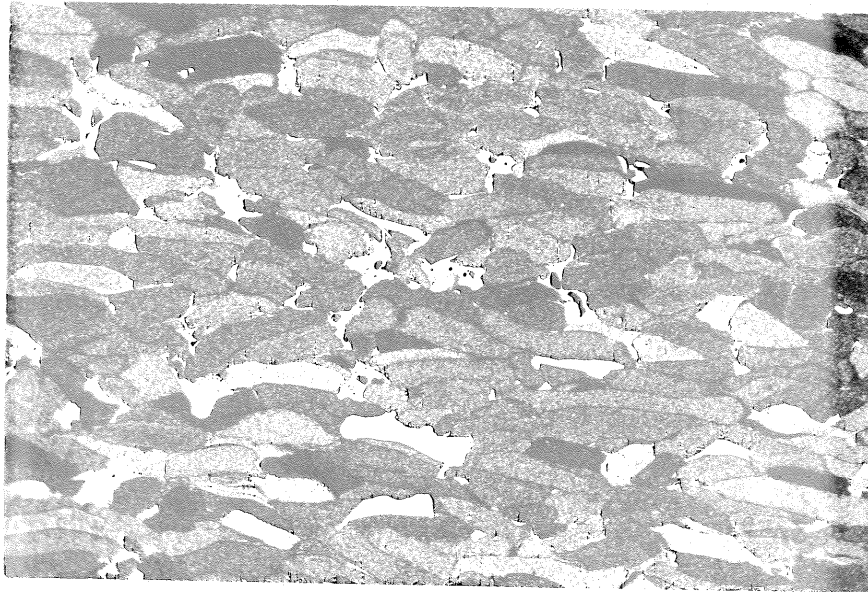


(B)


Fig. 4.15 Photomicrographs of compacted microcrystalline Markomet 1064 with shock energy of 190 kJ/kg: A) plane of shock front, and B) perpendicular plane to shock front (shock travel from top to bottom of picture). Etchant = Marble's reagent, room temperature.  50 μm

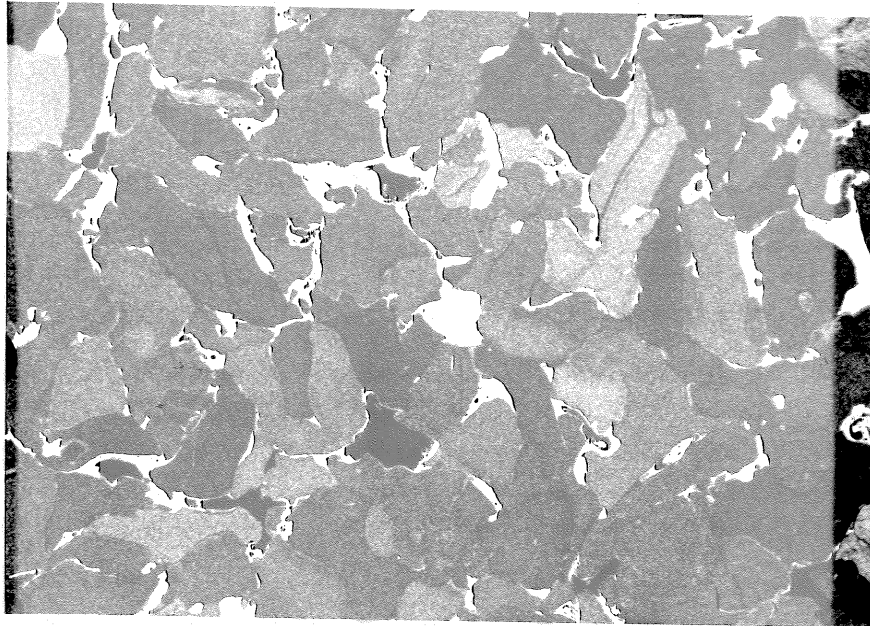


(A)

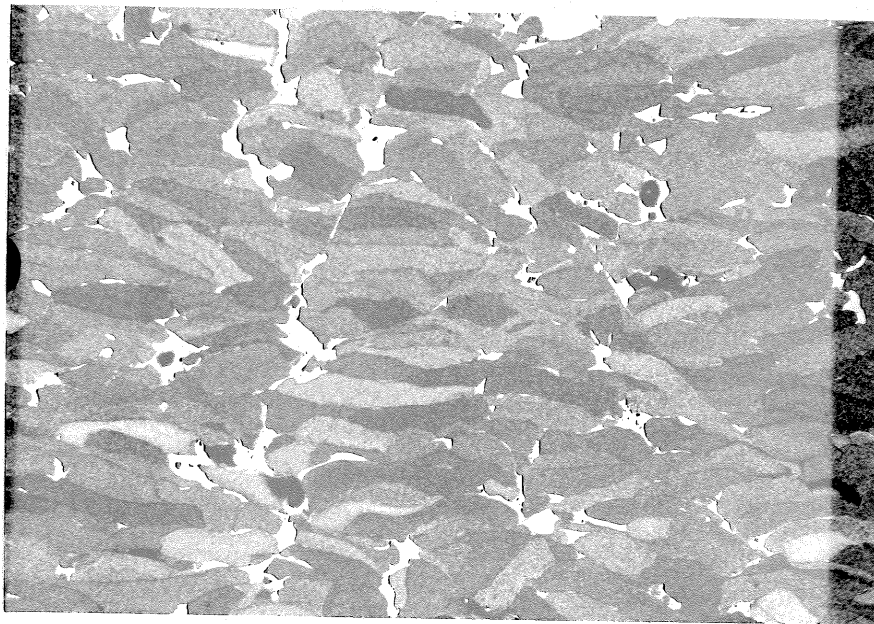


(B)


Fig. 4.16 Photomicrographs of compacted microcrystalline Markomet 1064 with shock energy of 279 kJ/kg: A) plane of shock front, and B) perpendicular plane to shock front (shock travel from top to bottom of picture). Etchant = Marble's reagent, room temperature.  50 μm

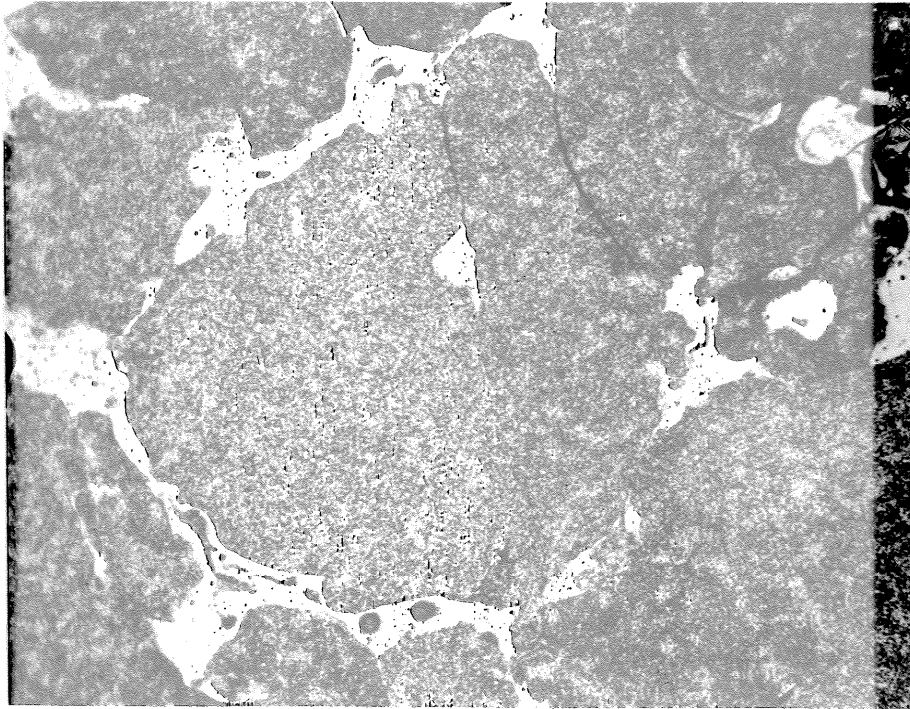


(A)



(B)

Fig. 4.17 Photomicrographs of compacted microcrystalline Markomet 1064 with shock energy of 350 kJ/kg: A) plane of shock front, and B) perpendicular plane to shock front (shock travel from top to bottom of picture). Etchant = Marble's reagent, room temperature.  50 μm



┌
10 μm

Fig. 4.18 Higher magnification photomicrograph (in the shock plane) of compacted microcrystalline Markomet 1064 with shock energy of 350 kJ/kg. Etchant = Marble's reagent, room temperature.

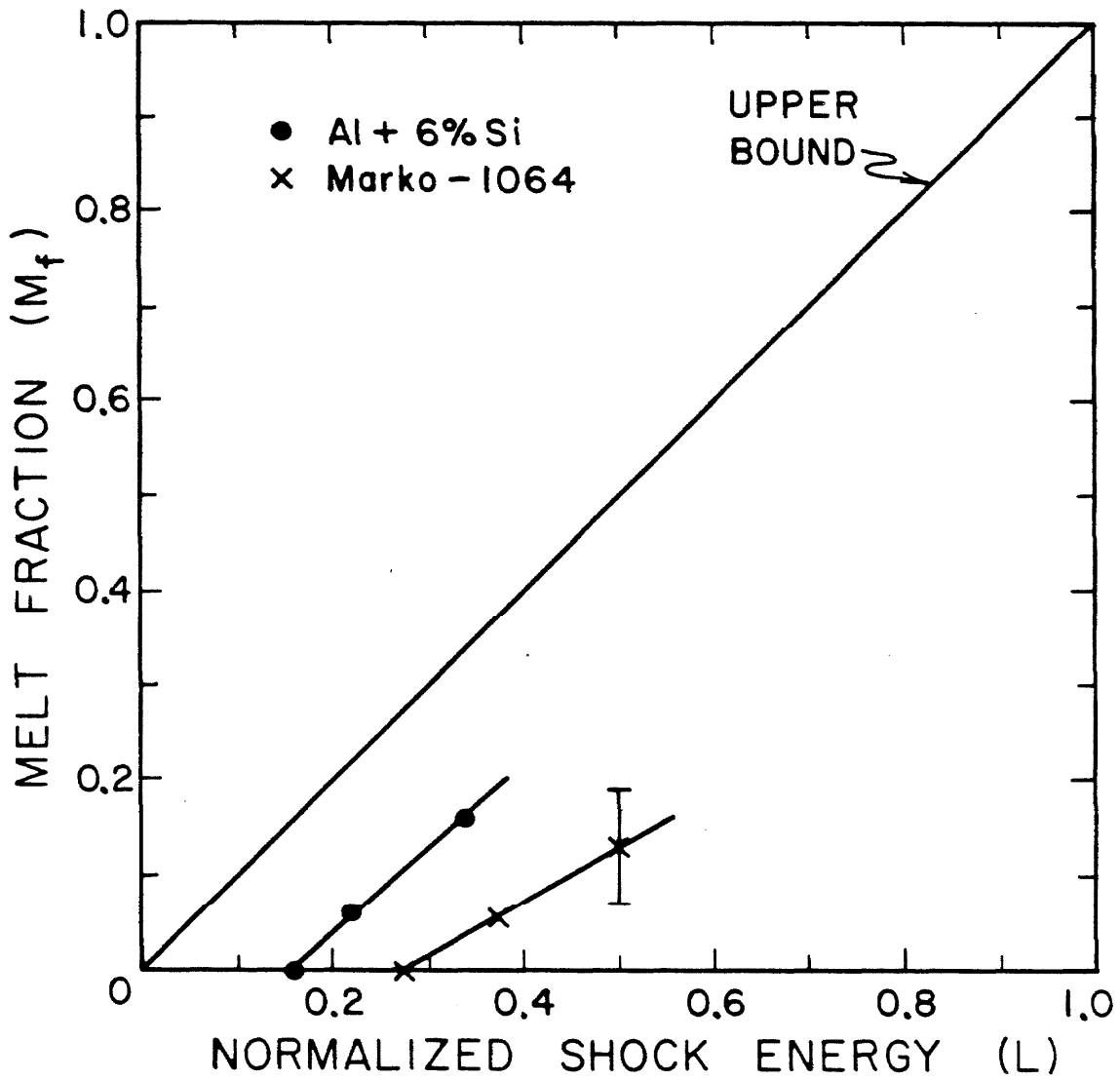


Fig. 4.19 Melt fraction data for Al+6%Si powder [15] and Mark-1064 powder in terms of the normalized shock energy, L , which is defined as the shock energy per mass divided by the energy per mass required to melt the material.

CHAPTER 4 REFERENCES

1. P. Kumar, PhD Thesis, Brown University, New York, New York, 1976.
2. Lemkey, F. D., private communication.
3. Hoyt, S. L., ed., Metals Properties, McGraw-Hill Book Company, New York, 1954.
4. Butcher, B. M. and C. H. Karnes, J. Appl. Phys., 40, 2967 (1969).
5. Simons, G. A. and H. H. Legner, J. Appl. Phys., 53, 943 (1982).
6. Raybould, D., J. Mat. Sci., 16, 589 (1981).
7. Morris, D. G., Metal Sci., 15, 116 (1981).
8. Lyman, T., ed., Metals Handbook Eighth Edition, Vol. 1, American Society for Metals, Novelty, Ohio, 1961.
9. Raybould, D., Int. J. Powder and Metallurgy and Powder Tech., 16, 9 (1980).
10. Murr, L. E., in Shock Waves and High-Strain-Rate Phenomena in Metals, Ch. 37, M. A. Meyers and L. E. Murr, ed., Plenum Press, New York, 1981.
11. Weast, R. C., ed., Handbook of Chemical and Physics, 55th Ed., CRC Press, Cleveland, 1974.
12. Marsh, S. P., ed., LASL Shock Hugoniot Data, University of California Press, Los Angeles, 1980.
13. Kasiraj, P., D. Kostka, T. Vreeland, Jr., and T. J. Ahrens, J. Non-Crystalline Solids, 61&62, 967 (1984).
14. Vreeland, T., Jr., P. Kasiraj, T. J. Ahrens, and R. B. Schwarz, in Proc. Materials Research Soc. Conf., Nov. 14-17, 1983, Boston, Mass., in press.
15. Morris, D. G., Mat. Sci. and Eng., 57, 187 (1983).
16. Gourdin, W. H., J. Appl. Phys., 55, 172 (1984).
17. Schwarz, R. B., P. Kasiraj, T. Vreeland, Jr., and T. J. Ahrens, Acta Metall., 1984, in press.
18. Strong, H. M., and F. P. Bundy, Phys. Rev., 115, 278 (1959).

19. Touloukian, Y. S., ed., Thermophysical Properties of High Temperature Solid Materials, Vols. 1-6, The MacMillan Company, New York, 1967.
20. Schwarz, R. B., private communication.
21. Walsh, J. M, M. H. Rice, R. G. McQueen, and F. L. Yarger, Phys. Rev., 108, 196 (1957).
22. McQueen, R. G., S. P. Marsh, J. W. Taylor, J. N. Fritz, and W. J. Carter, in High-Velocity Impact Phenomena, R. Kinslow, ed., Academic Press, New York, 1970.

CHAPTER 5

SHOCK CONSOLIDATION MAPS

5.1 Introduction

In this chapter we will review the understanding of the shock consolidation process that was gained from the experiments described in the previous chapters.

The various characteristic time scales in the shock consolidation process are listed and their relative importance and roles are discussed in section 5.2. The criteria for producing well-bonded compacts are enumerated in section 5.3. The criteria for good consolidation are evaluated for the AISI 9310 steel powder results in terms of a shock consolidation map in section 5.4. The possible mechanisms which preferentially deposit energy on the particle surfaces are discussed in section 5.5. The existing models for shock consolidation are evaluated in terms of the melt threshold condition in section 5.6. Some concluding remarks are presented in section 5.7.

5.2 Characteristic Times in the Shock Consolidation Process

The shock consolidation of powders involves several distinct processes characterized by time constants t_i . These are listed in Table 5.1. The numerical values quoted in the last column of this table correspond to typical values for our experiments on AISI 9310 steel powder. The first four time constants depend on the shock conditions and powder parameters. The last time constant can be controlled through experimental design.

1). Energy deposition Densification of the powder takes place within the shock front of width w . Therefore, t_r is the rise-time of the shock wave. Measurements of shock rise-times in copper give t_r of less than 23 ns. This indicates that w is less than $37 \mu\text{m}$ and approximately equal to one particle diameter. Thus, for a particle with a diameter of $58 \mu\text{m}$, a typical shock velocity of 2 km/s would result in a shock rise-time of 29 ns. Melting and bonding of the particles surfaces occurs during t_r .

2) Solidification After the passage of the shock front, the molten regions must solidify by conduction of heat into the relatively cooler particle interiors. An exact calculation of the time t_s necessary for all the melt to solidify [1-3] cannot be performed without knowledge of the shape and size of the melted regions as well as the temperature distribution after the passage of the shock front.

3) Relaxation to homogeneous temperature Immediately following solidification the temperature in the compact is highly inhomogeneous. The relaxation time t_h for reaching a homogeneous temperature T_h within the compact is given by the approximate relation (see Section 2.6)

$$t_h = d^2/64 D_m \quad (5.2.1)$$

where d is the diameter of the powder particle. Using $d = 58 \mu\text{m}$ in equation 5.2.1 and the data in Table 5.2, we obtain $t_h = 10 \mu\text{s}$. This time is a factor 4 longer than the duration $t_d = 2.5 \mu\text{s}$ of the shocked state in the steel powder consolidation experiments. Therefore, the homogeneous temperature is achieved after compaction, when the sample is in the unloaded state. Thus t_h is not a parameter relevant for the

successful recovery of the compact. However the value of t_h may be important in determining microstructural changes following the rapid solidification of the melted fraction, and thus relevant to the strength of the final product.

4) Relaxation to the ambient temperature The temperature of the compacted sample will relax to the ambient temperature in time t_a . The value of t_a will depend on the specific experiment. The minimum value of t_a is of order $t_h (\ell/d)^2$, where ℓ is the smallest dimension of the compact. Since $\ell \gg d$, $t_a \gg t_h$. If the homogeneous temperature, T_h , is high, the relatively slow cooling of the sample from T_h to ambient temperature may result in unwanted metallurgical changes. In a typical experiment, $\ell = 1.3$ mm which gives $t_a = 5$ ms. The actual cooling times will be longer if the compact does not have an ideal thermal contact with the recovery assembly.

5) Shock duration The duration of the shocked state, t_d , can be controlled through experimental design, i. e., by changes in thickness of the flyer. Figure 2.10 in Chapter 2 shows a typical pressure-time history in our experiments, at two extreme points in the powder: one on the impact surface (solid line) and the other on the surface of contact with the target base (dash lines). The average shock duration was approximately 2.5 μ s in the recovery experiments, as depicted in the figure.

In these experiments the initial shock wave of amplitude P_1 produces complete densification of the powder. At a later time the compacted powder is shocked to pressure $P_2 > P_1$ for a duration less than t_d . However, the parameter of importance for the consolidation is the time of positive pressure, t_d , indicated in Fig. 2.10.

5.3 Criteria for Successful Shock Consolidations

1). Minimum shock energy In order to produce shock consolidated material with mechanical strengths approaching that of solid material, enough interparticle melting must occur to disperse a sufficient amount of the surface oxides. However, melting begins to occur only if the shock energy is above some critical value. Possible reasons for the existence of the threshold will be discussed in section 5.6.

2). Minimizing the surface oxides The requirement of enough shock energy to cause melting is not a sufficient condition for producing well-bonded compacts, as demonstrated in the case of molybdenum powders, where the reduction of oxides in the powder greatly enhanced the strength of the consolidated material. Thus the surface oxides should be made as thin as possible in order to minimize the melt fraction required to disperse the surface oxides adequately.

3). Minimum shock duration Following the passage of the initial shock front, the interiors of the particles are relatively cool while the boundaries between the particles are in the molten state. Therefore, successful consolidation will take place provided the melted regions solidify and cool to below T_m while the sample is still in the shocked state. Otherwise, the sample would disintegrate by tensile failure when rarefaction waves arrive at the compacted powder [4]. Thus successful shock consolidation requires

$$t_d \geq t_s + t_c \quad (5.3.1)$$

where t_s and t_c are the solidification and cooling times, respectively.

The cooling time following solidification must be sufficiently long for the compact to acquire mechanical strength. The degree of strength required is difficult to predict since it will depend on the particular experimental set-up, which determines the magnitude and duration of the tensile stress experienced by the compact in the recovery experiment. In well-designed experimental set-ups, momentum traps are provided which minimize the tensile loading of the compact in the recovery process. Another difficulty in estimating t_c is the paucity of data for the mechanical integrity of alloys subjected to short-duration tensile stresses at high temperatures.

4). Maximum shock energy If too much energy is deposited during the shock wave consolidation of the powder, the homogeneous temperatures could be high enough to result in the loss of metastable properties in the compacted material. For example, in the shock consolidation of AISI 9310 steel powders, the microhardness of the compacts begins to decrease for shock energies above 700 kJ/kg (see Fig. 4.7). This softening is due to the annealing effect of the high homogeneous temperatures.

The homogeneous temperature, T_h , can be calculated by the approximate relation

$$T_h = E/\bar{C}_p + T_0$$

where \bar{C}_p is the average specific heat. Using the value of \bar{C}_p for iron from Table 5.2, we obtain $T_h = 1060$ C with $E = 700$ kJ/kg.

5). Particle size limitation Although in the present study the effect of particle size on the shock consolidation process was not investigated, a lower limit on the particle size is to be expected. An estimate of the smallest particle size that can be consolidated by

shock waves follows from the necessary condition that $t_r \ll t_h$. Otherwise, the preferential energy deposited on the particle surface will not produce any inhomogeneous heating and melting. With $t_r = d/C_s$ (C_s = shock velocity) and t_h given by equation 5.2.1, this condition gives [5]

$$d \gg 64 D_m / C_s. \quad (5.3.1)$$

With the D_m value in Table 5.2 and a typical value $C_s = 2 \text{ mm}/\mu\text{s}$, equation 5.3.1 requires $d \gg 0.17 \mu\text{m}$.

A second consideration relates to the minimum amount of melted material. As the particle size is decreased, the increase in particle surface to volume ratio may necessitate a larger threshold melt fraction in order to break and disperse the surface oxides and impurities.

5.4 Shock Consolidation Map for Spherical Steel Powders

All of the criteria described in section 5.3 with the exception of the minimum powder particle size condition can be conveniently expressed in the form of a shock consolidation map which plots the dimensionless shock duration, τ , against the dimensionless shock energy, ϵ , defined as

$$\tau = 64 D_m t_d / d^2$$

and

$$\epsilon = E / [C_p (T_m - T_0)].$$

The reason for such a normalization will become apparent in the discussion to follow.

The tensile test results of AISI 9310 steel consolidation experiments are presented in Fig. 5.1. The unshaded circles denote compacts with very little strength. The half-shaded circles denote compacts of intermediate strength. The shaded circles denote compacts with strength approaching that of wrought material. The constant shock duration results were presented earlier in Fig. 4.7, while the constant shock energy results are from Fig. 4.9.

The solid vertical line labeled melt threshold represents the critical shock energy required to initiate the interparticle melting. The melt threshold line was estimated from extrapolating the UTS values to zero in Fig. 4.7 which should correspond to the onset of melt in AISI 9310 spherical steel powders. The dashed vertical line represents the effective lower energy limit due to the effect of surface oxides. The curved line, labeled minimum shock duration, schematically represents the lower limit for the shock duration which arises from the condition that the molten areas solidify before the high pressure state is released. The behavior of the shock duration limit as ϵ approaches 1.0 arises from the fact that, at $\epsilon = 1.0$, the homogeneous temperature of the compact is the melting temperature. Thus any molten material that is now introduced will have to solidify by heat conduction to the ambient temperature which is a much slower process. The maximum shock energy condition is not shown on the map since it depends on the particular metastable property one wishes to retain in the compact.

The shaded area on the shock consolidation map represents the shock wave regimes which should produce mechanically well-bonded compacts. For optimum results the consolidation parameters should be chosen so that they lie away from the boundaries. The use of such a map

is twofold. First it provides a concise way of presenting shock wave consolidation data. Secondly, it can be used to select the optimum conditions for shock consolidation of a powder once the boundaries are defined.

5.5 Energy Deposition Mechanisms

Ultimately, the effectiveness of the shock consolidation process for bonding powder particles together depends on the efficiency of the preferential surface energy deposition mechanisms. These mechanisms occur in the shock front of the initial wave traveling through a powder medium. Presently, these mechanisms are poorly and at best only qualitatively understood.

In the preceding chapters, indirect clues about these mechanisms were gained from the experimental measurement of shock rise-times and the amount of melted material produced by shock waves and from metallographs which showed the final shape of the deformed powder particles. In this section, we will review the various mechanisms and comment on their relative importance in light of the new understanding we have gained from the experiments.

A realistic powder medium consists of particles with varying shapes and sizes. Thus during the shock consolidation of such a medium, there will be a wide range of particle deformations and localized energy depositions. Nonetheless, in our discussions about shock deformation mechanisms, we will use the concept of an ideal particle whose shape and size are representative of the distribution. However, the statistical nature of the particle distribution should be taken into account when these ideas are applied to real problems. Furthermore, the classification scheme introduced below for the shock energy deposition

mechanisms is mostly for discussion purposes. All of these mechanisms are interrelated so there will necessarily be some overlap in their descriptions.

1). Plastic deformation In shock consolidations most of the initial voids in the powder medium must be eliminated by plastic deformation of the powder particles. For example, in a powder medium with a distension of 1.69, the void volume is 69% of the actual solid volume in the medium. Therefore, one would expect plastic deformation to play an important role in the shock consolidation process.

The deformation paths followed during the shock rise-time by the various infinitesimal volume elements in the powder particle depend on the details of how the shock waves reverberate within the particle. Nonetheless, we can state that the material near the particle surfaces which are close to large voids will be heavily deformed, while the interiors will be deformed much less. Due to the relatively large volume rearrangement required to eliminate voids, plastic deformation will unavoidably deposit energy over a fairly large region.

The role of the large plastically deformed areas in particle bonding is shown in Fig. 5.2. Figure 5.2 contains a photomicrograph of AISI 9310 steel powder which was consolidated with a shock energy of about 240 kJ/kg. The surface oxides have been dispersed mostly at junctions where three or more particles have been heavily deformed to produce converging collisions (marked by the letter "a" in Fig. 5.2). These junctions seem to be the dominant bonding areas as judged from the disappearance of the surface oxides. This is qualitatively confirmed by the SEM fractographs in Fig. 4.6 which show preferential interparticle bonding sites.

Although for low strain rates the stress required to initiate plastic flow is relatively small compared to the shock pressures, the flow stress can be significant at the extremely large strain rates found in shock wave consolidations. By assuming spherical geometry for both the powder and the void, a rough estimate of the average strain rate can be obtained from the relation

$$SR = (m-1)^{1/3} / t_r.$$

The functional form will depend on the chosen particle and void geometry. For $m = 1.69$ and $t_r = 30$ ns, we obtain a value 2.9×10^7 /s for strain rate. Although flow stress data do not exist for such high strain rates, we can estimate this property of metals from shock wave experiments [6]. In plane impact shock wave experiments it is observed that shear stresses substantially larger than the shear strength of the material can be sustained momentarily after impact [7]. The subsequent relaxation of these large shear stresses is manifested by the decay of an elastic precursor shock front. The relaxation is determined by the strain rate dependent plastic behavior of the material. Much effort has been spent in trying to predict this relaxation from models of the dislocation dynamics [8,9]. To estimate the dynamic shear strength, we need to know the time dependence of the precursor amplitude. In iron, for example, the shortest time from impact at which the precursor's amplitude was measured was 300 ns. By that time the amplitude had decayed from 6.8 GPa, at impact, to 3.5 GPa [10]. The shear stress is approximately half the amplitude of the precursor [9]. Since the shock rise-times are as short as 30 ns in the shock consolidation process, the plastic flow stresses can be quite large (up to one-half of the value

of the shock pressures). Thus a large part of the shock energy may go into plastically deforming the powder particles at these high strain rates.

2). Kinetic energy Applied shear stresses above the flow stress must result in the acceleration of the plastically flowing material. Thus the material flowing into large voids can gain kinetic energy. Some of the kinetic energy will be converted into heat when the void becomes filled. Melting caused from the "trapping" of kinetic energy is thought to occur in the shock cladding of metal sheets [11].

The actual conversion of kinetic energy into heat involves more plastic deformation and/or shock wave pressure heating at the collision points. The examples of particle bonding shown in Fig. 5.2 could also be due to the effect of the kinetic energy. The melt pools found in the Markomet 1064 experiments may have been caused by the concentration of plastic deformation and kinetic energy where large voids existed.

3). Shock pressure heating at stress concentration points The heating of solids by shock waves is small when the pressures are only in the 10 GPa range (which are the pressures attained after the passage of the shock front). However, in the shock front itself, there will be areas which have experienced much higher shock pressures due to point-like contacts between particles which act as stress concentration points. The high pressure shock waves produced at these points will decay in strength as they propagate and spread out into the particle interiors. These shock waves will have shock front widths of a few atomic spacings and have shock velocities much higher than the deformational shock front velocity of the powder medium. Thus the regions, which are near the particle surfaces where the stress

concentration points exist, will experience much higher shock pressures and energy deposition than the interior of the particles. For example, copper that has been shocked to 150 GPa and then released to the zero pressure state will have a temperature of 1220 C [12] which is above the melting point of copper at 1 atmosphere.

A possible example of the above mentioned mechanism is shown in Fig. 5.2 where there is gap in the oxide layer at a region which seems to be the original contact surface between the two particles (marked by the letter "b" in Fig. 5.2). However, since these types of bonds are seen infrequently on the micrograph, they seem to play a minor role in the shock consolidation process for AISI 9310 steel powders. The thin melt layers seen in the Markomet 1064 could also result from this effect (see Fig. 4.17).

Another aspect of the preferential surface energy deposition mechanism by shock pressure heating is the so-called double shocking of surfaces near gaps [13]. Consider the situation where two parallel surfaces are separated by a very narrow gap. When a shock wave arrives at the gap, the surface region near the gap is released from the shocked state by the release wave generated at the free surface at the gap. However, the shock and release waves impart momentum to the surface so that the gap is closed as one surface collides with the other. This generates a shock wave which reshocks the surface which was just released from the shocked state. Thus the surface experiences a double-shock and thus gains approximately twice as much thermal energy as the interior because, for small enough gaps, the double-shocking is restricted only to the surface since the second shock wave is faster than the release wave. This mechanism is efficient only near stress

concentration points where large pressures exist and the gaps are small. Thus for the present discussion it will be classified as part of the stress concentration mechanism of surface energy deposition.

4). Surface friction The concept of surface friction is usually applied in the phenomenological sense. Thus the description of the surface friction mechanisms will vary with the specific application. The large plastic deformations that occur at the particle surfaces will be influenced by surface friction effects and thus part of the plastic deformation could be defined as the surface friction mechanism.

At very high surface sliding velocities, the coefficient of friction drops dramatically in metals, presumably from the lubricating effects of any surface melting [14]. Thus, once a thin layer of molten material forms, the surface friction mechanism is essentially disabled. From micrographs such as those shown in Fig. 5.2, it is clear that the surface oxides are dispersed mostly at regions where the flowing materials converge. Thus most of the interparticle surfaces retain the oxide layers despite the possible action of surface friction. Therefore, any layer of molten material due to surface friction must be exceedingly thin.

5.6 Melt Threshold

Large homogeneous temperatures are undesirable since they may destroy metastable properties of the powder. Therefore, the minimum possible shock energy should be used to produce a well-bonded compact. This requires that 1) the shock energy be deposited as efficiently as possible on the particle surfaces to cause maximum melting for a given shock energy and 2) the surface oxides be initially reduced to a minimum. Improving the shock wave efficiency should result in the

lowering of the critical shock energy at which appreciable melting begins. Thus knowledge about the dependence of the melt threshold on the various shock and powder parameters would give valuable insights into the shock energy deposition mechanisms.

Table 5.3 contains all of the melt threshold results. The AISI 9310 melt threshold was deduced from the UTS measurements. Due to the paucity of melt threshold data, all of the following discussion must be considered tentative until further supporting evidence is gathered.

One possible reason for the threshold arises from the condition that the shock energy deposition be locally adiabatic [15]. In other words, the energy deposition must be faster than the heat conduction into the interior. This condition was applied to get the minimum particle size limitation in section 5.3. A quantitative model was recently introduced which incorporates this idea [16]. In this model the shock consolidation process is transformed into an idealized problem in which a spherically symmetric particle is subjected to a uniform and constant energy flux for a duration equal to the shock rise-time. The energy flux is chosen to be equal to the specific shock energy divided by the experimentally measured specific surface area of the powder. The radius of the sphere is scaled so that the total shock energy is conserved. This model is solved numerically which makes it difficult to use and evaluate. Nonetheless, the reported melt fraction predictions of the model are in reasonable accord with the Al+6%Si results [16].

The general applicability of the numerical model is still in doubt since it assumes: 1) all of the shock energy is deposited uniformly on the particle surface, 2) neglects material properties such as plastic deformation characteristics, and 3) spherical geometry and symmetry for

the powder particle. Another basic assumption behind such a model is that all of the heating is from surface friction. The results from the present investigation indicate that surface friction is not the dominant energy deposition mechanism and that on the surfaces the deposition tends to occur at specific areas. Also the importance of the plastic deformation cannot be neglected. The effect of high strain rate plastic deformation property of the material should play an important role in the consolidation process. In fact, one possible approach to the modeling of particle deformation would be to treat the material as a very viscous fluid. The geometry of the particles and the voids influences the deformation paths, and therefore should be taken into account. Thus, further experimental data to help elucidate some of these points are needed.

5.7 Concluding Remarks

The study of shock consolidation is still in its earliest stages. Before the process can be optimally applied to the fabrication of novel and useful materials, we must improve our understanding of the process. This optimization requires the knowledge of the relationships and importance of the various parameters in the shock consolidation process. The parameters of shock energy and shock duration were explored. Future investigations should study the effects of particle size and shape. In particular it is suggested that the technique of measuring the melt fraction from the amount of amorphous phase in the shock consolidated sample be used to study particle size and shape effects. These studies are important since they will give clues about the shock energy deposition mechanisms as well as give empirical data for the optimization of the shock consolidation process.

Table 5.1 Characteristic times in the shock consolidation process. These are typical values in the consolidation of 58 μm spherical powders of AISI 9310 steel. The solidification time was estimated from the dependence of UTS on shock duration. The other four times were calculated as explained in the text.

<u>Symbol</u>	<u>Process</u>	<u>Typical Value</u>
t_r	densification and melting	30 ns
t_s	solidification of melt	400 ns
t_h	thermal relaxation to homogeneous temperature	10 μs
t_a	thermal relaxation to ambient temperature	5 ms
t_d	duration of socked state	2.5 μs

Table 5.2 Thermal and thermodynamic properties of iron [14].

Specific Heat	c_p	450 J/kg K
	$c_{p,m}$	836 J/kg K
	\bar{c}_p	670 J/kg K
Thermal Conductivity	K	80.2 W/m K
	K_m	34 W/m K
Thermal Diffusivity	D	$1.26 \times 10^{-5} \text{ m}^2/\text{s}$
	D_m	$5.16 \times 10^{-6} \text{ m}^2/\text{s}$
Latent Heat of Fusion	H_m	$2.47 \times 10^5 \text{ J/kg}$
Specific	V_0	$1.27 \times 10^{-4} \text{ m}^3/\text{kg}$

The bar denotes an average over the regime $300 < T < T_m$.

The index m denotes property at $T = T_m$.

Table 5.3 The slope and intercept in the linear melt fraction vs shock energy relation, $M_f = M_0(L-L_0)$. The $Al_{94}Si_6$ results are from Ref. [16].

<u>Material</u>	<u>Shape</u>	<u>Size</u>	<u>M_0</u>	<u>L_0</u>
$Al_{94}Si_6$	Spherical	30-60 μm	0.89	0.16
Marko-1064	Irregular	25-120 μm	0.59	0.28
AISI 9310	Spherical	44-77 μm	-	0.12-0.16

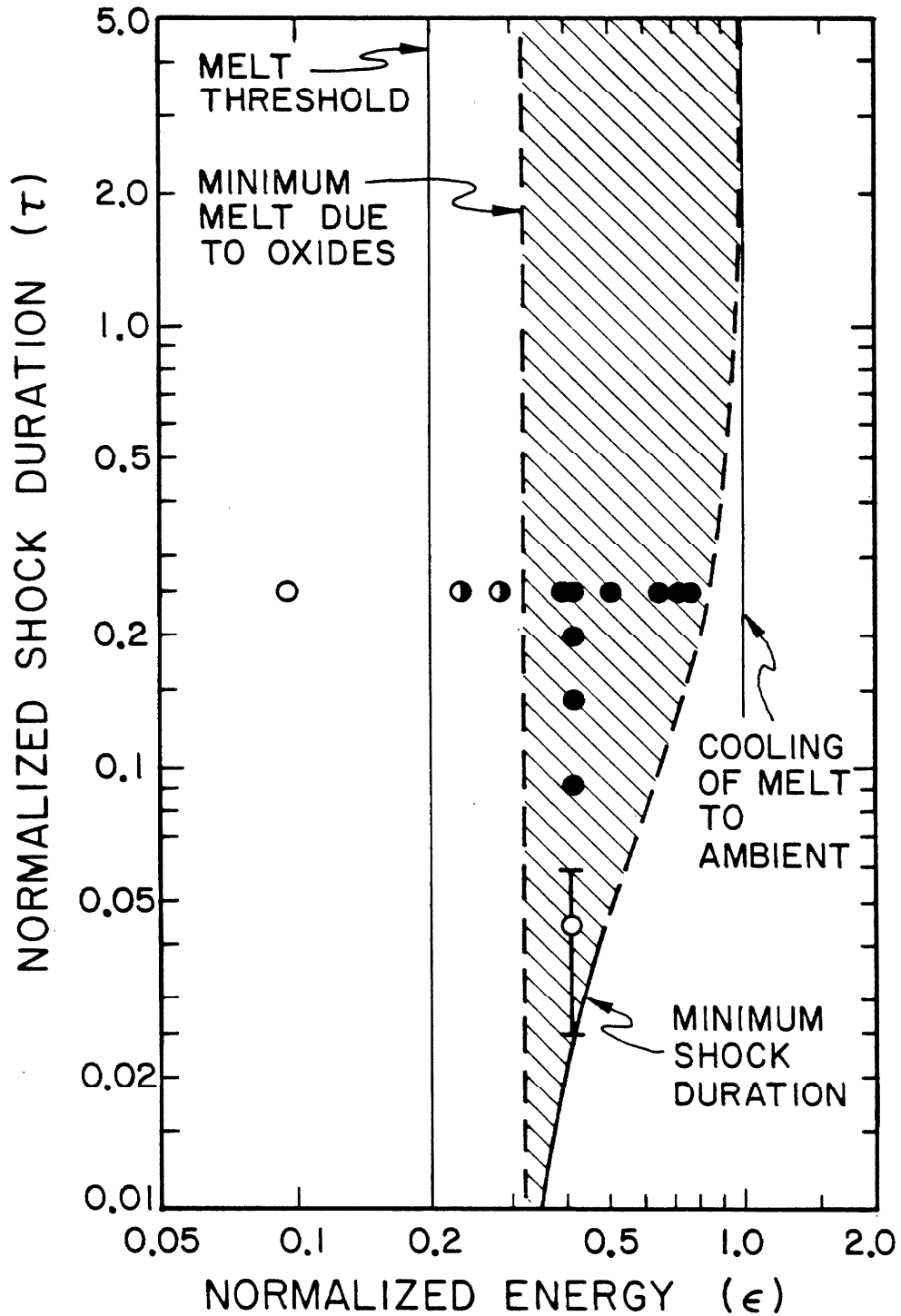
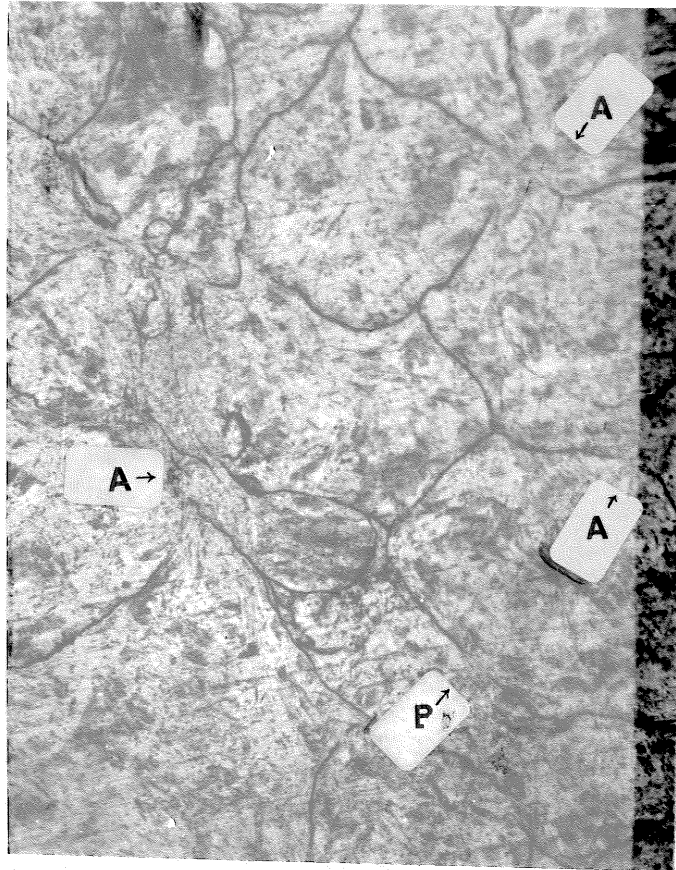


Fig. 5.1 The shock consolidation map for AISI 9310 steel powders. The clear circles denote compacts with UTS < 0.3 GPa. The half-filled circles denote compacts with 0.3 < UTS < 0.8 GPa. The filled circles denote compacts with UTS > 0.8 GPa. Refer to text for explanation of the features of the map.



10 μ m

Fig. 5.2 Photomicrograph in the plane of the shock wave of consolidated AISI 9310 powder (44- 74 μ m in diameter). The shock energy used was approximately 240 kJ/kg. The letter "A" denotes areas where the surface oxides have been dispersed by the converging collision of three or more deforming particles. The letter "B" denotes the area where oxides may have been dispersed due to high shock pressure at a point-like contact. Etchant = MoO₃ etch.

CHAPTER 5 REFERENCES

1. Carslaw, H. S. and J. C. Jaeger, Conduction of Heat in Solids, Oxford University Press, New York, 1947.
2. Murray, W. D. and F. Landis, J. Heat Transfer, 106 (May, 1959).
3. Tien, R. H., Trans. Metall. Soc. AIME, 233, 1887 (1965).
4. Staver, A. M., in Shock Waves and High-Strain-Rate Phenomena in Metals, Ch. 49, M. A. Meyers and L. E. Murr, ed., Plenum Press, New York, 1981, p. 865.
5. Schwarz, R. B., P. Kasiraj, T. Vreeland, Jr., and T. J. Ahrens, Acta Metall., in press, 1984.
6. Mikkola, D. E., and R. N. Wright, in Shock Waves in Condensed Matter-1980, Ch. IX:14, J. R. Asay, R. A. Graham, and G. K. Straub, ed., North-Holland Physics Publishing, New York, 1984.
7. Asay, J. R., G. R. Fowles, and Y. Gupta, J. Appl. Phys., 43, 744 (1972).
8. Abou-Sayed, A. S., and R. J. Clifton, J. Appl. Mechs., 44, 79 (1977).
9. Taylor, J. W., J. Appl. Phys., 36, 3146 (1965).
10. Taylor, J. W. and M. H. Rice, J. Appl. Phys., 34, 364 (1963).
11. Carpenter, S. H., in Shock Waves and High-Strain-Rate Phenomena in Metals, Ch. 53, M. A. Meyers and L. E. Murr, ed., Plenum Press, New York, 1981, p. 941.
12. McQueen, R. G., S. P. Marsh, J. W. Taylor, J. N. Fritz, and W. J. Carter, in High-Velocity Impact Phenomena, R. Kinslow, ed., Academic Press, New York, 1970.
13. Urtiew, P. A. and R. Grover, J. Appl. Phys., 45, 140 (1974).
14. Bowden, F. P. and D. Tabor, The Friction and Lubrication of Solids, Part II, Oxford Press, New York, 1968.
15. Raybould, D., Int. J. Powder Metallurgy and Powder Tech., 16, 9 (1980).
16. Gourdin, W. H., J. Appl. Phys., 55, 172 (1984).
17. Touloukian, Y. S., ed., Thermophysical Properties of High Temperature Solid Material, Volume 1-6, The MacMillan Publishing Company, New York, 1967.

APPENDIX A

FABRICATION OF POWDER THERMOCOUPLE

The thermocouple powder pills (depicted in Fig. 3.7) were fabricated by statically pressing the various layers of powder in a hollow steel cylindrical die (20.3 mm inner diameter) whose base could be detached after pressing to allow the removal of the powder pill from the die. The pressing was done in several steps. First, a thin layer of copper powder with parallel surfaces was formed at the base of the die by pouring in 1.00 gram of powder and leveling with a piston (20.3 mm diameter). This leveling was done, avoiding pressing the powder because, when powders are pressed in a die, the powder particles at the surfaces which are in contact with the die and piston tend to be flattened and aligned (unlike the particles in the interior which are arranged more randomly and interlockingly). Thus care was taken to avoid precompression of the first layer of the powder since the exposed top part was to be used as the thermocouple interface, and it was desired that the conditions there be as similar as possible to the interior. Also, intermediate pressing decreases the mechanical integrity of the powder pill. A 14 mm diameter quartz tube was carefully centered and placed on top of the first copper layer. Then, the central portion of the copper layer surface was masked by a 4.7 mm disc. The remaining exposed surface inside the quartz tube was covered with an approximately 0.5 mm thick layer of alumina powder. Alumina retains its insulating ability under extremely high shock pressure [1]. The disc used to mask the central portion was carefully removed and the quartz tube was filled with constantan powder. This results in a

circular copper-constantan powder interface at the center of the quartz tube, which is the active thermocouple junction. The outside of the quartz tube was then filled with copper powder until it covered everything, including the constantan powder in the inside of the quartz tube. Enough copper powder was added to insure a thick cover layer of copper. About 8 grams of copper were typically added in this final stage. This mixture was pressed with a piston up to 44.5 Knt. This produced enough pressure (0.14 MPa) to compress the copper and constantan powders to a density of 5.27 g/cm^3 .

Copper powder was used for encapsulation because both alumina and constantan powders did not have enough cohesiveness, unlike copper which held together upon removal from the die. The quartz tube was necessary for electrically isolating the thermocouple junction. Quartz was used because it is readily available and retains its insulating property under the shock pressures of interest. However, to minimize the effect of the impedance mismatch of the quartz with the copper powder, the quartz tube was made wide enough so that it would not affect the initial shock wave which impinges on the thermocouple junction.

After the powder pill was removed from the die, it was further encapsulated in epoxy to facilitate handling of the pill since it was still relatively fragile. The face which contained the first thin layer of copper was kept free of epoxy since it would be the face through which the shock wave would enter the powder from the buffer plate. Layers of the rear surface of the epoxy encapsulated powder pill were successively removed with 240 grit, boron-carbide abrasive paper, until the quartz tube was reached. This establishes the required electrical isolation of the outer copper powder from the inner constantan powder,

except for the connection through the thermocouple junction. The powder pill now resembles Fig. 3.7.

A test powder pill was made and strengthened by soaking it in a solution of acetone and Duco cement. When the test pill was removed and dried, it had sufficient strength to be abrasively sawed by a wire to reveal its cross section. The cross-section was similar to that depicted in Figure 3.7. The powder pills were held against the flat copper buffer plate by four epoxy beads on the sides.

The electrical circuit was formed by connecting the ground shield of a 50 ohm coaxial cable to the copper driver plate and by connecting the central wire of the coaxial cable to copper powder as shown in Fig. 3.7. The first electrical connection was made by soldering, while the last electrical connection was made with the use of silver paint. After the silver paint dried, the electrical connection was covered with epoxy for mechanical strength. The 50 ohm cable was then terminated by the 50 ohm internal impedance of the Tecktronix 485 oscilloscope.

APPENDIX B

ETCHANTS USED IN METALLOGRAPHY

5 % Nital [2]

5 ml HNO_3
100 ml Methanol or Ethanol

Murakami's Solution [2]

10 g $\text{K}_3\text{Fe}(\text{CN})_6$
10 g KOH or NaOH
100 ml H_2O

Marble's Reagent [2]

8 g CuSO_4
40 ml HCl
40 ml H_2O

MoO₃ Etch [3]

1.5 g MoO_3
50 ml HCl
50 ml HNO_3
50 ml H_2O

APPENDIX C

TENSILE TEST MEASUREMENTS

The steps required for making tensile strength measurements involve the preparation of the tensile test specimen from the compacted samples and the controlled pulling of the specimen to failure in a specially designed fixture.

Tensile Specimen Preparation

The compacted samples are sectioned into thin slices. In the present investigation, the sectioned slices were parallel to the impact face. The sections are mechanically polished on both sides to a thickness of about 1/4 mm using wet SiC paper and diamond paste through 1 μ m grit.

Dog-bone shaped tensile specimens are then made from the polished sections with the use of an Agietron spark cutting machine. The cutting tool of the Agietron acts as a cookie cutter and produces samples which resemble the shape of the tool. Since the recovered area (of the material compacted under well-defined conditions) is usually less than 10 mm in diameter, the dimensions of the cutting tool are such that the tensile specimens cut with the tool had a gauge length of 2 mm and a width of 0.7 mm.

Tensile Test Fixture

The dog-boned shaped tensile specimens are pulled to failure with the use of the fixture which is on the right in Fig. C1. The fixure on the left in Fig. C1 is used for ribbon shaped specimens. A closer view of the section that holds the tensile specimen is shown in Fig. C2. The holes in the tensile specimen are used as guides for pins. The pins are

used to measure the relative displacement of the two holes.

The fixture was designed to minimize tensile specimen bending and to operate under temperatures up to 600 C. The fixture contains a linear variable differential transformer (LVDT) which can measure the relative displacement of the two holes at the end of the dog-bone shaped tensile specimen. A Schawitz LVDT (Model 025 M-HR) and a DTR-450 digital transducer readout are used in the present fixture. This system is capable of measuring displacements as small as 0.3 μm . Since the tensile specimen is gripped and pulled from the two ends, the displacement measurement (i. e., the stretching of the tensile specimen under a pulling force) can be used to calculate the strain in the tensile specimen.

In order to minimize the effect of the strain in the fixture on the measurement of the stretching of the tensile specimen, the pulling force is applied through 1 mm diameter Mo wires that are attached near the gripping jaws. These wires are labeled "A" in Figs. C1 and C2. The coil of the LVDT hangs from the two guide wires that are attached to the pin in the upper specimen hole. The guide wires are labeled "B" in the figures. The core of the LVDT hangs from the hollow central tube that is attached to the lower specimen hole. This central tube is labeled "C." The lower Mo pull wire passes through the center of the tube. Since the pull force is applied directly to the jaws, the LVDT should measure only the relative displacement of the holes in the tensile specimen.

The tensile stress is applied by pulling on the ends of the two Mo wires with an Instron testing machine (Type TT-B-L). The force is measured by a reversible load cell, type A217-12, that can measure

increments of 0.2 lbs. (0.9 Nt) on its most sensitive scale.

The displacement measured by the LVDT and the force measured by the load cell are output as voltages. These voltages are recorded by a HP 7035B X-Y Recorder. The Y-scale (force or stress scale) is calibrated by placing standard weights on the load cell. The X-scale (displacement or strain scale) is calibrated by moving the coil of the LVDT relative to the core with a precise translational mount.

Tensile Test Measurement

An example of a tensile test measurement is shown in Fig. C3. The tensile specimen was made from a recovered AISI 9310 flyer used in a 15 GPa shock-wave consolidation experiment (shot no. 758). The force scale was converted into the stress scale by dividing the force by the initial cross section of the tensile specimen (0.64 mm X 0.30 mm). The displacement scale was converted into the strain scale by dividing the displacement by the initial gauge length of the specimen (2.10 mm). These stress-strain curves are called the engineer's stress-strain curves. The differences between true stress-strain curves and the engineer's stress-strain curves are small when the strain is small and no necking has occurred in the tensile specimen.

The ultimate tensile strength of the specimen (determined from Fig. C3) is 1.16 GPa, which is the strength of wrought AISI 9310 [2]. The initial slope of the stress-strain curve is 107 GPa and should correspond to the Young's modulus of steel. However, the Young's modulus for steel is 197 GPa [2]; thus the present tensile fixture does not measure the elastic strain very accurately. The plastic strain at failure (elongation) is about 5 % in Fig. C3. In compacted AISI 9310 powder, the elongation was typically less than 2 %.

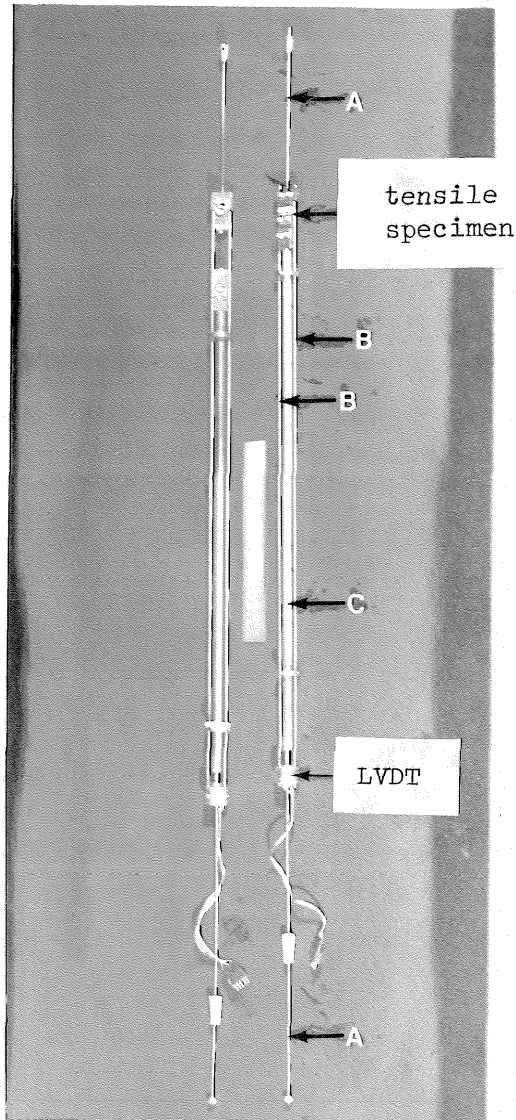


Fig. C1 The fixture on the right is used for measuring the tensile strength of dog-bone shaped tensile specimens. The fixture on the left is for ribbon shaped tensile specimens (not used in the present investigation). The letters "A" denote the Mo pull wires. The letters "B" denote the guide wires that are attached to the LVDT coil. The letter "C" denotes the central tube that is attached to the LVDT core.

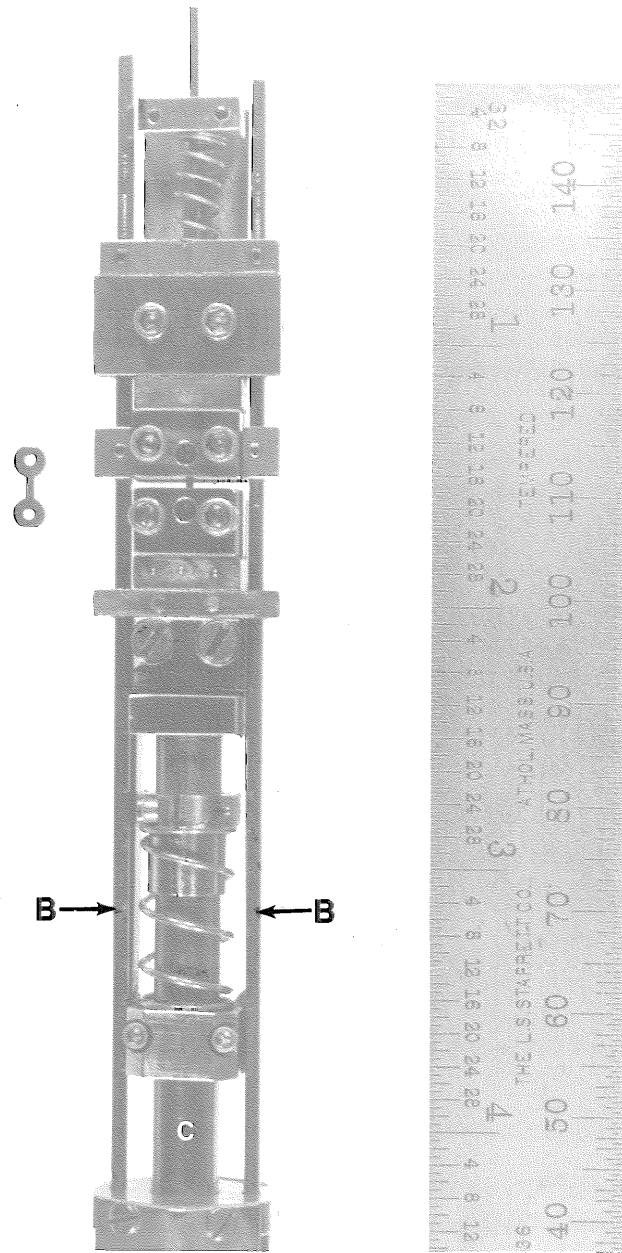


Fig. C2 The tensile test fixture with a sample tensile specimen is shown in the picture. The springs are used to hold the pins firmly to the holes in the tensile specimen. The upper pin is attached to the guide wires labeled "B". The lower pin is attached to the central tube labeled "C".

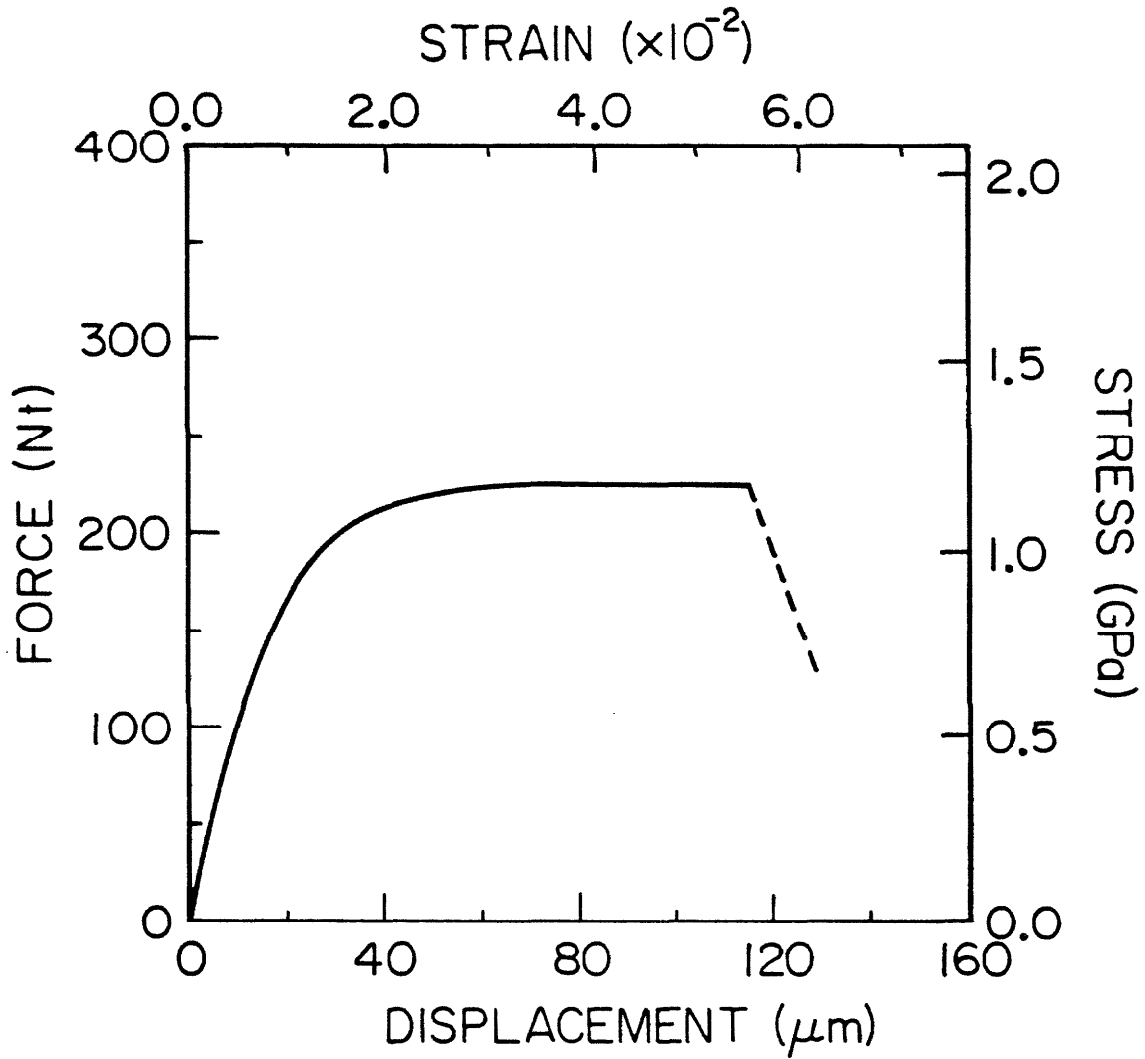


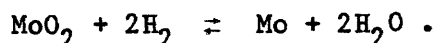
Fig. C3 The stress-strain curve of a tensile specimen pulled with the tensile fixture shown in Fig. C2.

APPENDIX D

SURFACE OXIDE REDUCTION

The molybdenum powders described in section 4.5 of Chapter 4 were treated by flowing one atmosphere pressure of H₂ gas for 2 hours at a temperature of 1000 K. The inflowing H₂ gas had a purity of 99.995 %, with O₂ impurity concentration of less than 20 ppm [4]. In addition, the H₂ gas was passed through a condensation coil submerged in a dry ice and alcohol bath (-57 C) to reduce the H₂O content in the inflowing gas to less than 14 ppm [5].

The surface oxides are reduced by the reaction



The reaction will proceed to the right when the free energy for the reaction, ΔG , is negative. This energy can be calculated from the relation [6]

$$\Delta G = \Delta G^0 + RT \ln \frac{[\text{Mo}] [\text{H}_2\text{O}]^2}{[\text{MoO}_2] [\text{H}_2]^2} ,$$

where

$$\Delta G^0 = \sum G^0(\text{products}) - \sum G^0(\text{reactants}).$$

R and T are the gas constant (8.314J/mole K) and the temperature, respectively. G^0 is the free energy of formation of the compound from the constituent elements of the compound. The value of G^0 for many compounds have been determined and can be found in the literature [7]. By definition, the value of G^0 for an element is zero. The quantities in brackets denote the activities of the various constituents in the

reaction. The activity of a substance may be thought of as the effective concentration of the substance. For an ideal gas, the activity is simply equal to the normalized density of the gas, i.e., the partial pressure divided by the total pressure. The activity of a solid with an invariant composition is equal to one, since the concentration of such a solid does not change during the chemical reaction [6].

At a temperature of 1000 K, the G^0 of MoO_2 and H_2O are -409 and -192 kJ/mole, respectively [7]. Since G^0 of H_2 and Mo are zero, the value of ΔG^0 is

$$\Delta G^0 = 25 \text{ kJ/mole}$$

at 1000 K. The pressure of H_2 gas is essentially equal to the total pressure; thus, $[\text{H}_2] = 1$ and $[\text{H}_2\text{O}] < 14 \times 10^{-6}$. Using the above mentioned values and with $[\text{Mo}] = [\text{MoO}_2] = 1$, the free energy for the reaction at 1000 K is

$$\Delta G = -186 \text{ kJ/mole.}$$

Thus, the reaction will proceed to the right until $\Delta G = 0$. However, since the H_2 gas is continually replaced; the concentrations of H_2 and H_2O are constant. Therefore, the reaction will proceed until most of the MoO_2 is depleted. The exact amount of remaining oxides depends on the reaction rate and details of the reaction mechanism. In the present investigation, quantitative measurements of the oxides before and after the treatment were not performed.

APPENDIX REFERENCES

1. Hawke, R. S., D. E. Duene, J. G. Huebal, R. N. Keeler, and W. C. Wallace, *J. Appl. Phys.*, 49, 3298 (1978).
2. Lyman, T., ed., Metals Handbook Eighth Edition, Vol. 7, American Society of Metals, Novelty, Ohio, 1972.
3. Lemkey, F. D., private communication.
4. Big 3 Industries, 2445 South St., Long Beach, California, 90805, private communication.
5. Weast, R. C., ed., Handbook of Chemical and Physics, 55th Ed., CRC Press, Cleveland, 1974.
6. Mahan, B. C., University Chemistry, 3rd Ed., Addison-Wesley Publishing Company, Menlo Park, California, 1975.
7. Robie, R. A., B. S. Hemingway, and J. R. Fisher, *U. S. Geological Survey Bulletin*, 1452, 1 (1978).